Politecnico di Torino

POLITECNICO DI TORINO

Department of Electronics and Telecommunications

Master's Degree Course in Mechatronic Engineering

Master Thesis

Analysis of Mechanical Metamaterial Structures for 3D printed wearable strain sensors

Supervisor:

Prof. Stefano Stassi

Candidate:

Kyriaki Karageorgopoulou

July 2024

Table of Contents

Introduction

Mechanical metamaterials are engineered materials with properties that are not ordinarily found in nature. They derive their characteristics from the geometric arrangements of their microstructure rather than their actual composition. These materials often present unusual mechanical properties, such as: negative Poisson's ratio, high stiffness-to-weight ratio, tunable mechanical response.

They can find their application in various fields such as aerospace, automotive, and biomedical engineering due to their unique potential customization.

Given their unique properties, their study and better understanding can lead to the production and improvement of already existing sensors. An application of that in the future could be the development of an electronic skin for prosthetics and robotic applications.

Due to the vast family of mechanical metamaterials, the structures that have been considered for this research were just two: Honeycomb Re-Entrant structure & 4-Star Re-Entrant structure.

The selected models were firstly built and tested digitally with the use of COMSOL Multiphysics and then, they were later physically printed with the aid of a 3D FDM printer and a UV DPL.

The tests done on said models were both mechanical and electrical ones in order to determine their mechanical and piezoresistive response. Lastly, it was decided to also compare these experimental data with the simulations made in advance.

It has been observed, through the results of this study, that there is a high potential for the geometries tested and this suggests that in the future it will be possible to build sensors without worrying anymore about the properties of the materials used to build them. Hence, it will be possible to focus mainly on their geometry at a microscopic level.

1. Fundamentals of Mechanical Metamaterials

1.1. Definition and characteristics of metamaterials

Mechanical Metamaterials are materials that exhibit properties and functionalities that cannot be realized with conventional materials. In fact, in order to understand better their unique properties, we need to focus on the study of mechanical characteristics such as: Density, Poisson's ratio, and compressibility.

Before analyzing further their behavior, it is important to consider metamaterials can be found in literature under different names based on the different circumstances and fields they are studied in. Some relevant examples of synonyms are stated above:

- Advanced Materials
- Architectured Materials
- Optimized Materials
- Multi-Scale Materials
- Smart Materials
- Multi-Physics Materials
- Materials with negative mechanical constitutive coefficients
- Composite Materials
- Complex Materials

Those materials offer a paradigm shift in material design and engineering. In order to understand them better, it is necessary to analyze the different properties that make them so special:

Geometric Design: Metamaterials derive their properties from their intricate geometric design rather than the materials they are made from. They combine the concept of hierarchical architecture with material size effects at micro/nanoscale. In other words, those kinds of materials are able to obtain unique properties in their macrostructure by only arranging geometrically its own micro/nanostructure.

Unusual Mechanical Properties: Unlike conventional materials, some mechanical metamaterials can expand in multiple directions simultaneously when compressed (Negative Poisson's Ratio).

Their mechanical properties can also be tailored by adjusting their geometric design, enabling control over stiffness, damping, and energy absorption (Tunable Mechanical Response).

On the other hand, they can exhibit exceptional stiffness relative to their weight, making them desirable for lightweight structural applications (High Stiffness-to-Weight Ratio).

Finally, metamaterials can exhibit nonlinear mechanical behavior, such as bistability or auxetic behavior (Nonlinearity).

Customizability: Mechanical metamaterials offer a high degree of customization. They can be customized accordingly in order to meet the requirements of diverse applications, including aerospace, automotive, robotics, and biomedical engineering.

Multiscale Structure: As stated above, metamaterials often feature hierarchical structures with repeating patterns at multiple length scales. This design allows for precise control over performance characteristics.

Applications: Mechanical metamaterials have resulted essential in multiple fields such as Aerospace, Acoustics, Seismic Protection, Biomechanics.

Mechanical metamaterials [20] encompass a wide range of structures and designs, each with its own unique properties and characteristics. A possible classification of said materials is listed below (Fig. 1.1) :

- Lattice Materials
- Origami-inspired Materials
- Topologically interlocked materials
- Architectured materials
- Morphing materials
- Granular materials
- Hierarchical composites

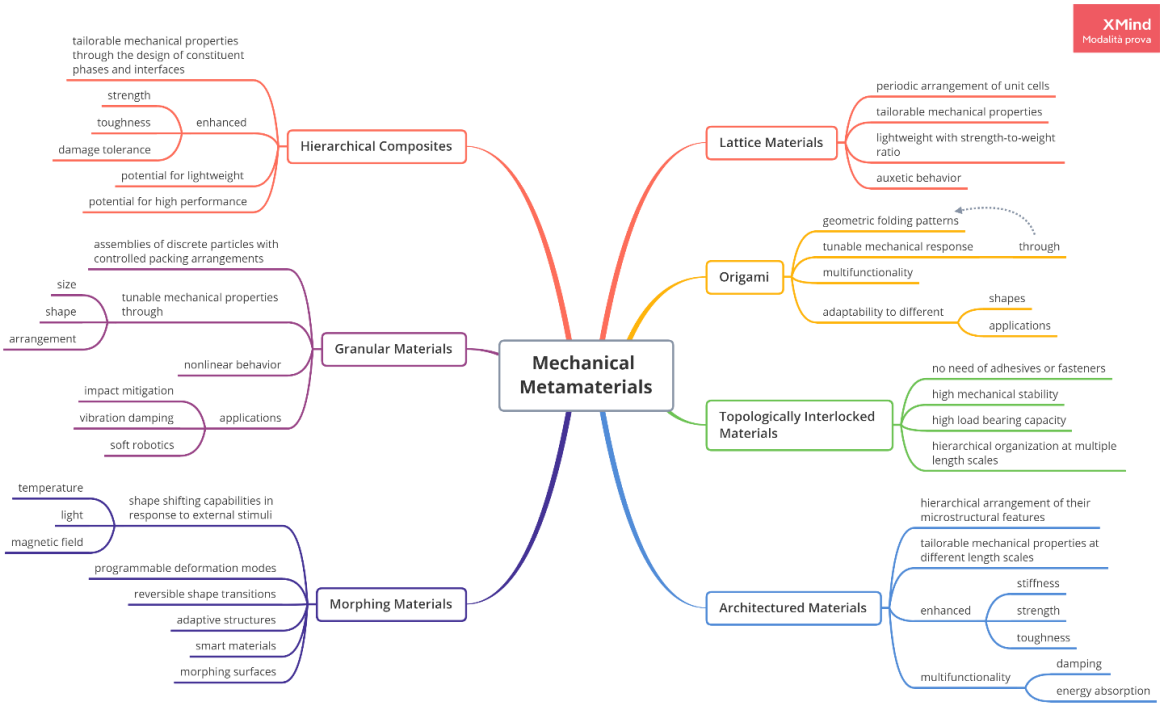

Figure 1.1 Classification of Mechanical Metamaterials (map created with XMind)

1.2. Classical continuum mechanics and higher gradient theories

Studying normal structures typically involves analyzing materials with properties determined primarily by their chemical composition and microstructure. This analysis often relies on the classical 3D Cauchy's continuum mechanics (Fig. 1.2). According to those principles, examining the behavior of materials under various loading conditions and understanding their mechanical properties through empirical testing and theoretical models is the key. On the other hand, mechanical metamaterials require a shift in perspective from traditional material science to the inclusion of principles from fields such as mechanical engineering, solid mechanics, and topology optimization.

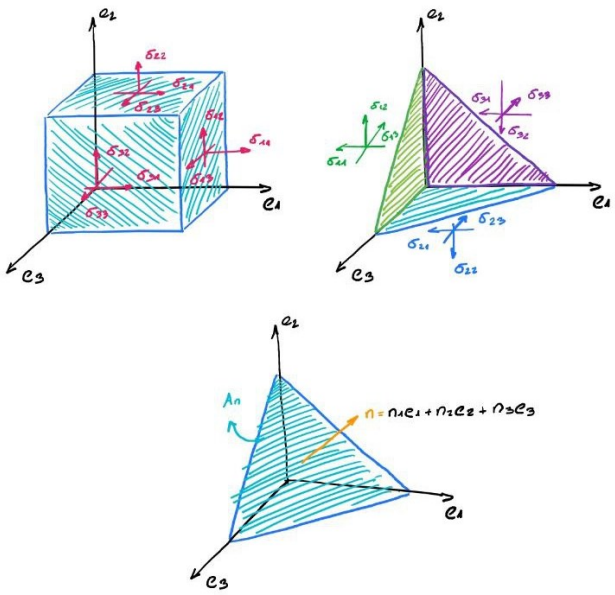

Figure 1.2 Cauchy's Tetrahedron (Classical Continuum Mechanics)

The difference between the two theories can also be observed through their predictability and understanding. Normal structures are often well understood based on established material properties and empirical data, while mechanical metamaterials require advanced mathematical modeling, computational simulations, and experimental validation in order to be predicted. As a result, classical continuum mechanics is not enough, and Higher Gradient Theory is considered (Fig. 1.3).

Both techniques are used to describe the mechanical behavior of materials, but they differ in their assumptions, scope, and ability to capture microstructural effects. Classical continuum mechanics assumes that materials behave as continuous media, where stress, strain, and deformation vary smoothly throughout the material without considering microstructural effects. On the other hand, higher gradient theories relax the assumption of continuity by considering materials with microstructural effects such as defects, interfaces, or fine-scale features. These theories include higher order derivatives of displacement or strain in the constitutive equations to capture nonlocal effects.

Another difference between the two can be observed in the scope of the study. Classical continuum mechanics is suitable for analyzing materials with homogeneous and isotropic properties at length scales larger than the characteristic microstructural length. On the contrary, higher gradient theories are applicable to materials with length scales comparable to or smaller than the characteristic microstructural length.

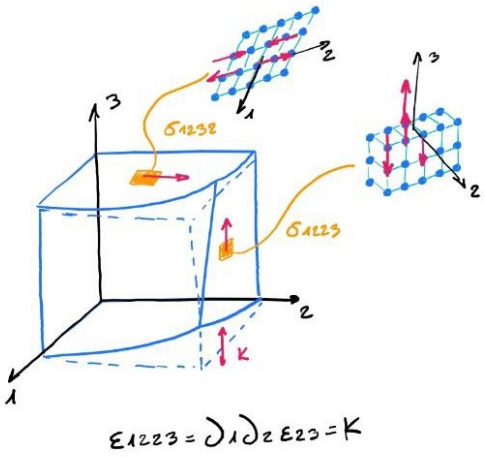

Figure 1.3 Unit cube element subjected to a constant second strain gradient k. Schematics of the deformation pattern and the work-conjugate triple stresses (Example of Higher Gradient Theory).

Higher gradient theories are also known as higher-order continuum theories or gradient elasticity theories. In the context of mechanical metamaterials, those theories are particularly relevant due to the intricate geometric arrangements and multiscale structures characteristic of said materials. Mechanical metamaterials in fact require the study of two different scales:

- Macroscopic scale: referred to the length scale where the phenomena are observed and need to be controlled.
- Microscopic scale: referred to one or more length scales used to build the architecture itself.

In mechanical metamaterials, where the structural arrangement often occurs at multiple length scales, the microstructural effects play a crucial role in determining material properties.

Another thing that need to be considered at this point is that higher gradient theories inherently capture nonlocal effects, where the response of a material at a particular point depends on the deformation history of the neighboring points. This is especially important in mechanical metamaterials with complex architectures, where localized deformations can propagate over larger distances due to the material's multiscale structure.

Finally, mechanical metamaterials can exhibit instabilities and localized deformation modes that are not adequately captured by classical continuum mechanics. Higher gradient theories provide a framework for modeling and predicting these instabilities, allowing for a more accurate representation of the material's mechanical behavior.

Compared to ordinary materials, when studying mechanical metamaterials a reverse approach is requested. In fact, the first step is to define the desired behavior of the material and then subsequently the actual model of the microstructure.

1.3. Auxetic Metamaterial Structures

Mechanical metamaterials and auxetics are closely linked through their shared property of negative Poisson's ratio (Fig. 1.4), also known as auxetic behavior. In other words, by having a negative Poisson's ratio, auxetic materials expand laterally when stretched longitudinally, in contrast to conventional materials that contract laterally under tension.

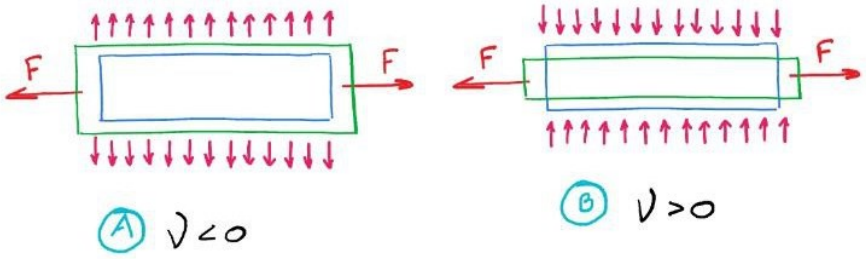

Figure 1.4 Auxetic Behavior (A) vs non-Auxetic Behavior (B)

Mechanical metamaterials can be designed to exhibit auxetic behavior through specific geometric arrangements of their microstructure or unit cells. The negative Poisson's ratio is often achieved by introducing structures that allow for lateral expansion or reorientation of structural elements under loading, leading to unique mechanical properties not found in traditional materials.

There are different complex geometric arrangements to utilize such as:

- Lattice structures
- Origami-inspired patterns
- Topologically interlocked configurations

Auxetic materials can be fabricated using various techniques, including re-entrant structures, re-entrant foams, and hierarchical architectures.

The advantages obtained by those structures are unique. These materials are often utilized in impact protection systems, cushioning materials, smart textiles, biomedical implants, and structural components where enhanced energy absorption, improved conformability, and increased toughness are desired.

By combining the principles of mechanical metamaterial design and auxetic behavior, engineers can create innovative materials with tailored mechanical properties for specific applications, further expanding the potential of both fields.

At this point, based on the definition of auxetic material, a further classification can be made. In fact, metamaterial structures can be divided into different categories based on their auxetic behavior (Fig. 1.5).

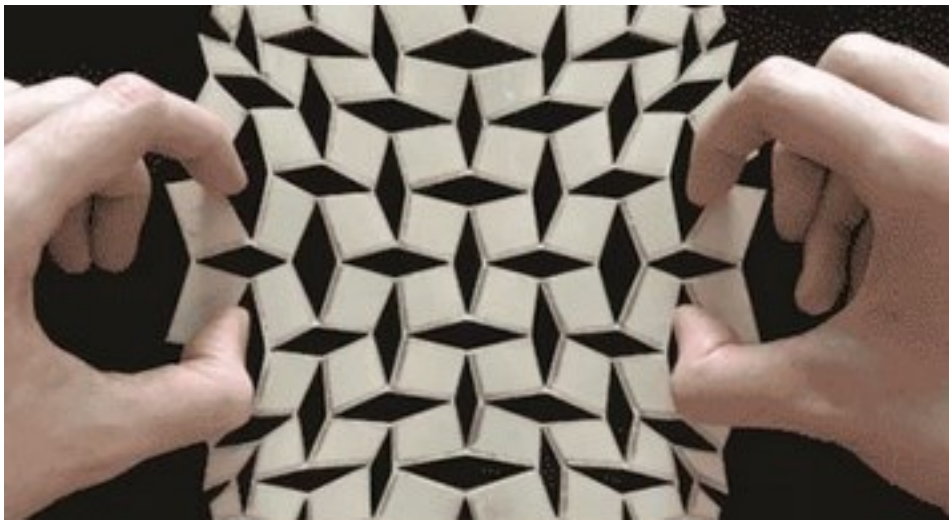

Figure 1.5 Auxetic Structure (Image taken from Focus.it)

- Re Entrant Structures
  The term ''Re-Entrant'' refers to something directed inwards or having a negative angle. Those structures, in fact, have the ability to deform mainly through the hinging of their cell ribs (Fig. 1.6). As a result, the Young's modulus of re-entrant structures is found to decrease during deformation while the non-linear Shear modulus increases. The anisotropic nature of those structures allows the Poisson's ratio to have an arbitrarily large negative value.

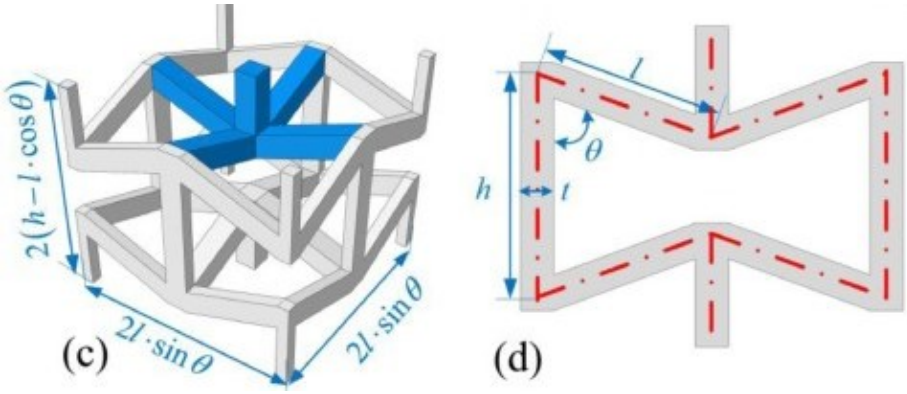

Figure 1.6 Re Entrant Structures [24]

The variety of structures that go under the name ''Re-Entrant'' is very vast. For this reason, it is useful to take a look at the different micro categories and their relative properties:

- Foams

  Foams (Fig. 1.7) present an auxetic effect through the behavior of their rigid joints which preserve their geometry and topology under stress. There are mainly two types of foams found so far: Polymeric Foams (ν=-0.7) and Metallic Foams (ν=-0.8).

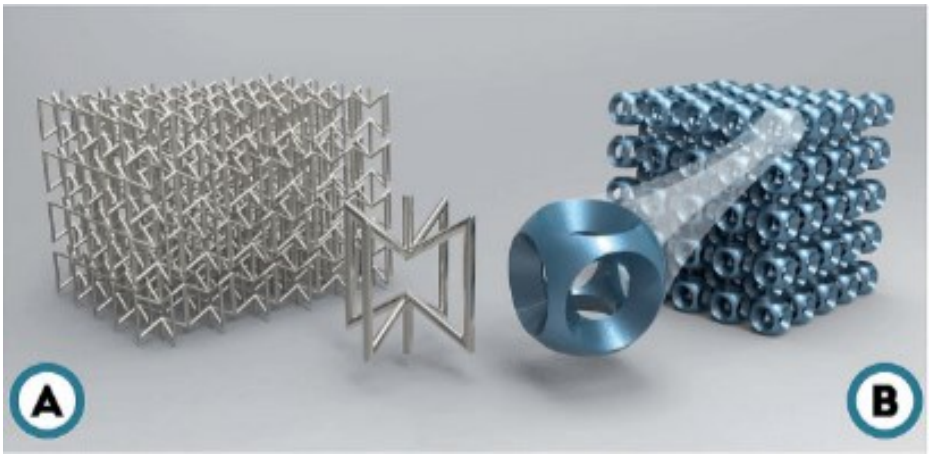

Figure 1.7 Re Entrant Structures – Foams [12]

- Honeycombs

  Honeycomb structures are defined as any array of identical re-entrant cells which nest together to fill a plane or 3D space, and their main property is that they exhibit a negative Poisson's ratio (Fig. 1.8). They are also known for their high anisotropy.

  As the re-entrant angle increases, the stiffness decreases. In other words, the auxenticity of the structure is increased. On the other hand, by increasing the length of the base wall flexibility is obtained while the Poisson's ratio stays virtually unmodified.

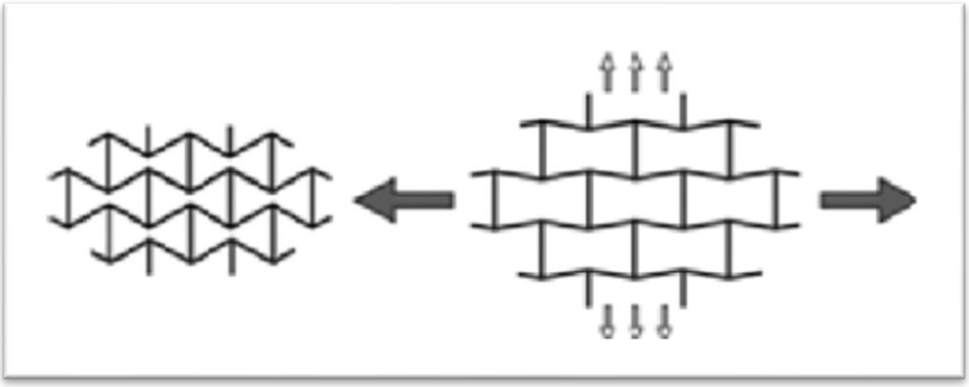

Figure 1.8 Re Entrant Structures – Honeycombs [25]

Aside from the traditional re-entrant honeycombs, recently new types of honeycombs have been discovered.
In the case of Auxetic Arrowhead structures (Figure 1.9a), depending on the configuration of the arrowhead, compression will initiate the collapse of the triangles (Transverse Contraction ν=-0.8).
Furthermore, arrows can be interconnected in such a way that their arms form stars (Fig. 1.9b).

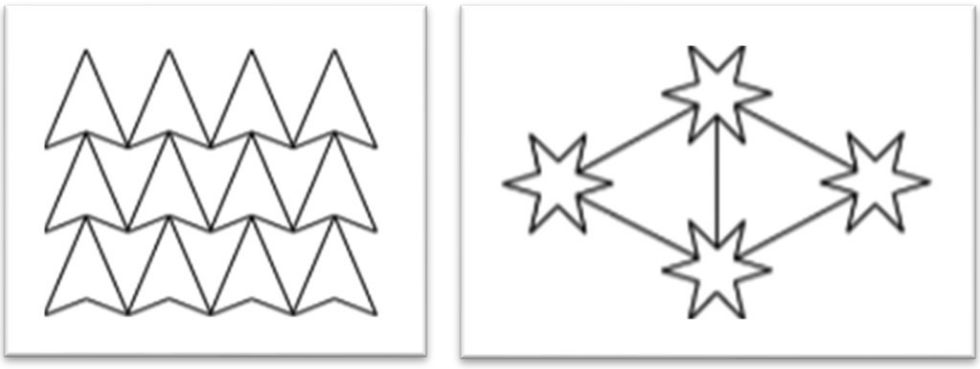

Figure 1.9 Re Entrant Structures - special type of Honeycombs: (a) arrows [26], (b) stars [3]

- Pore shapes

  Results suggest that for this architecture maximum auxenticity can be reached for samples with the highest possible void fraction. By changing the porosity of the structure, alterations can be observed in the stiffness, critical buckling strain, Poisson's ratio, and compaction properties.
  Based on the shape of the void, pore shape structures are further divided into three different types, each with its own properties (Fig. 1.10). In particular, Type A and Type B are known for their microscopic instabilities and as a consequence, a significant increase in compaction, opposed to Type C which presents macroscopic ones that induce a positive Poisson's ratio. The best among the three for its auxetic response is by far Type B.

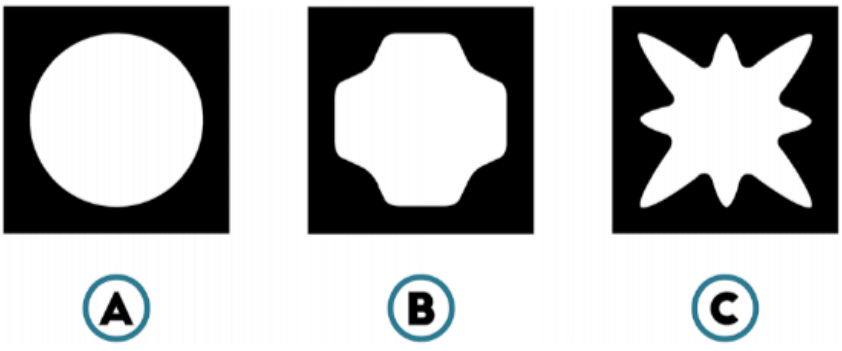

Figure 1.10 Re Entrant Structures - Pore Shapes [20]

- Microporous polymer

  A special case of re-entrant structure is the microporous polymer (Polytetrafluoroethylene).

  The structure is obtained through the interconnected network of disc-shaped particles and fibrils which leads to a very high anisotropic behavior (ν=-12). The fully expanded form of the structure can be observed with the rotation of the disc-shaped particles (Fig. 1.11).

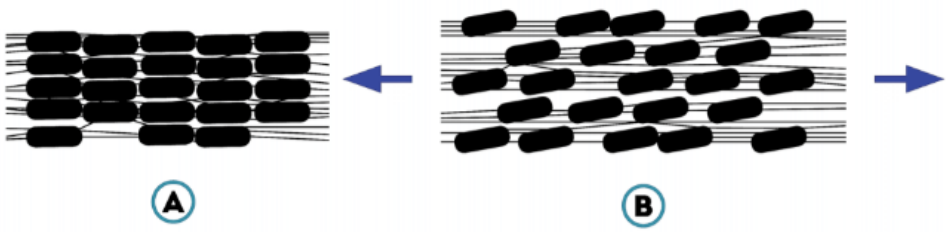

Figure 1.11 Re Entrant Structures - Microporous Polymer [20]

- Rotating (Semi)Rigid Structures

  The second type of auxetic structures is called Rotating Rigid and Semirigid Architectures. The structure itself is obtained by the rotation of 2D and 3D geometrical shapes, and based on that, they are divided into different families of their own.

  When loaded, those architectures deform through the rotation of their rigid units and thereby changing the angles between them (Fig. 1.12). The rigid structure of the joints has a negative influence on the auxetic effect. Lastly, all the anisotropic rotating systems can be reduced to one of the isotropic ones by carefully changing the aspect ratio, or the angles of rotation ϕ and Θ.

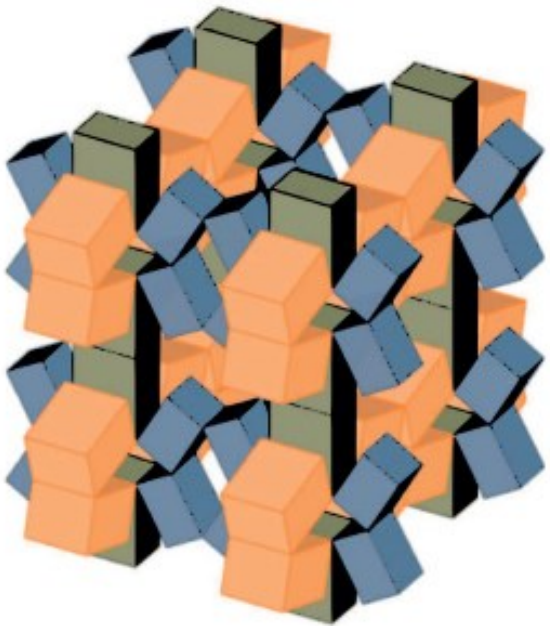

Figure 1.12 Rotating (Semi)Rigid Structures [16]

- Squares
  Systems composed by squares exhibit a constant Poisson's ratio of -1. If their rotating units were assumed semi-rigid, their Poisson's ratio would become dependent on the relative rigidity and the direction of the loading.
- Rectangles
  By replacing the squares with rectangles, the architecture exhibits both positive and negative Poisson's ratios depending on the above-mentioned angles of rotation. The voids that those structures form during their rotation divide the latter into two types (Fig. 1.13).
  Type I is characterized by rhombi-shaped voids (Anisotropic behavior) while Type II by parallelogram-shaped voids (Isotropic behavior).

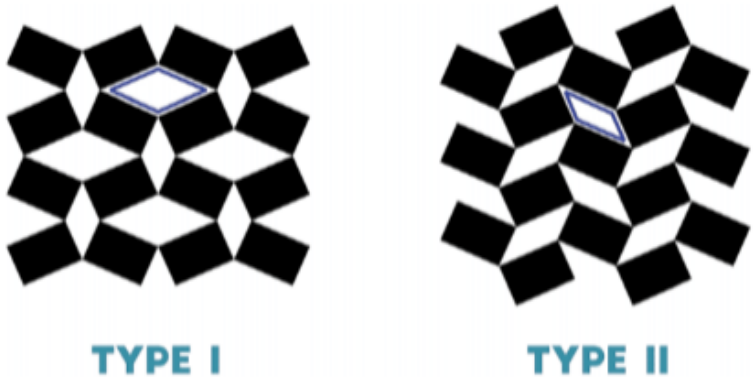

Figure 1.13 Rotating (Semi)Rigid Structures – Rectangles [20]

- Triangles
  This kind of architecture exhibits different behaviors based on the type of triangles it is composed by (Fig. 1.14).
  The triangles in question can either be hinged equilateral rigid ones or isosceles ones.

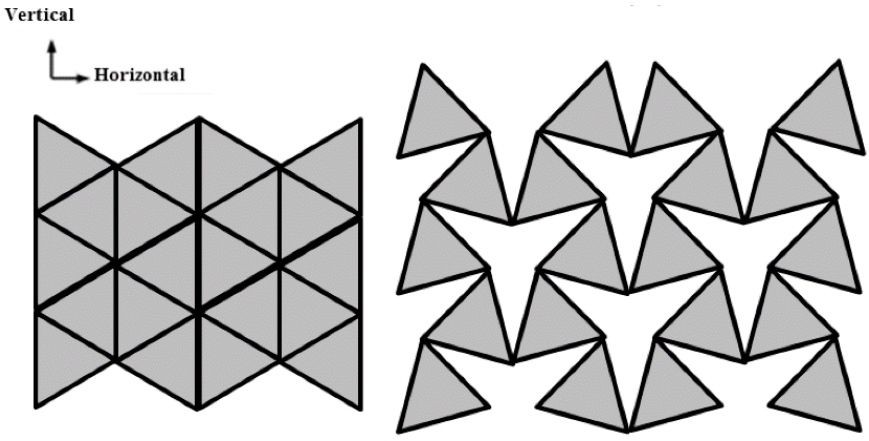

Figure 1.14 Rotating (Semi)Rigid Structures – Triangles [2]

- Rhombi

  Rotating rhombi can exhibit an auxetic behavior and their Poisson's ratio depends on the rotating angles ϕ and Θ but also on the direction of the load (Fig. 1.15).

  They can be found in two different arrangements: Type α and Type β (Fig. 1.16).

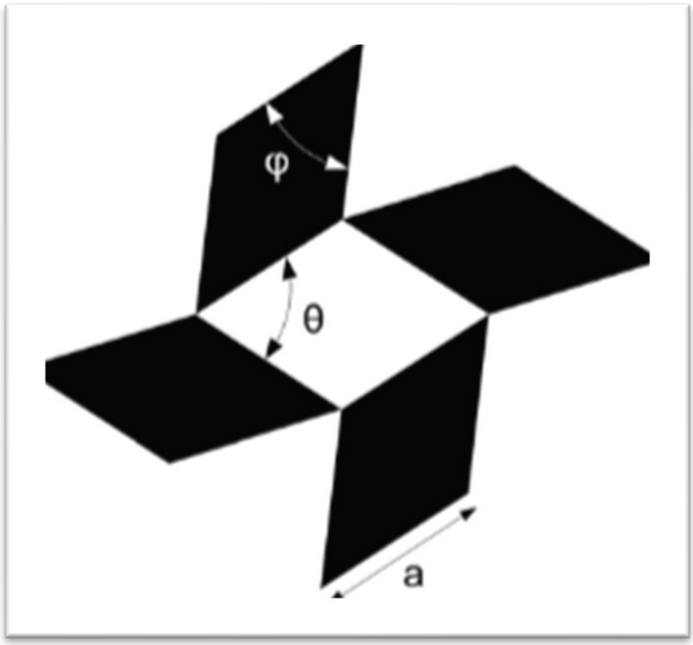

Figure 1.15 Angles of rotation ϕ & Θ [20]

Type α is highly anisotropic and the connection between adjacent angles is of the opposite type (acute-obtuse, obtuse-acute).

On the other hand, Type β presents a Poisson's ratio equal to -1 as the adjacent angles are of the same type (acute-acute, obtuse-obtuse).

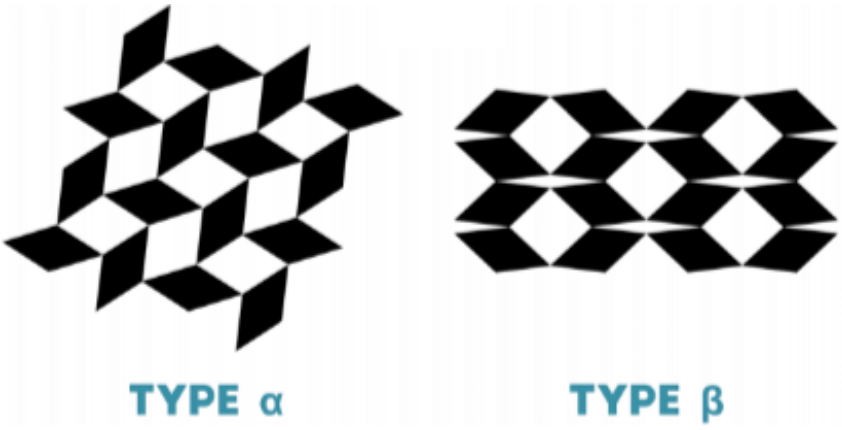

Figure 1.16 Rotating (Semi)Rigid Structures – Rhombi [20]

- Parallelograms

  Lastly, rotating structures can be also obtained by the rotation of parallelogram shapes. This architecture combines the connectivity schemes of the rhombi and the rectangle structures. This results in a subdivision of the following types (Fig. 1.17): Type Iα, Type Iβ, Type IIα, Type IIβ.

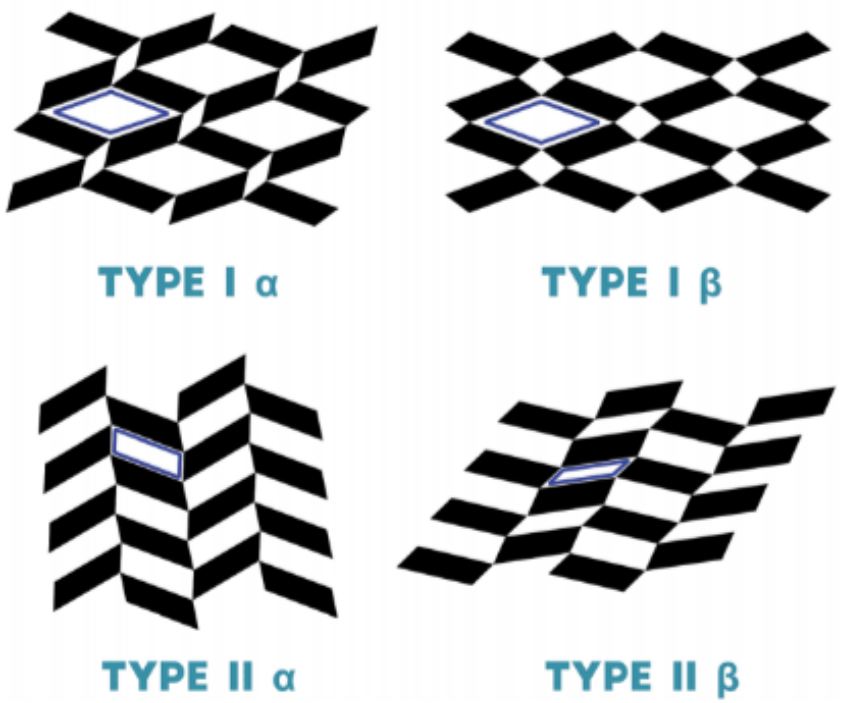

Figure 1.17 Rotating (Semi)Rigid Structures – Parallelograms [20]

- Chiral Structures

  Finally, auxetic chiral structures represent a unique class of materials with unconventional mechanical properties.

  The main feature of the structure is ''chirality'', meaning they are non-superimposable mirror images of each other (Fig. 1.18). This property arises from their asymmetric arrangement of the structural elements.

  Like every other category, chiral structures can be divided in smaller groups based on their characteristics:

  - Twisted Structures

    These structures are formed by twisting or helically arranging the struts or beams, resulting in chirality and auxetic behavior. As the beams rotate under mechanical loading they cause the ligaments to flex. A tensile loading would lead to the folding of the ligaments, while a compressive one would lead at their unfolding.

- Honeycomb Structures
  Chiral honeycombs have been designed with asymmetric unit cells, leading also to auxetic behavior. They can be easily fabricated using additive manufacturing techniques.

- Origami-inspired Structures
  Those designs can be used to achieve intricate chiral patterns by folding and manipulating flat sheets.

- Lattice Structures
  Composed of interconnected struts or beams arranged in a repeating pattern, they too can exhibit an auxetic behavior. By carefully designing the lattice geometry, chirality and negative Poisson's ratio can be achieved.

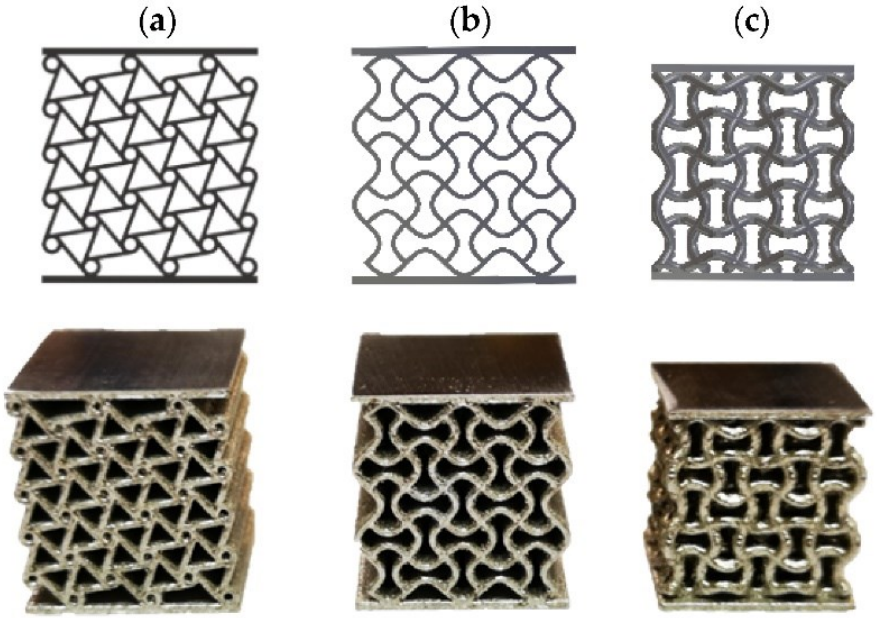

Figure 1.18 Chiral Structures [1]

1.4. Sensor Applications

Mechanical metamaterials have various sensor applications due to their unique mechanical properties and ability to respond to external stimuli. The sensors in question can be divided in the following main categories:

- Strain Sensors
- Pressure Sensors
- Acoustic Sensors
- Temperature Sensors
- Chemical Sensors
- Biomechanical Sensors

The latter in particular can be designed to mimic the mechanical properties of biological tissues or structures, making them suitable for biomechanical sensing applications. These sensors can be used to detect and measure forces, strains, or deformations in biological systems, enabling applications such as wearable health monitors, prosthetics, and medical implants.

It is important to specify at this point that all the types of sensors mentioned above can be considered as part of a bigger macro-category of sensors called Auxetic sensors. The main feature of auxetic sensors is that the variation of their electrical signal depends on the geometry of the sensor itself. For this reason, auxetic sensors utilize the unique mechanical properties of auxetic metamaterials to detect and measure changes in their structure properties. According to Jiang's article ''Auxetic Mechanical Metamaterials to Enhance Sensitivity of Stretchable Strain Sensors'' the auxetic structures tested on that occasion, had the following characteristics:

- Compared to normal sensors, the sensitivity in this case was improved by 24-fold.
- As the structure is under stress, the microcracks elongate generating a variation in resistance (Fig. 1.19).

The main applications of auxetic sensors can be found in: wearable devices, healthcare monitoring, soft robotics, and electronic skins.

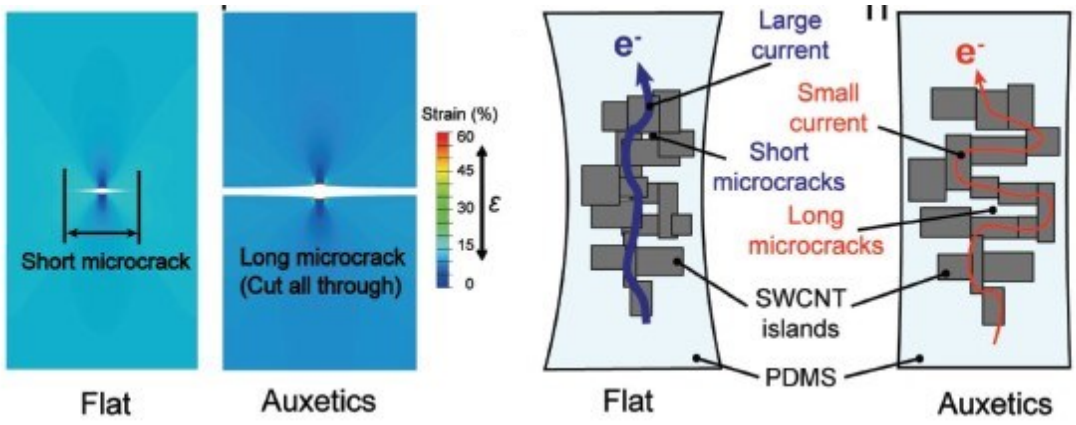

Figure 1.19 Auxetic sensors, elongation of microcracks [18]

In regard of this topic, auxetic sensors can be classified based on their sensing mechanism, structure, and application. A very common type of auxetic sensor is the capacitive type (Fig. 1.21). Its working principle consists in the change of capacitance between electrodes or between an electrode and a surrounding conductive surface after a mechanical strain. The main advantages of this sensor are: high linearity, repeatability and a Gauge factor close to 1 (sensitivity). Capacitive sensors are often used in soft robotic applications and examples of that can be:

- Human elbow (Fig. 1.20)
- Jamming gripper

The key to the utility of capacitive sensors is their potentially personalized applications due to compliance and conformability.

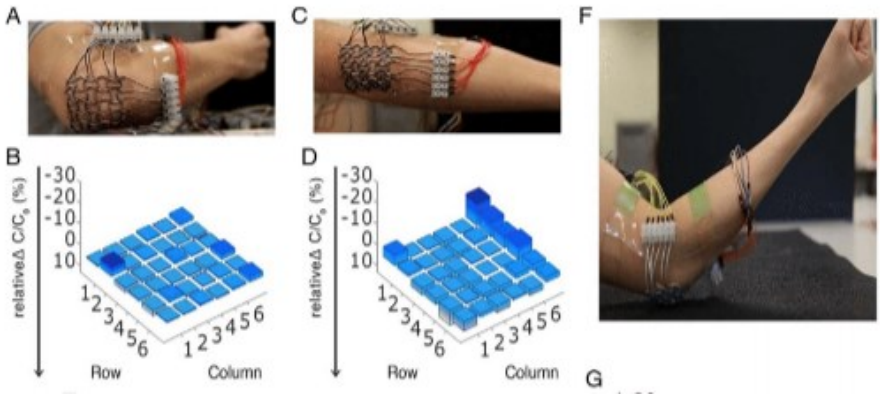

Figure 1.20 Wearable capacitive elbow sensor [19]

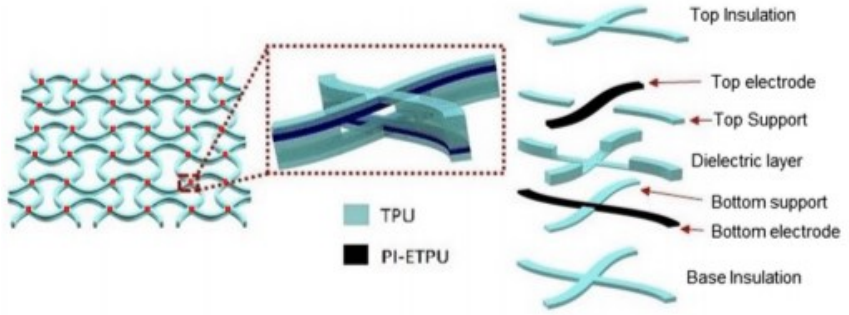

Figure 1.21 Capacitive sensor structure. [19]

Capacitive sensors can be improved in sensitivity with the use of Ionic Hydrogels (Fig. 1.22). Ionic hydrogels are composed by: liquid metal (EGaln), elastomers, negligible water content. Because of the latter, the only issue found with this type of sensors is the evaporation of the aquatic contents. The characteristics that make hydrogels original and unique are: high linearity, repeatability, and low hysteresis.

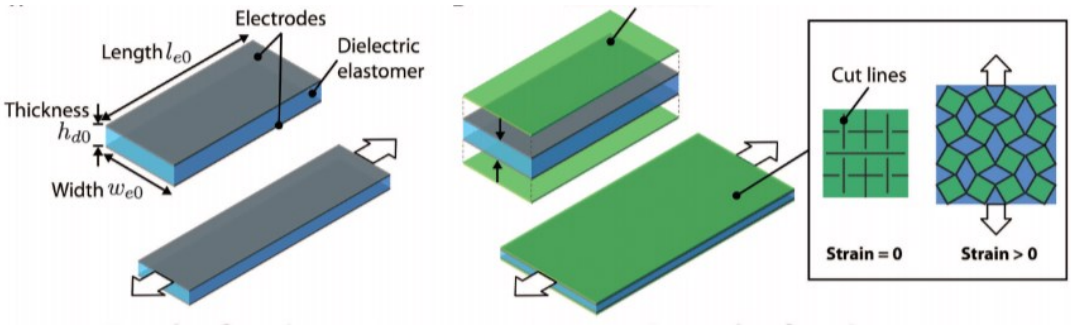

Figure 1.22 Ionic hydrogels [8]

Auxetic sensors can be utilized for biomechanical sensing and applications, such as monitoring joint movements, muscle contractions, or body posture. These sensors are valuable for healthcare, sports performance monitoring, and rehabilitation.

- Healthcare

  When dealing with wounds, auxetic sensors can be a valuable asset to consider. In order to better understand this field of application, it is important to remember that the human skin has certain important characteristics: it is composed by two main layers (epidermis and dermis), and each has a specific purpose and structure (Fig. 1.23).

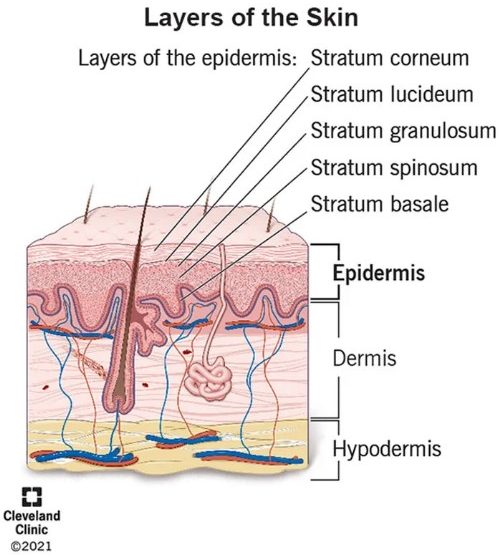

Figure 1.23 layers of the human skin (Clevelandclinic.org)

Based on the entity of the wound, a certain amount of additional skin is usually required. If the entity of the wound to be treated is small, it is often a custom to borrow additional skin either from the patient or from a donor. On the other hand, whenever this is not possible, in case of bigger wounds, the solution can be found in auxetics. Due to their mechanical strength, stability, and porous structure, auxetics can be a great solution to nowadays issues related to cost, integration, and esthetics (Fig. 1.24).

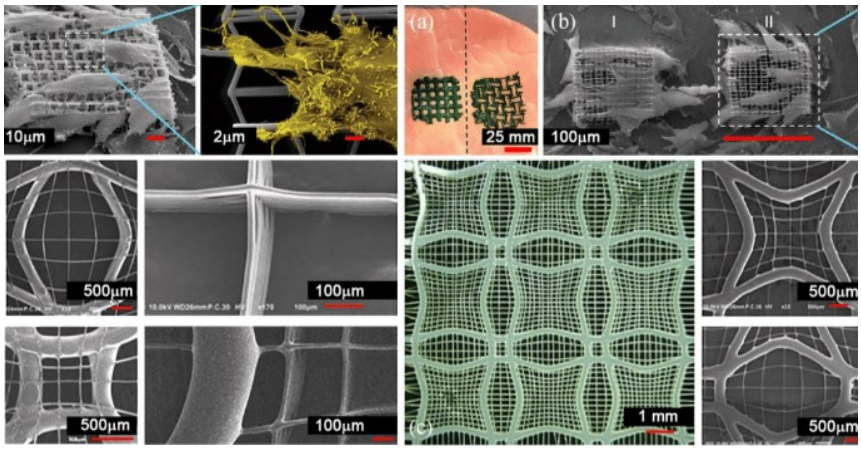

Figure 1.24 auxetics used as additional skin in wound treatment [6]

According to [18], by dealing with auxetic structures applied to wound treatment, in order to verify the performance of the auxetic sensors, three things had to be checked:

- Sensitivity: 24 higher
- Stretchability: it reaches 98% while the human skin requires only 30%
- Cyclic durability

An additional tool used for healthcare applications are Auxetic Hydrogel patches. They are composed by two layers: PEGMA and GelMA.

Due to their desirable characteristics (negative Poisson's ratio, isotropic behavior, biocompatible, biodegradable, support cell attachment, proliferation, differentiation) those patches can be suitable for different complex applications such as:

- Heart
- Skin
- Lungs
- Bladder

- Healthcare monitoring

Due to their high sensitivity, auxetic sensors are also used for health monitoring applications. In the picture above for example, an auxetic sensor is used for the monitoring of the beating of a human heart and it can be clearly observed how much the sensitivity is improved compared to the sensitivity of a traditional sensor (Fig. 1.25).

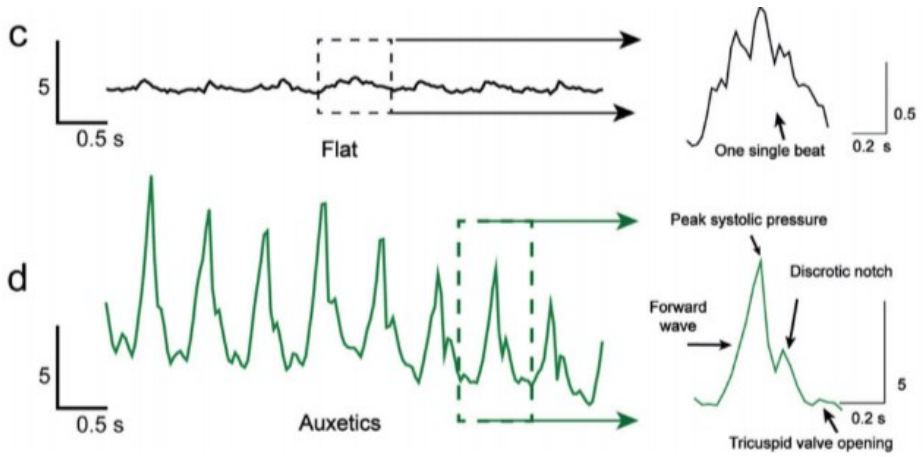

Figure 1.25 heart rate monitoring using auxetic sensors [18]

- Rehabilitation

Additive manufacturing and auxetic structures are often combined to achieve certain goals and efficiency, especially in research and development. This combination can be observed in the study [5]. In general, it is a human goal to create complex structures by using synthetic forms inspired by natural organisms. The challenge is to combine

the elastic properties, the resolution, and the integrated actuation of the structure. The complex structures built in this case are:

- Tendon driven hands (Fig. 1.26).
- Pneumatically actuated walking manipulators
- Pumps that mimic the heart (Fig. 1.27)

The process required an additive manufacturing technique that involved 4 different printing nozzles. That way it was possible to print using multiple materials simultaneously. This process not only made the structure closer in composition to the real one, but it also generated structures that had an auxetic behavior like real human organs have in nature. In fact, human tissues are extremely elastic and difficult to reproduce with the materials we have at our disposal. Additive manufacturing and auxetics are the key to this problem. The only limitations observed were related to speed and the printing dimensions.

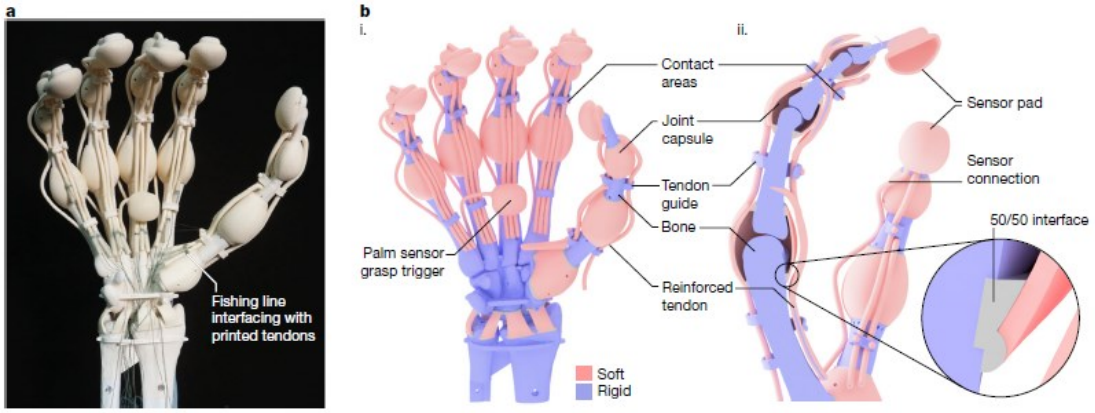

Figure 1.26 tendon driven hand [5]

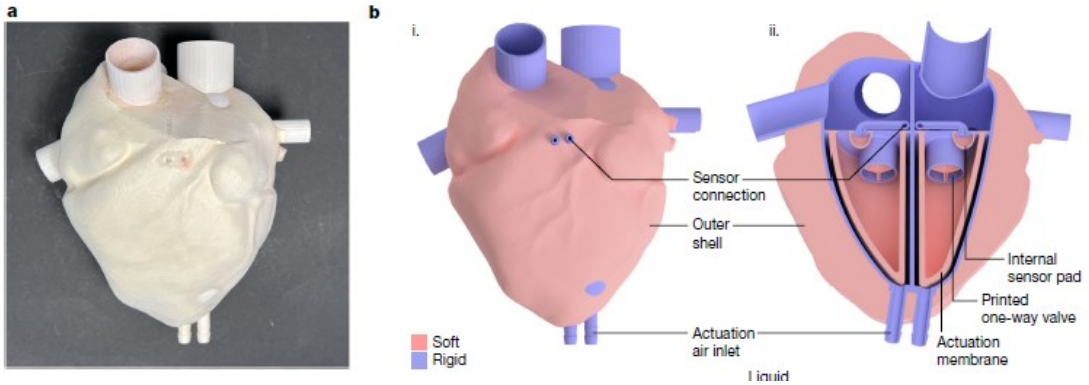

Figure 1.27 artificial pumps that simulate the human heart [5]

- Sports Healthcare

  Last but not least, auxetic structures can be also found in sports applications like athletic shoes, mainly used for energy absorption. The unit cell used in this case that

guarantees an auxetic behavior is a cell that has the same shape as the sea urchin. For this application additive manufactured lattice has been used and three types of tessellations, using the urchin-shaped unit cells, have been observed. Each tessellation has a different distribution of the load:

- Body Centered Cubic (BCC), load distributed radially (Fig. 1.28).
- Face Centered Cubic (FCC), load distributed in a zig zag pattern (Fig. 1.29).
- Hexagonal Closely Packed (HCP), s-shaped load (Fig 1.30).

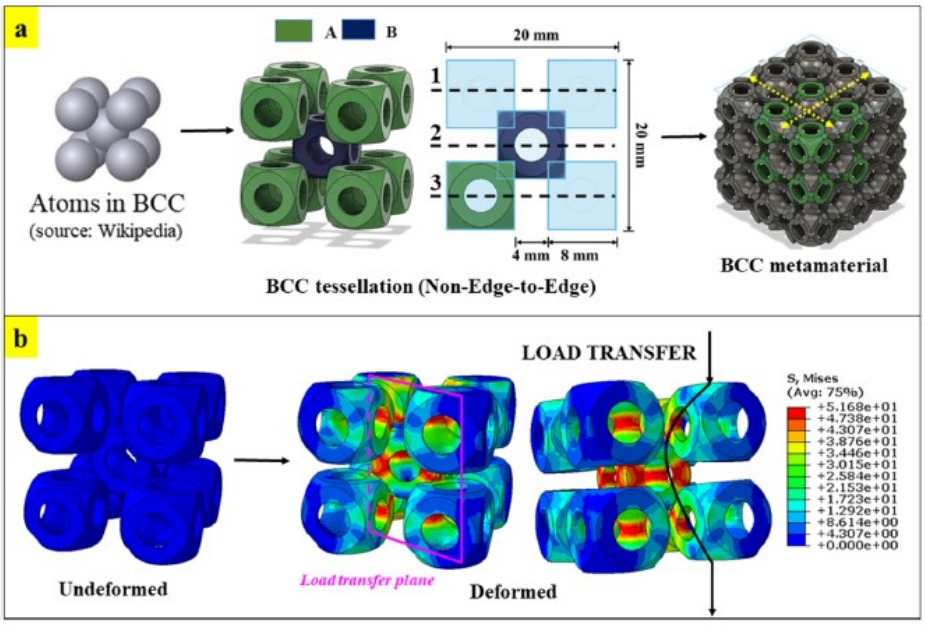

Figure 1.28 BCC tessellation [4]

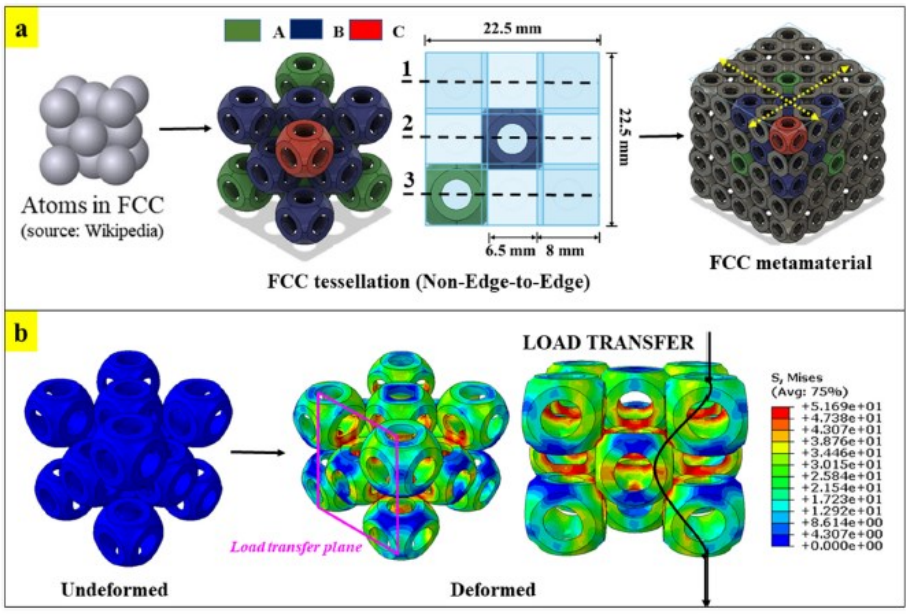

Figure 1.29 FCC tessellation [4]

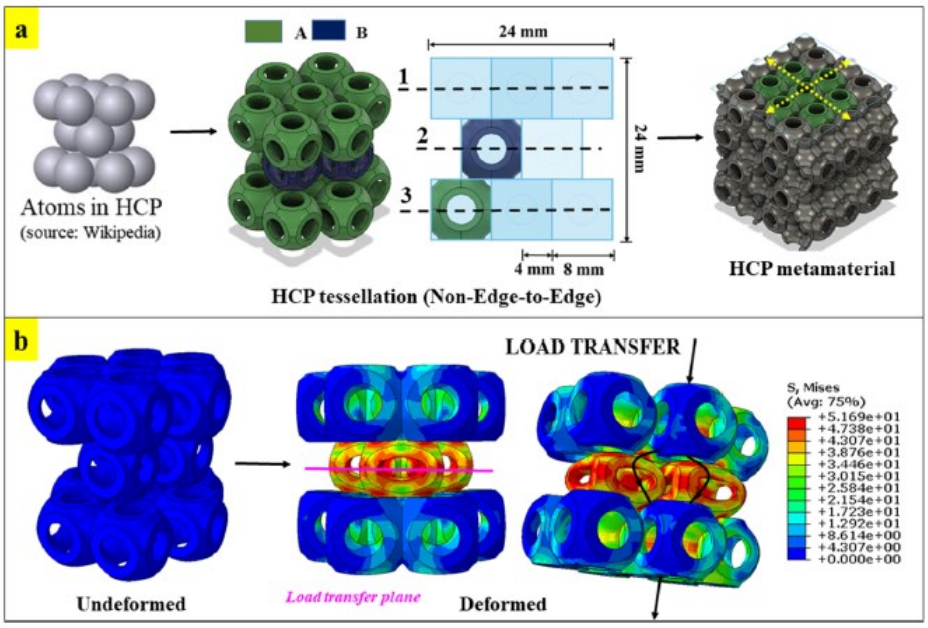

Figure 1.30 HCP tessellation [4]

2. Design and Modeling of Mechanical Metamaterials

2.1. Selection of suitable metamaterial structures

For the purpose of this study a series of geometries have been selected to be designed and tested in order to determine if the observed behavior was suitable for future sensor applications. As mentioned in the previous chapter, our interest was focused entirely on Auxetics and in particular, on structures with a negative Poisson's ratio.

The main type of auxetic structure to be considered was the Re-Entrant structure. The focus was mainly directed towards the honeycomb re-entrant structure due to its interesting properties under tensile stress (Fig. 2.1). Later on, the 4-pointed star re-entrant structure was also taken into consideration for its interesting behavior under compression.

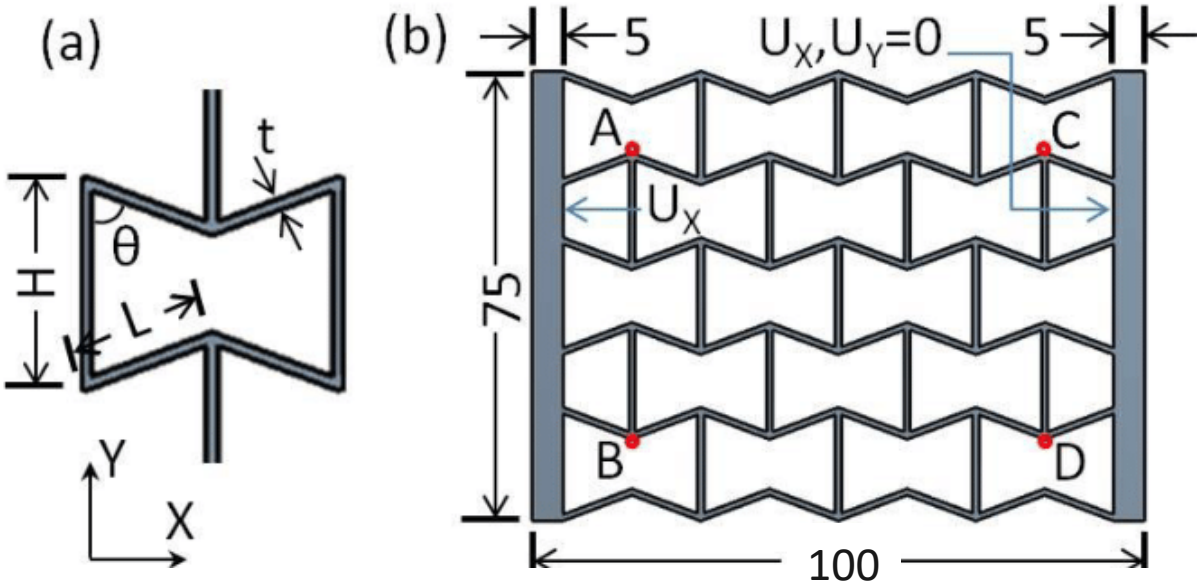

Figure 2.1 Re-Entrant Honeycomb Structure [21]

Re-Entrant star structures get their name from the voids that the structure itself creates during its expansion. The most common studied ones are:

- Three-Pointed Stars (Fig. 2.2i)
- Four-Pointed Stars (Fig. 2.2ii)
- Six-Pointed Stars (Fig. 2.2iii)

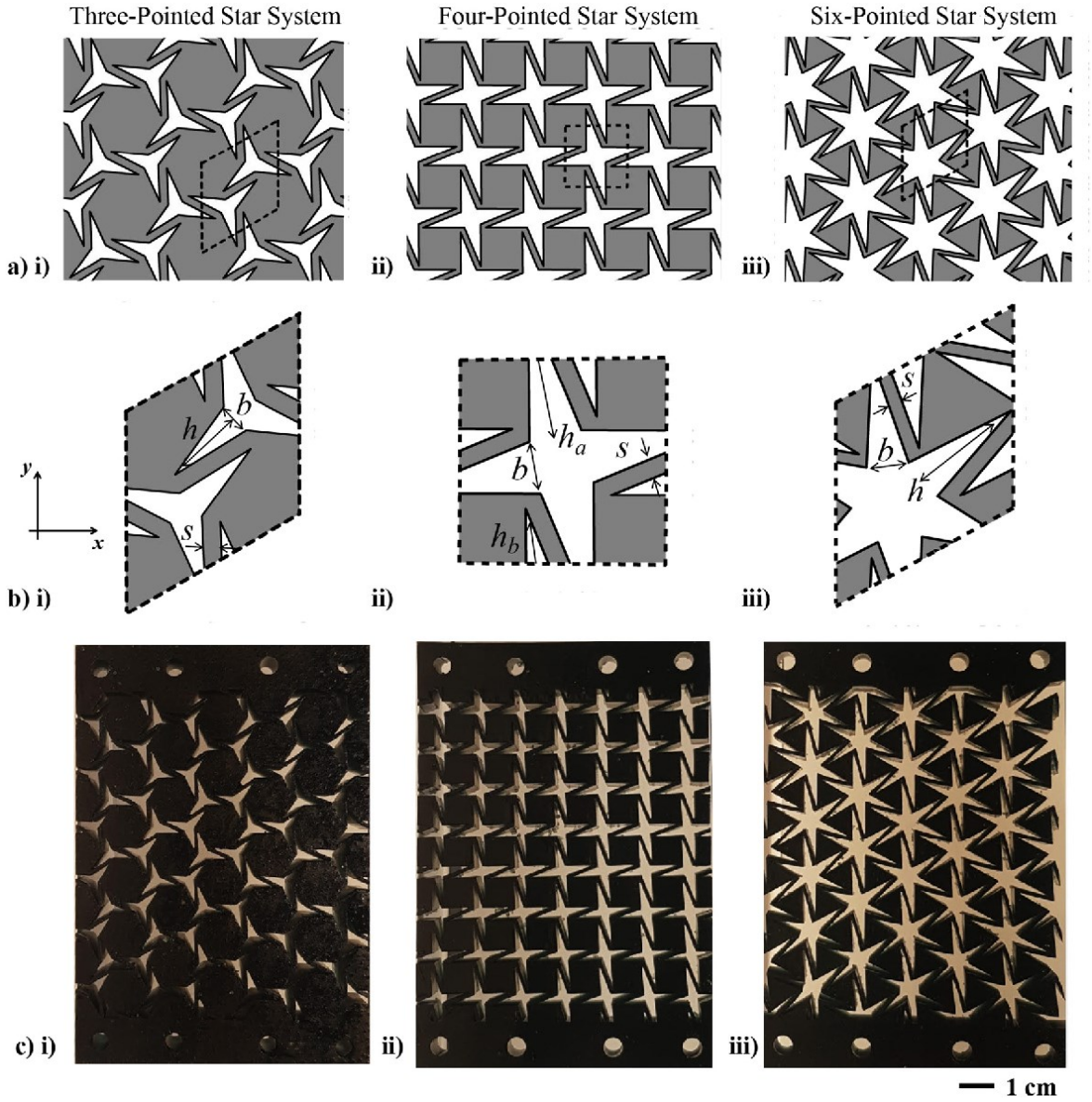

Figure 2.2 Re-Entrant Star Structures: i. 3 pointed stars, ii. 4 pointed stars, iii. 6 pointed stars [22]

2.2. Design process and SolidWorks modeling

Once the models had been determined, the CAD of the structure was designed using SolidWorks and COMSOL Multiphysics tools.

The first model to be preliminarily studied and designed was the unit cell of the honeycomb re-entrant structure. After checking that the desired behavior was indeed manifesting itself under tensile stress (Fig. 2.3), the next step was to proceed and design the 2D honeycomb re-entrant lattice.

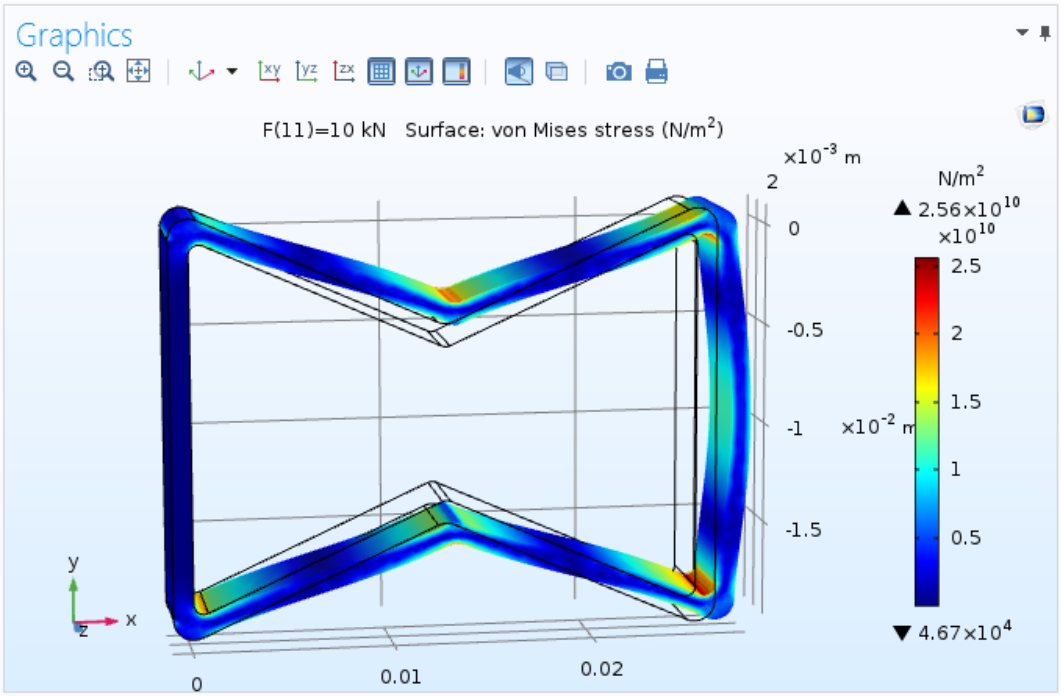

Figure 2.3 Desired behavior of the unit cell (Negative Poisson's Ratio) checked with COMSOL Multiphysics

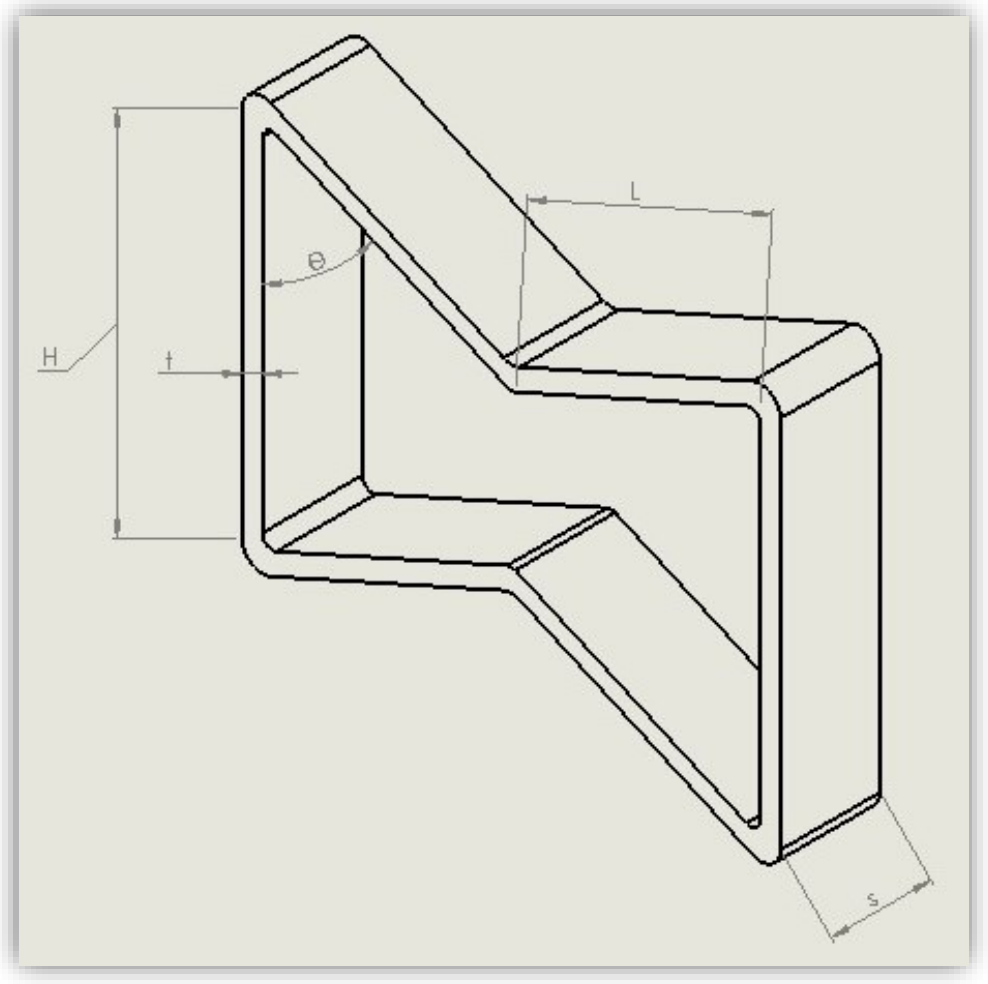

Figure 2.4 Unit Element of Honeycomb Re-Entrant Structure built with SolidWorks

The parameters chosen for the design (Figure 2.4) of the unit cell were the following:

- Angle θ=42°
- Height H=16 mm
- Length L=9 mm
- Thickness (Fig. 2.5): three cases were initially considered and tested:
  - t=1 mm
  - t=2 mm
  - t=3 mm

In order to properly print the structure with a 3D FDM printer, a certain thickness in the Z dimension had also to be defined. After testing different thicknesses among 1 mm, 3 mm, and 5 mm it was concluded that the ideal thickness was s=5 mm because the other two options led to a printed structure that was too thin to be tested accordingly.

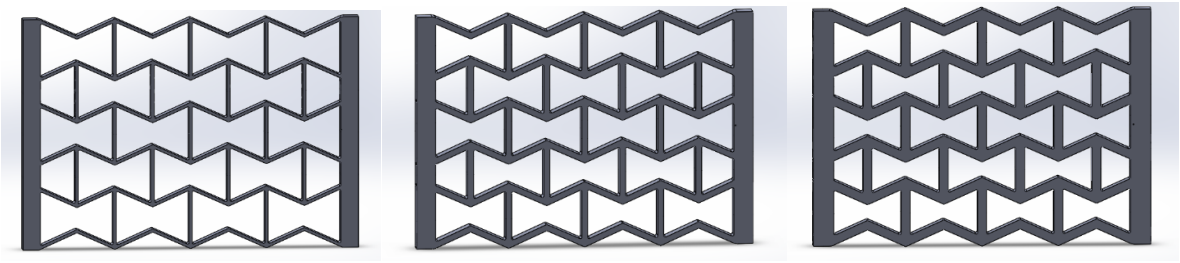

Figure 2.5 2D Honeycomb Re-Entrant Structure: (i) unit cell thickness 1 mm, (ii) unit cell thickness 2 mm, (iii) unit cell thickness 3 mm

On the other hand, as far as the Re-Entrant Star structure was concerned, the unit cell consisted of a void star-shape. The main difference between the honeycomb structure and the Star-shaped one is in fact that the latter works with voids instead of single unit cells combined together. This meant that the designing process was based on creating a hole with certain characteristics into a lattice and replicating that hole n times. Proceeding the same way as in the previous case, the parameters of the void (Fig. 2.6) were defined as follows:

- Width b=3.5 mm
- Height of the unit cell h=4.5 mm
- Space between the voids s=0.5 mm

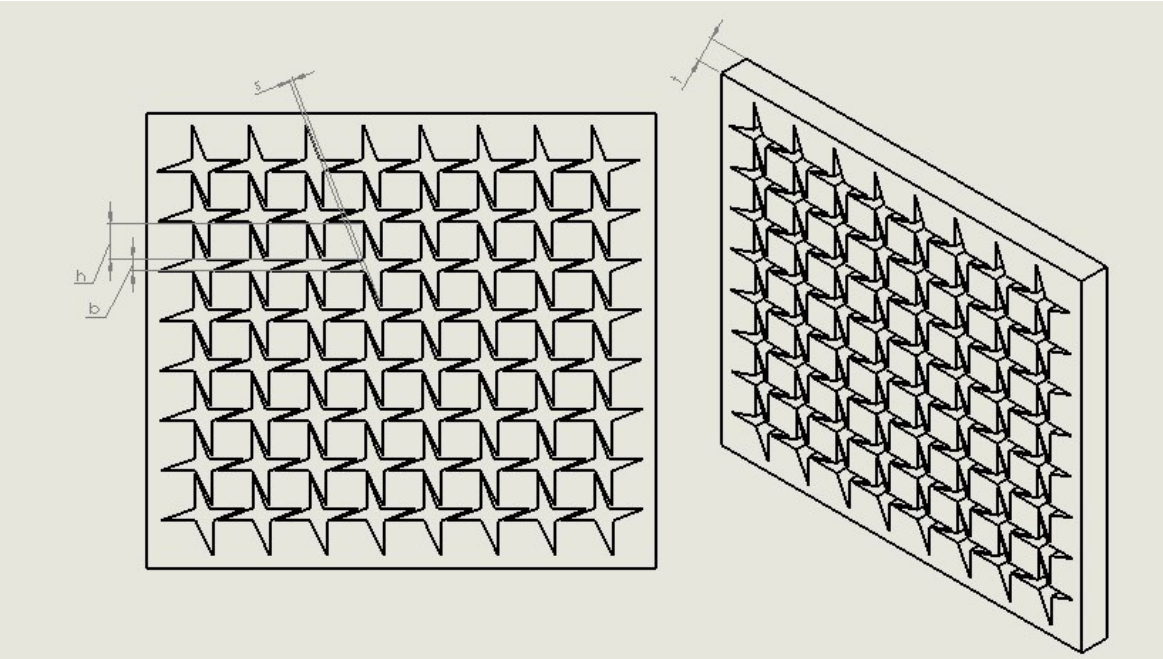

Figure 2.6 2D Re-Entrant Star Structure built with SolidWorks

Given some technical problems with the definition and propagation of those voids, as much as some technical difficulties during the printing process, it was decided later on to develop the Re-Entrant Star structure through the use of the CAD software made available in COMSOL Multiphysics (Fig. 2.7).

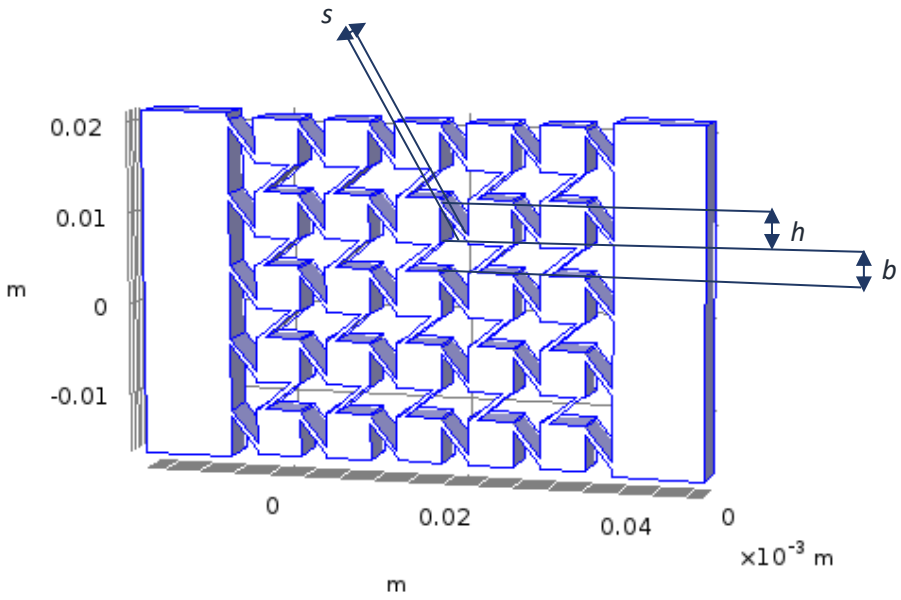

Figure 2.7 Perfected 2D Re-Entrant Star Structure built with COMSOL Multiphysics

Another important thing to keep into consideration while building those models was that the bidimensional lattices had to also have some borders specifically made for the gripping during the tensile tests.

Last but not least, the final step for both re-entrant designs was to develop their 3D models (Fig. 2.8). In order to do that, the honeycomb re-entrant structure had to be re-designed from scratch due to the superposition of the parts in a 45° angle. In fact, based on the information found in literature, the 3D model presents a unit cell composed by the superposition of two hourglass shape structures. As for the star shaped 3D model, cube-shaped unit cells had to be combined together and linked with each other diagonally.

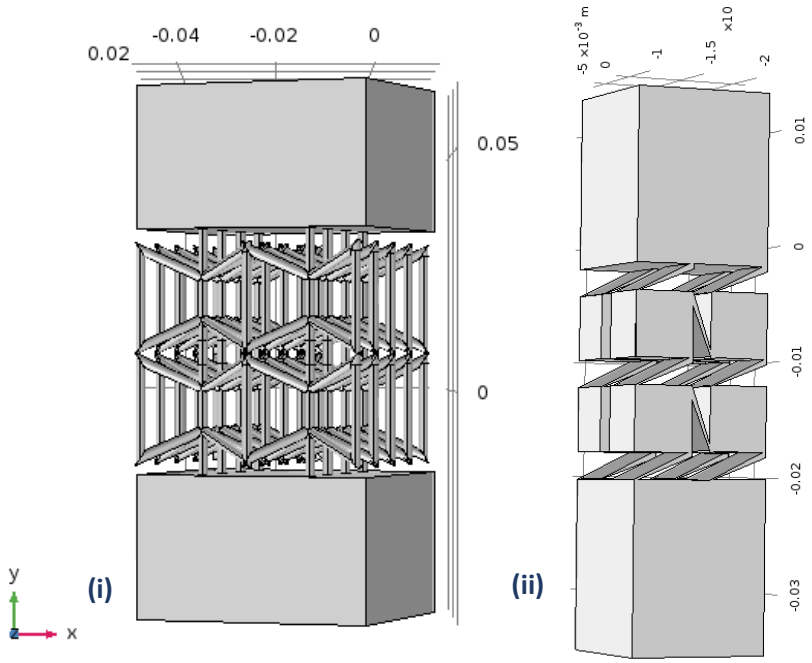

Figure 2.8 3D Re Entrant Models built using SolidWorks: (i) Re-Entrant Honeycomb, (ii) Re-Entrant Stars

In order to observe the behavior of the structures properly, it was also necessary to build different models to compare their results with. For this reason, two other models were built: a bulk one and a traditional lattice one.

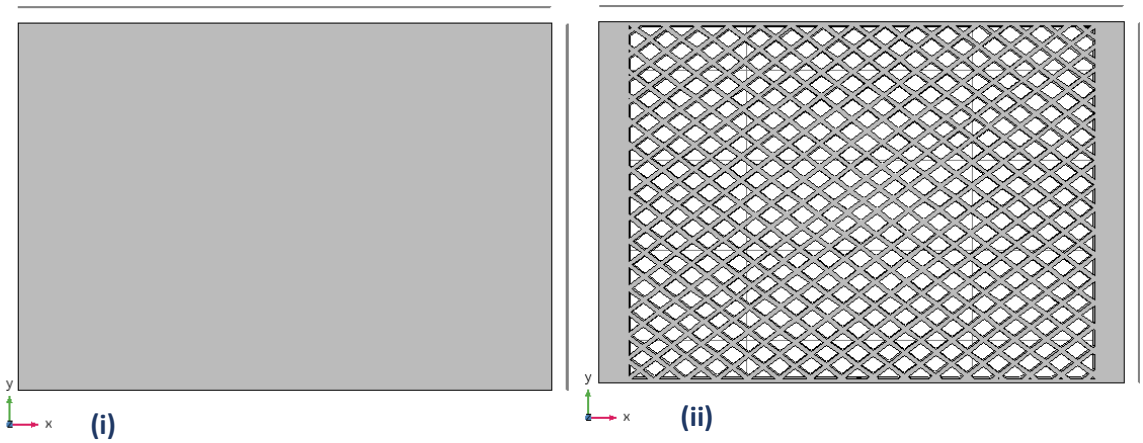

Figure 2.9 Comparison models made with SolidWorks: (i) Bulk, (ii) Traditional Lattice

2.3. Finite element analysis using COMSOL Multiphysics

Before testing the models experimentally, some mechanical and electrical tests were attempted to be done with the use of COMSOL Multiphysics.

As far as mechanics was concerned, the options selected for the mechanical study of the structure were:

- Space Dimension-3D
- Physics-Solid Mechanics (solid)
- Study-Stationary

Once the model had been imported as a CAD in COMSOL Multiphysics, a whole set of other parameters had to be discussed and properly selected. For a preliminary study and observation of the geometry, a generic type of PLA (Polylactic Acid) was considered.

The next step was to define the mechanical boundaries of the model. Given the study of the auxetic behavior and given the fact that the study had to simulate the work of a traction device, the boundaries defined were as follows:

- Fixed constraint on one side of the structure, perpendicular to the X direction
- Boundary load on the other side of the lattice, again perpendicular to the X direction. The load was defined as Total Force entirely applied on the X direction

When it was time to choose the mesh, different tests had to be done in order to check if there was a significant change in the results among ''Normal'' (Fig. 2.10), ''Fine'' (Fig. 2.11), and ''Finer'' (Fig. 2.12) mesh. From the results that came out, the different maximum stresses were compared:

- Normal Mesh: $1.18 * 10^8 \ \ N/m^2$
- Fine Mesh: $2.75 * 10^8 \ \ N/m^2$
- Finer Mesh: $3.4 * 10^8 \ \ N/m^2$

It was later concluded that there wasn't a significant change among the different mesh and that the ''Fine'' one was a good compromise and less computationally expensive.

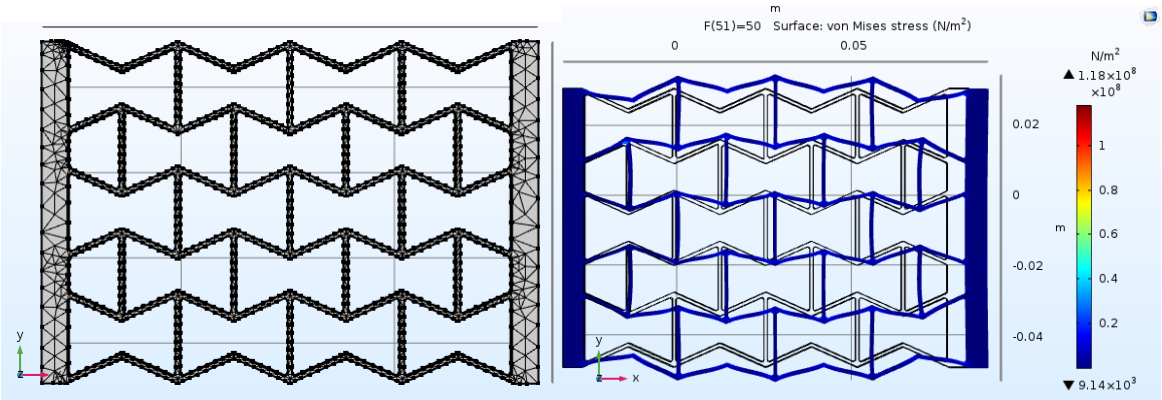

Figure 2.10 Normal mesh of Honeycomb Re Entrant Structure with COMSOL Multiphysics

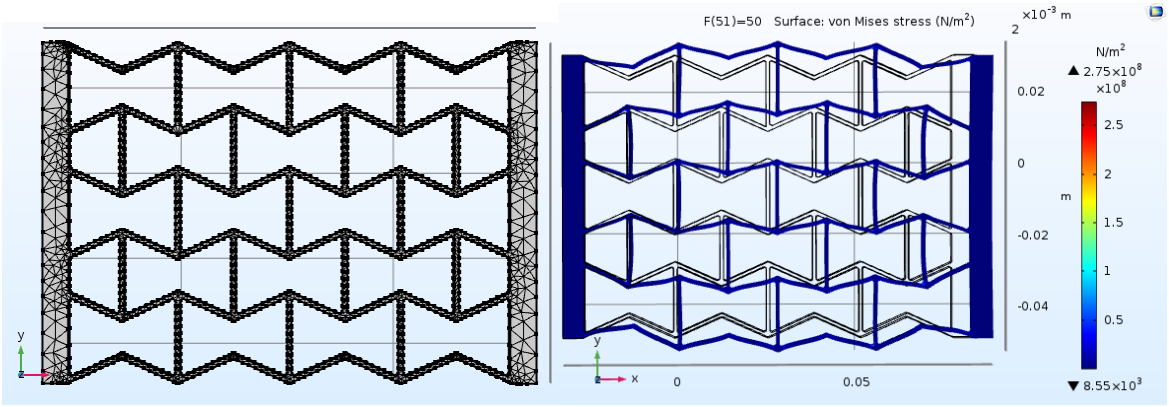

Figure 2.11 Fine mesh of Honeycomb Re Entrant Structure with COMSOL Multiphysics

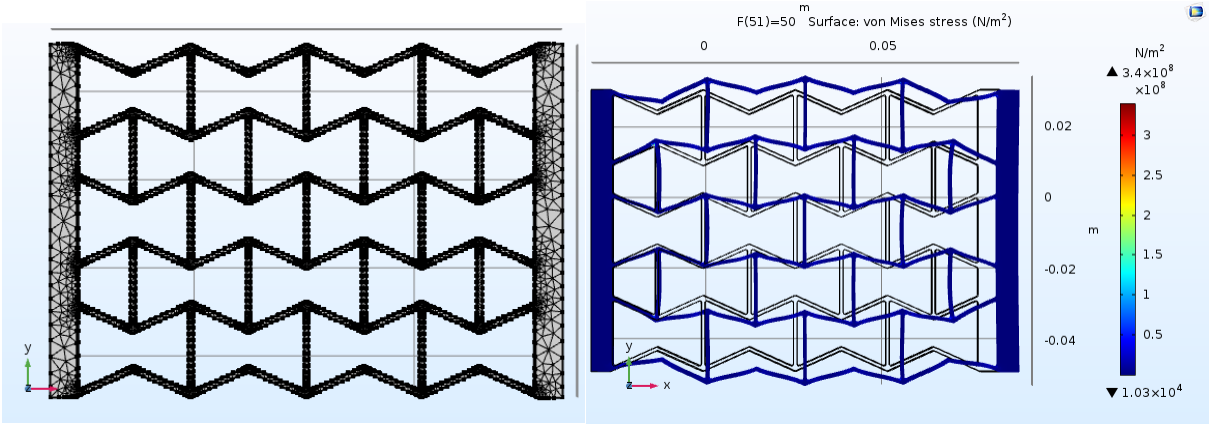

Figure 2.12 Finer mesh of Honeycomb Re Entrant Structure with COMSOL Multiphysics

Finally, attempts to study the electrical response of the structures were made, only to conclude that it wasn't possible for this study to determine the piezoresistive response of the structure with the use of that generic material and COMSOL Multiphysics. For this reason, that part of the study had to be entirely checked only through experimental tests.

3. Fabrication & Testing

3.1. Additive manufacturing methods

In order to experimentally fabricate and test the structures built in the previous chapter, additive manufacturing techniques were used. In particular, the main tool used was a 3D FDM (Fused Deposition Modeling) printer (Fig. 3.1) and, later on, a UV DPL (Digital Light Printing) printer was also considered.

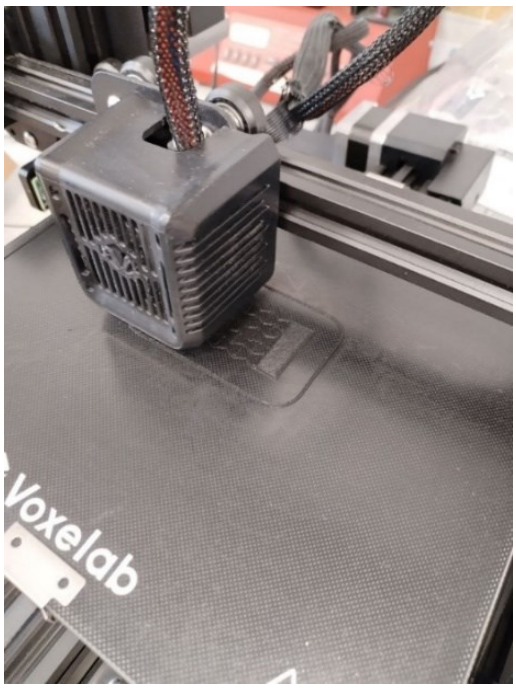

Figure 3.1 Filament 3D printer

According to [23] based on the majority of literature reports, auxetics derived from the honeycomb cell have been the ones mostly explored compared to other auxetic structures due to its simplicity of fabrication for complex 3D shaped models. Furthermore, those reports focus mainly on the theoretical modelling of the strain behavior of said models through the use of Finite Element Analysis (FEA). This study aims to show experimentally the potential of those structures with the aid of additive manufacturing techniques.

Setting aside possible technical difficulties related to the quality of printing and the characteristics of the 3D printer itself, it was possible to print and test multiple models. The printer itself resulted also versatile for the use of different materials.

In order to print with a 3D FDM printer, it was necessary to elaborate the models and choose the suitable parameters for the printing process through the use of a slicer software, in this specific case Cura was used. For this step, the main parameters to be chosen were the following:

- Printing Temperature
- Quality: 0.2mm

- Temperature of the bed: 65°C
- Filling percentage
- Type of filling
- Supports: none
- Build Plate Adhesion: Skirt, it consists of just a line printed around the model but not connected to it directly.
- Scale: 35%

As for the type of filling, initially, the very first structures were printed with a 20% filling and a tri-hexagon pattern (Fig. 3.2). It was later noticed that in order to improve the gripping during the traction test and to improve the conduction of the structure, a 100%-line filling (Fig. 3.3) was adopted. Finally, a 100%-concentric filling (Fig. 3.4) was also tested in order to check if the conduction was influenced in any way by the direction of the fibers of the printed models.

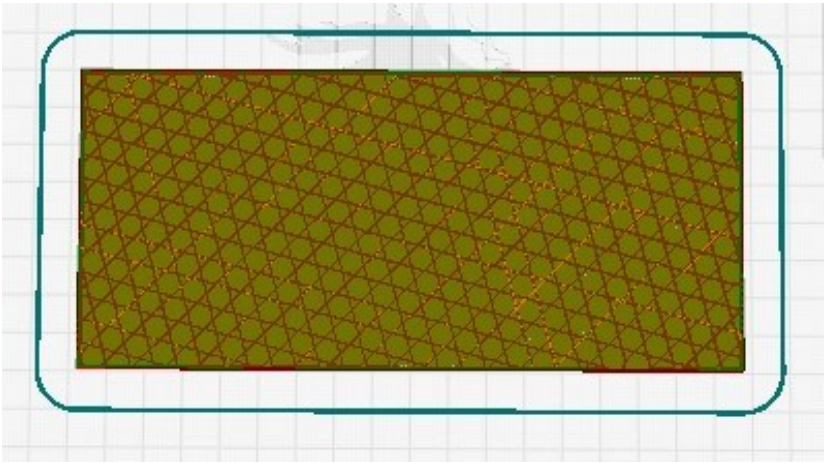

Figure 3.2 20% Tri-hexagon filling with Cura

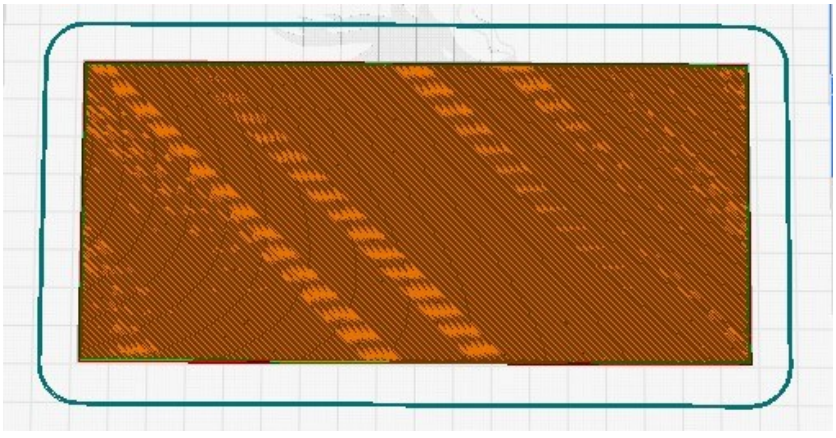

Figure 3.3 100% Lines filling with Cura

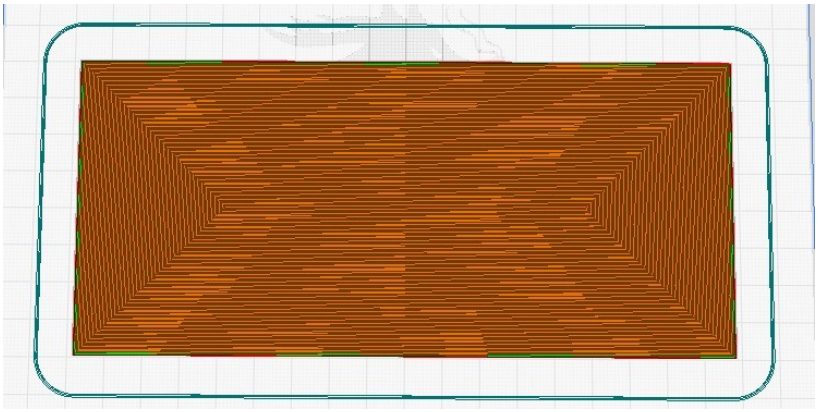

Figure 3.4 100% Concentric filling with Cura

3.2. Selection of 3D FDM filaments

As it was stated above, different materials were used during the printing process. As a consequence, the filaments used (Fig. 3.5) were the following:

- PLA - Black
- Conductive FilaFlex - Black
- Foamy FilaFlex - Grey
- PolyFlex TPU90 - White

Another reason for using additional types of filaments was also to test the piezoresistive effect of the structures under tensile and compressive stress. In fact, one of the new purchased filaments (Conductive FilaFlex), compared to the other ones that behaved as insulators, is a type of Polyurethane that allows electric conduction.

In addition to this, it is interesting to take note that the PolyFlex TPU90 filament has an equally interesting property which is its incredible flexibility. Compared to the other filaments, this one in particular was able to reach more than 300% of extension under tensile stress.

Lastly, it was finally decided to focus mainly on 3 among those filaments (PLA, Conductive FilaFlex and TPU90) due to their interesting properties and due to the fact that the Foamy FilaFlex led to some technical difficulties related to limits in the printing temperature of the printer used.

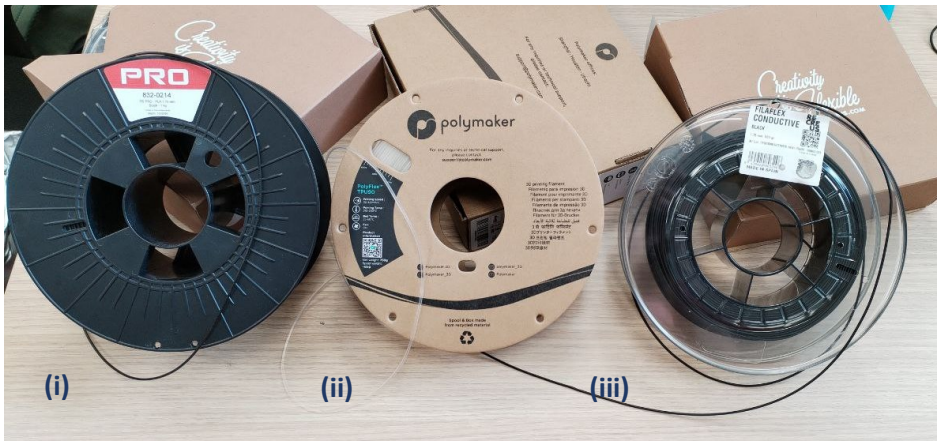

Figure 3.5 Filaments used: (i) PLA, (ii) TPU90, (iii) Conductive FilaFlex

It is important at this point to list in the table below the different filament specifications and the printing conditions that were used during the printing process (Table 1).

Table 1 Filament Specifications

Filament Type	Material	Density	Printing Temperature	Recommended Speed	Tensile Modulus
PLA	Polylactic Acid	1.3 $\frac{g}{cm^3}$	230°C	20-60 $\frac{mm}{s}$	3.5x10^3 MPa
Conductive FilaFlex	Conductive TPU FilaFlex	1.35 $\frac{g}{cm^3}$	260°C	20-40 $\frac{mm}{s}$	90 MPa
Foamy FilaFlex	Foamy TPU	1.050 $\frac{g}{cm^3}$	245-255°C	20-40 $\frac{mm}{s}$	-
PolyFlex TPU90	Thermoplastic polyurethane	1.12 $\frac{g}{cm^3}$	230°C	30-60 $\frac{mm}{s}$	6.17 MPa

Multiple models were printed and tested (Fig. 3.6-3.9) for the purpose of making some statistics out of the results. The goal was to print and test at least 3 models of each type in order to be able to evaluate statistically the behavior of said models.

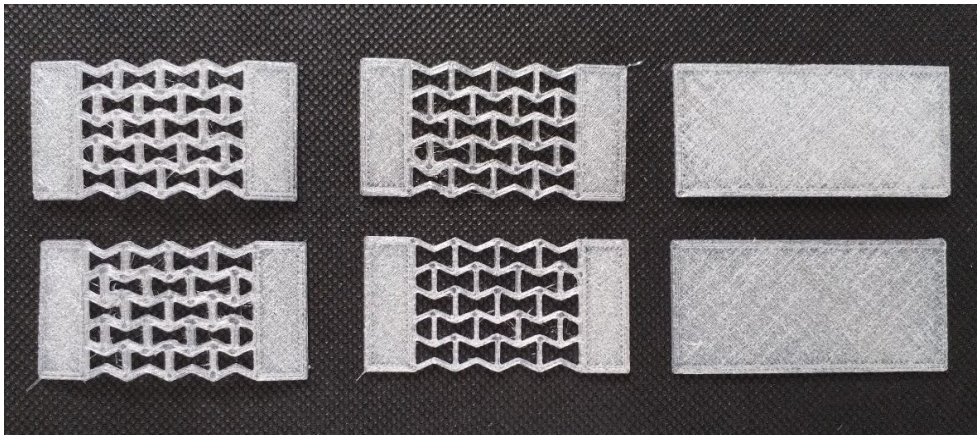

Figure 3.6 Example of PolyFlex TPU90 prints

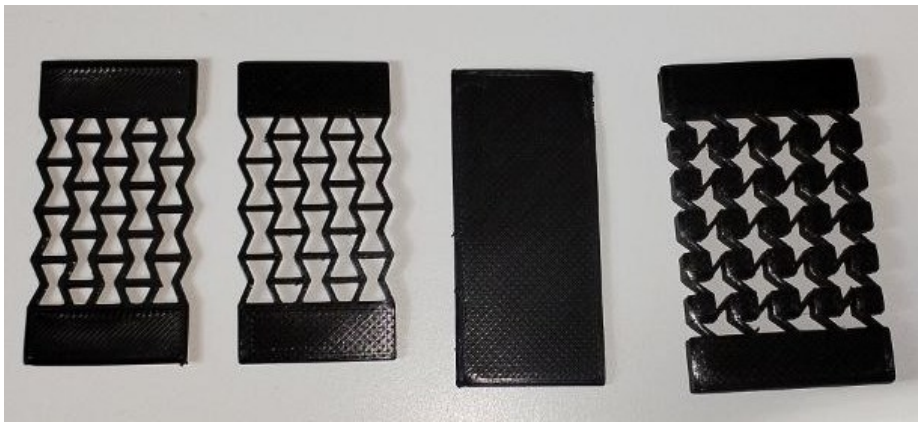

Figure 3.7 Example of PLA prints

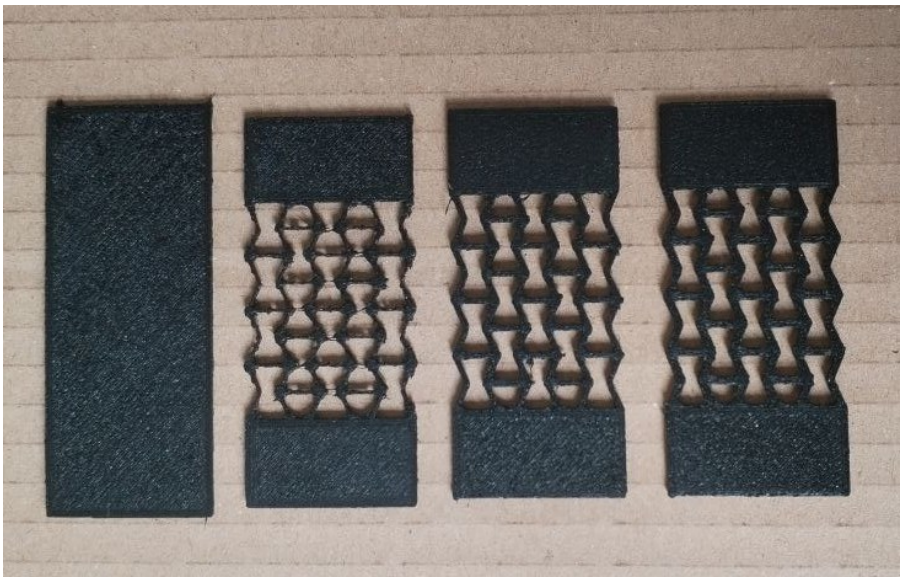

Figure 3.8 Example of Conductive FilaFlex prints

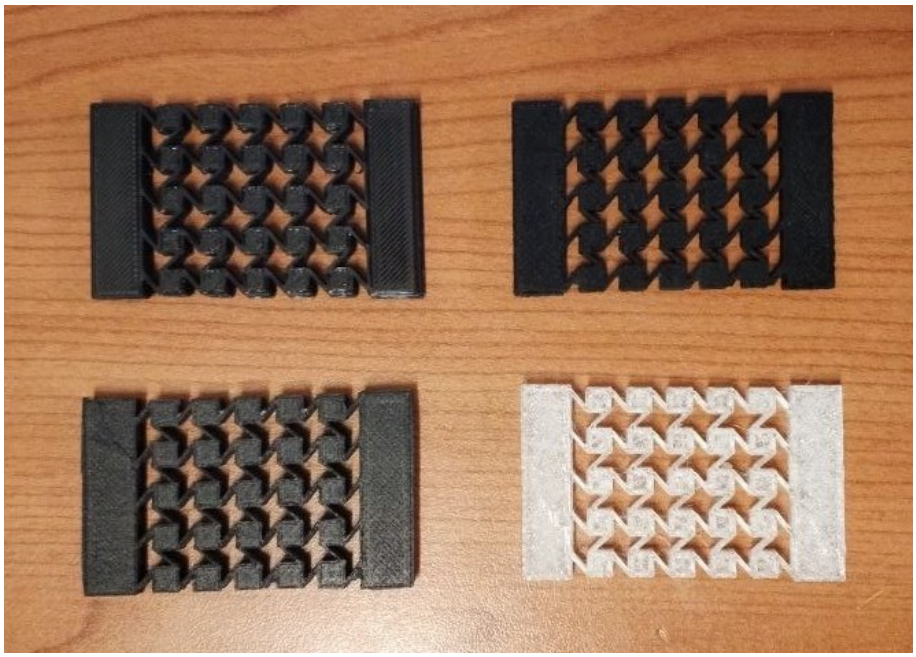

Figure 3.9 Re-Entrant Star models printed with the different filaments

3.3. UV light printing process

As an alternative, a more precise tool was used for more accurate measurements. Specifically, the UV DPL printer was used for the 3D models which, as explained before, were way more complex to print. This allowed higher resolution for smaller more complex structures and at the same time, given the material used (ionically conductive cellulose) it was also possible to get a more accurate measurement in the variation of resistance under tensile and compressive stress.

Additionally, compared to the FDM printer, the UV DPL one offered the advantage of printing way faster and, due to its principle, multiple models at once.

The main disadvantage, on the other hand, was that the material used for this process had to be made from scratch (Fig. 3.10) almost every single time due to the limited amount of ingredients available in the laboratory and also due to the fact that the composition had to be tested first before being used for the actual printing. That way, the quantity of materials wasted was reduced in case something went wrong with the composition of the cellulose.

Speaking of that, the recipe for that specific composition consisted in:

- ✓ Zinc Chloride (ZnCl2): 37.35%
- ✓ Distilled Water (DIW): 4.82%
- ✓ Acrylic Acid (AAc): 51.81%
- ✓ Microcrystalline *cellulose (MCC): 6.02%*
- ✓ *Photo initiator (TPO): 1.5% with respect to acrylates*

Once the cellulose had been tested, the next step was to actually print the structures. Even though this printing technique was used mainly for the complex 3D models (Fig. 3.12), some 2D models (Fig. 3.11) were also printed to compare their results with the filament printed models.

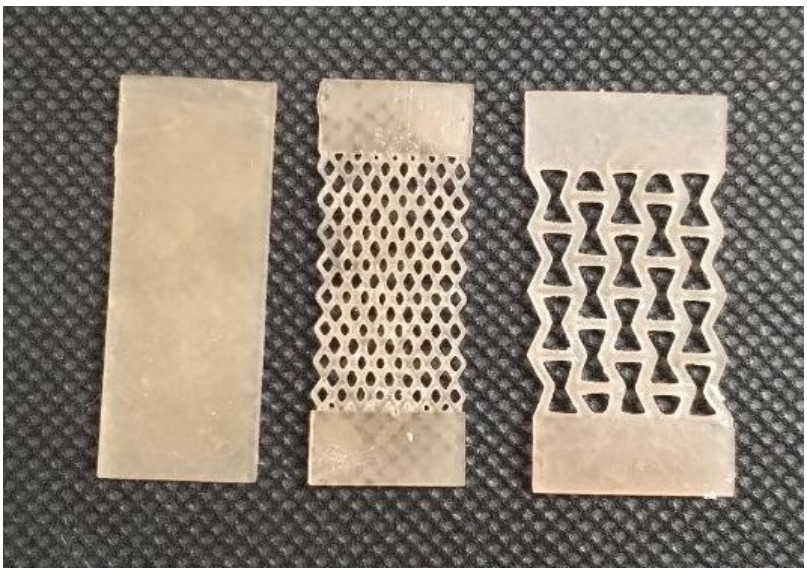

Figure 3.10 2D models printed with a UV DPL printer

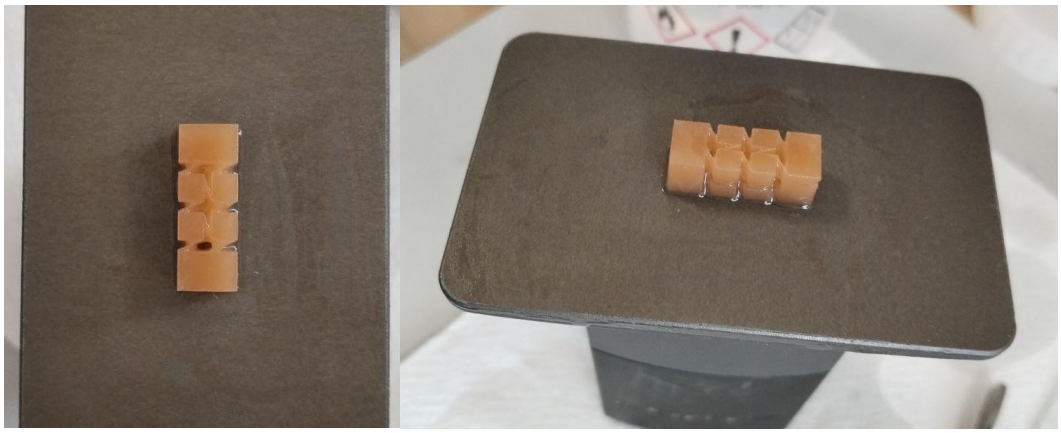

Figure 3.11 3D Re-Entrant Star model printed with a UV DPL printer

Like in the previous case, the use of a slicer software was necessary. For the UV DPL printer (Fig. 3.12), the slicer used was the software associated with the printer itself (Fig. 3.13).

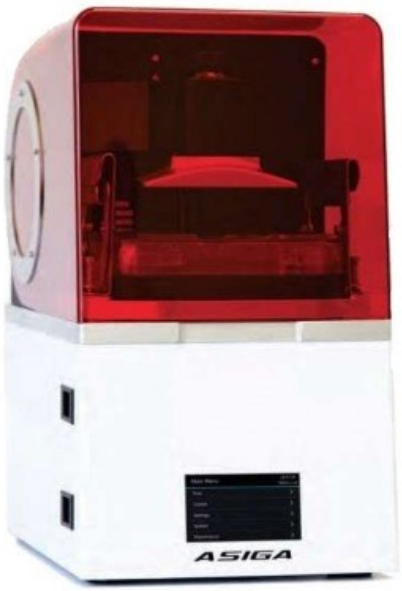

Figure 3.12 Asiga UV DPL printer

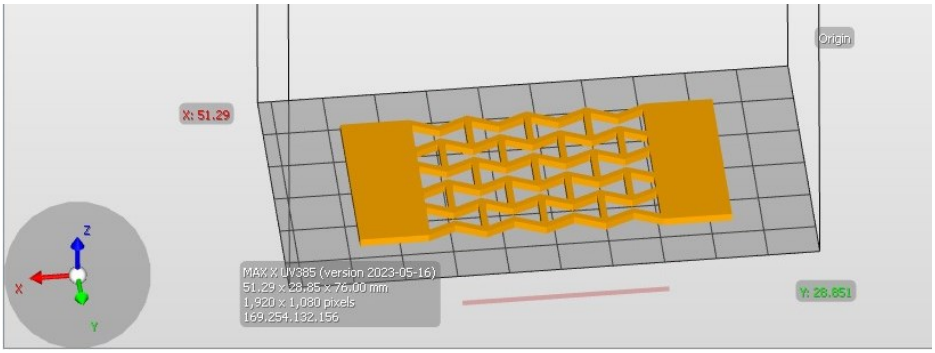

Figure 3.13 Asiga slicer for UV light printing: slicing of 2D Re-Entrant Honeycomb structure

A set of parameters had to be chosen accordingly and for the printing of the 2D structures or the 3D ones. In fact, for the 2D structures, the parameters used are showed in the table below (Table 2), with particular focus towards the ones underlined in green.

The parameters needed to be specified for two general layers. The ''burn-in'' column refers to the layer that would form against the build plate and securely hold the entire print during the building process. The ''1st layer'' column on the other hand, refers to all the other layers that compose the final model during the printing process.

Table 2 Parameter for the UV DPL printer for 2D Structures

Parameter	Burn-In	1st Layer	Units
Print Range From	0.000	0.200	mm
Print Range to	0.200	0.796	mm
Slice Thickness	0.050	0.050	mm
Slice Count	4	12	
Print Range Height	0.200	0.600	mm
Heater Temperature	0.0	0.0	°C
Minimum Temperature	0.0	0.0	°C
Heater Enable	0	0	
Light Intensity	30.08	28.08	$\frac{mW}{cm^2}$
Light Intensity Control	1	1	
Exposure Time	3.800	3.200	s
Z Compensation	0.000	0.000	mm
XY Compensation	0.000	0.000	mm
Support Exposure	100.00	100.00	%
Fill Exposure	100.00	100.00	%
Fill Noise	0.00	0.00	%
Border Exposure	100.00	100.00	%
Border Width	0.000	0.000	mm
Border Noise	0.00	0.00	%
Two Step Exposure Border Width	0.000	0.000	%
Separation Velocity	1.000	1.000	$\frac{mm}{s}$
Separation Acceleration	0.000	0.000	$\frac{mm}{s^2}$
Separation Deceleration	0.000	0.000	$\frac{mm}{s^2}$
Separation Distance	10.000	10.000	mm
Separation Detect Window	0	0	g

Separation Detect Window Time	0.000	0.000	s
Separation Detect Hard Stop	1	1	
Separation Pressure Limit	300.000	300.000	$\frac{g}{cm^2}$
Approach Velocity	1.000	1.000	$\frac{mm}{s}$
Approach Acceleration	0.000	0.000	$\frac{mm}{s^2}$
Approach Deceleration	0.000	0.000	$\frac{mm}{s^2}$
Approach Pressure Limit	100.000	100.000	$\frac{g}{cm^2}$
Tare Interval	0.001	0.001	mm
Pressure Hysteresis	5.00	5.00	%
Layer Tolerance	30.00	30.00	%
Viscosity Range	1.000	1.000	mm
Motor Timeout	300.000	300.000	s
Traverse Timeout Range	0.100	0.100	mm
Wait time (After Exposure)	1.000	1.000	s
Wait time (After Separation)	1.000	1.000	s
Wait time (After Approach)	0.000	0.000	s

In order to print the 3D structures instead, it was necessary to change some of the parameters in such a way that they could suit the characteristics of the 3D models. The parameters chosen in this case are listed in Table 3.

Table 3 Parameters for UV DPL printer for 3D structures

Parameter	**Burn-In**	**1st Layer**	**Units**
Print Range From	0.000	0.200	mm
Print Range to	0.200	0.796	mm
Slice Thickness	0.100	0.100	mm
Slice Count	4	12	
Print Range Height	0.200	0.600	mm
Heater Temperature	0.0	0.0	°C
Minimum Temperature	0.0	0.0	°C
Heater Enable	0	0	

Light Intensity	32.00	30.00	$\frac{mW}{cm^2}$
Light Intensity Control	1	1	
Exposure Time	4.000	3.500	s
Z Compensation	0.000	0.000	mm
XY Compensation	0.000	0.000	mm
Support Exposure	100.00	100.00	%
Fill Exposure	100.00	100.00	%
Fill Noise	0.00	0.00	%
Border Exposure	100.00	100.00	%
Border Width	0.000	0.000	mm
Border Noise	0.00	0.00	%
Two Step Exposure Border Width	0.000	0.000	%
Separation Velocity	1.000	1.000	$\frac{mm}{s}$
Separation Acceleration	0.000	0.000	$\frac{mm}{s^2}$
Separation Deceleration	0.000	0.000	$\frac{mm}{s^2}$
Separation Distance	10.000	10.000	mm
Separation Detect Window	0	0	g
Separation Detect Window Time	0.000	0.000	s
Separation Detect Hard Stop	1	1	
Separation Pressure Limit	300.000	300.000	$\frac{g}{cm^2}$
Approach Velocity	1.000	1.000	$\frac{mm}{s}$
Approach Acceleration	0.000	0.000	$\frac{mm}{s^2}$
Approach Deceleration	0.000	0.000	$\frac{mm}{s^2}$
Approach Pressure Limit	100.000	100.000	$\frac{g}{cm^2}$
Tare Interval	0.001	0.001	mm
Pressure Hysteresis	5.00	5.00	%
Layer Tolerance	30.00	30.00	%
Viscosity Range	1.000	1.000	mm
Motor Timeout	300.000	300.000	s
Traverse Timeout Range	0.100	0.100	mm

Wait time (After Exposure)	1.000	1.000	s
Wait time (After Separation)	1.000	1.000	s
Wait time (After Approach)	0.000	0.000	s

3.4. Testing methods

The main goal of this study was testing the printed models mechanically and electrically. After collecting the experimental data, it was possible to compare the experimental results with the simulations done beforehand and it was finally possible to make some observations accordingly.

3.4.1. Mechanical testing

Not all printed structures had conductive properties. This means that those structures got tested only mechanically under tensile stress. Tension was performed by the Tensile Test Z5 machine and was controlled through the use of the THSSD software.

Tensile tests had to be done by taking into consideration that the maximum load available for that machine was: 500N. Ideally, the test was meant to break all models in order to evaluate the statistics of the behavior of the different structures made with different filaments but not every structure reached the breaking point. In fact, structures made with the TPU90 filament were unable to break, instead they reached at low forces very high extensions of even 300% (Fig. 3.14).

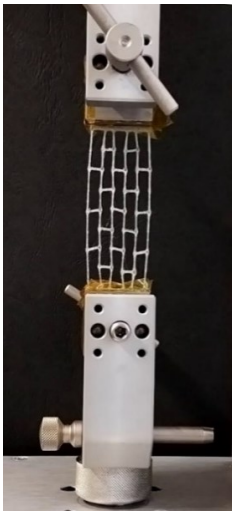

Figure 3.14 Elongation of Honeycomb Re-Entrant Structure with TPU90 filament

In order to test the structures under tensile stress, the following parameters were chosen for the occasion:

- Force: 400N
- Speed: 10 $\frac{mm}{min}$

It is important to note at this point that for the conductive structures some additional measures had to be taken. Given the conductive surface of the grippers, it was necessary to insulate the contact between the structure itself and the grippers through the use of an insulating tape so the electrical data wouldn't be affected by too much noise.

Furthermore, even though most of tests were carried out under tensile stress, the 3D star re-entrant structure printed with our customized resin, was also tested under compression. Throughout this experiment, it was noticed in fact, that once compressed, the structure started behaving as a bulk model (Fig. 3.15).

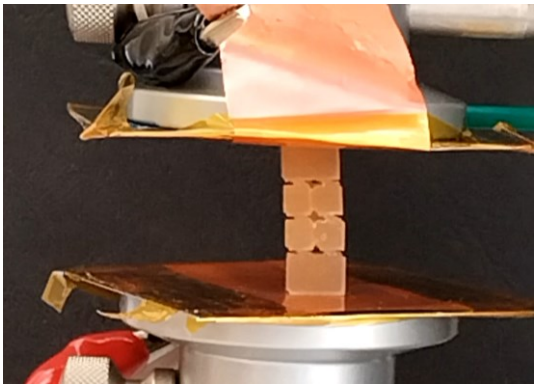

Figure 3.15 Compression test of 3D Star Re-Entrant model

The data obtained from those tests were then processed through the use of the software Origin Lab. In particular, the only data available from the THSSD software were related to the elongation of the height of the sample and the force used. Data involving the elongation in the Y direction had to be extrapolated by measuring manually the elongation using the frames of videos taken during said tests.

The first thing that was noticed during those tests by the naked eye, was that the structures were behaving exactly as a model with a negative Poisson's ratio would (Fig. 3.17), compared to the bulk and traditional lattice structures which appeared thinner and thinner the more the structure was stressed (Fig. 3.16).

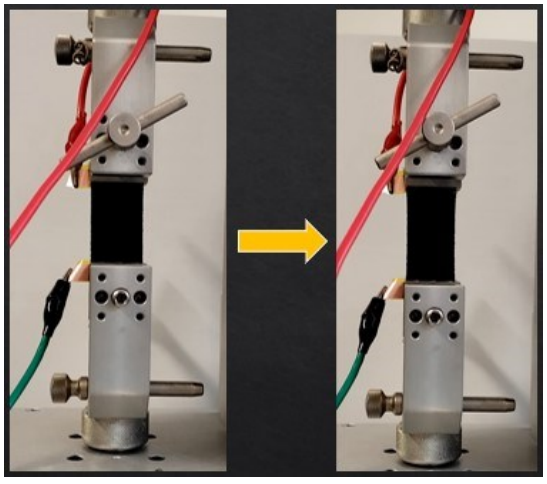

Figure 3.16 Elongation of Bulk 2D structure

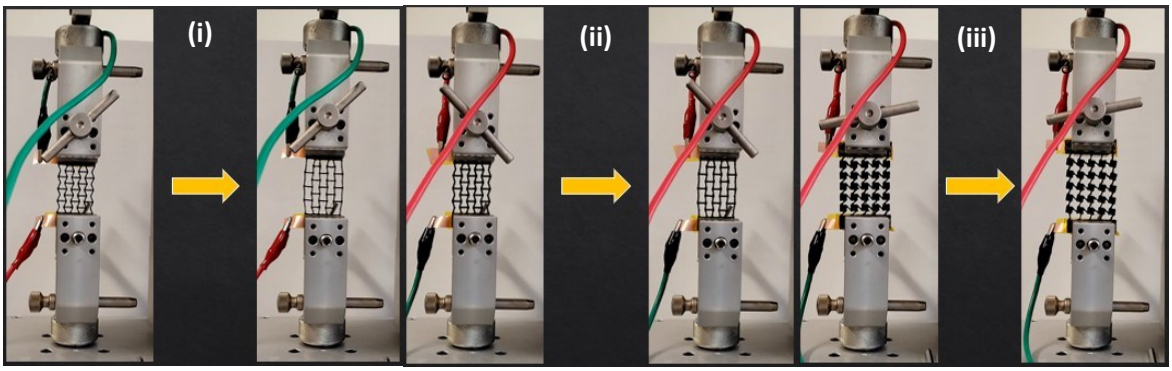

Figure 3.17 Elongation of 2D auxetic structures: (i) Honeycomb Re-Entrant Structure with unit element thickness of 2mm, (ii) Honeycomb Re-Entrant Structure with unit element thickness of 3mm, (iii) Star Re-Entrant structure

3.4.2. Electrical testing

The electrical test was carried out with the use of a Keithley 2400 multimeter while the data acquisition was executed using a specific LabVIEW program for the occasion. The main goal was to evaluate the variation of resistance in the structure once the latter was under stress. That way, it was possible to define and evaluate the piezoresistive behavior of the structure itself.

As stated above, for the electrical test it was necessary to isolate the grippers from the models by using an insulating tape. Some thin strips of copper electrodes were also added to both extremities of the structure in order to connect the structure to the multimeter (Fig. 3.18).

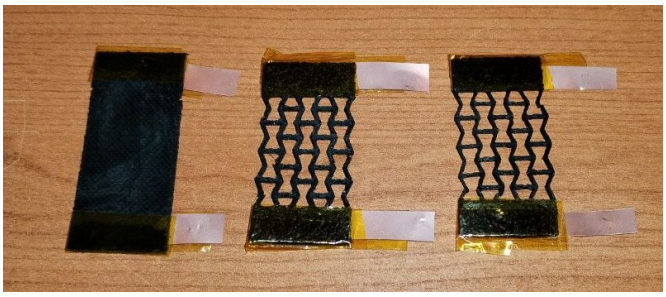

Figure 3.18 2D structures made with conductive FilaFlex and connected to some thin strips of copper electrodes and insulated with insulating tape

An additional test was to evaluate the variation of resistance by connecting this time the multimeter to the two sides of the structures instead of the two extremities. For this reason, it was necessary to connect the models and the multimeter in such a way that the wires wouldn't compromise the mechanical test. The solution was found in the use of a thin metallic wire (Fig. 3.19).

Two attempts were made to connect said wire to the structures:

- Attempt #1: a silver paste was used (Fig. 3.20-3.22)
- Attempt #2: a drop of liquid cellulose was used

Figure 3.19 conductive wire used for the lateral electrical test

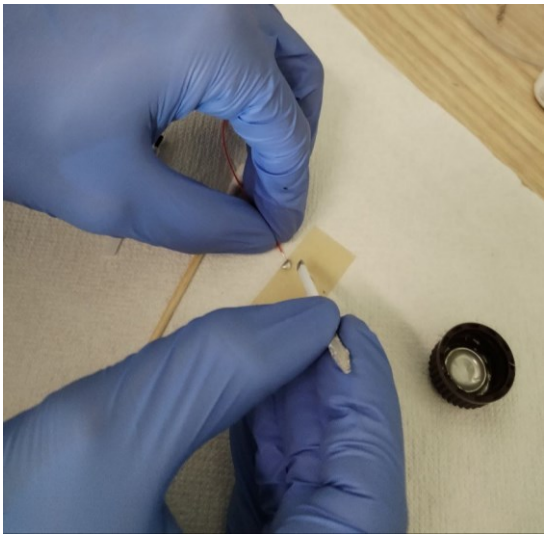

Figure 3.20 silver paste used for the lateral electrical test

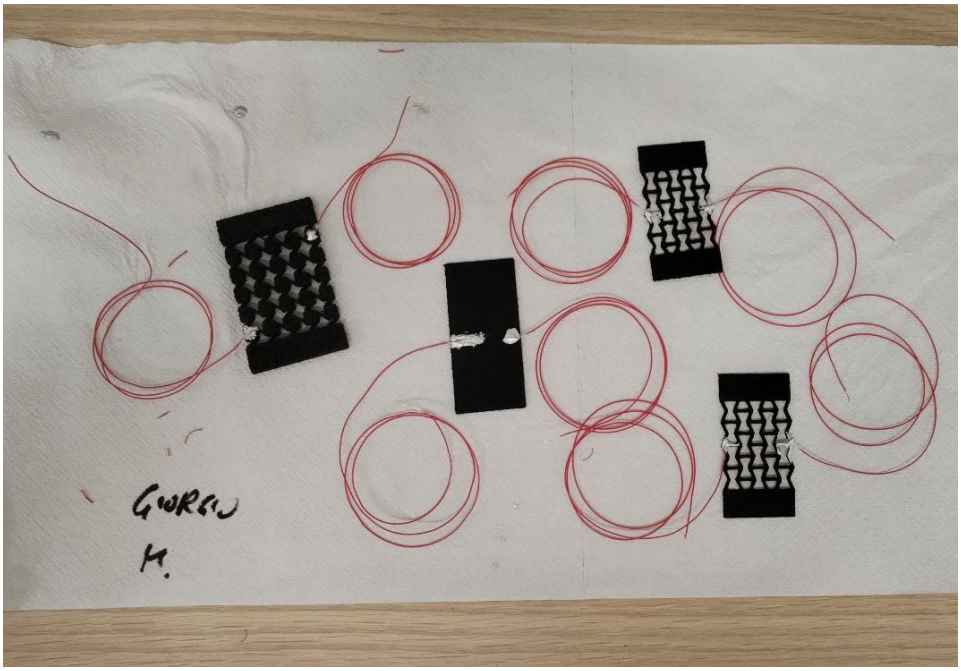

Figure 3.21 Filament printed structures connected with a conductive wire through the use of a silver paste

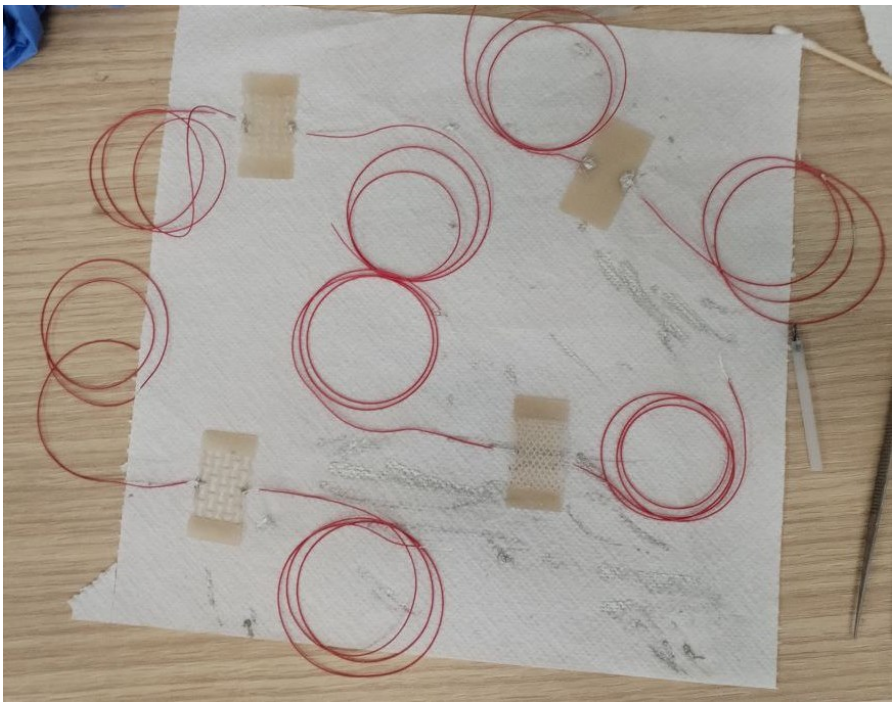

Figure 3.22 Cellulose structures connected with a conductive wire through the use of a silver paste

4. Results and Discussion

In this chapter, all the evaluations conducted throughout this study are presented and analyzed. It was essential not only to compare the simulation results with the obtained experimental data but also to interpret the behavior of the models through careful observation of these graphs.

- ***Elasticity and Young's Modulus (Graph εx-σx)***

  As illustrated by the graphs below, each model exhibited distinct stiffness characteristics based on its geometrical structure.

  To facilitate a clearer analysis and interpretation, the graphs were grouped according to the materials used (Fig 4.1-4.3). This grouping provided a more lucid and comprehensive understanding of the data.

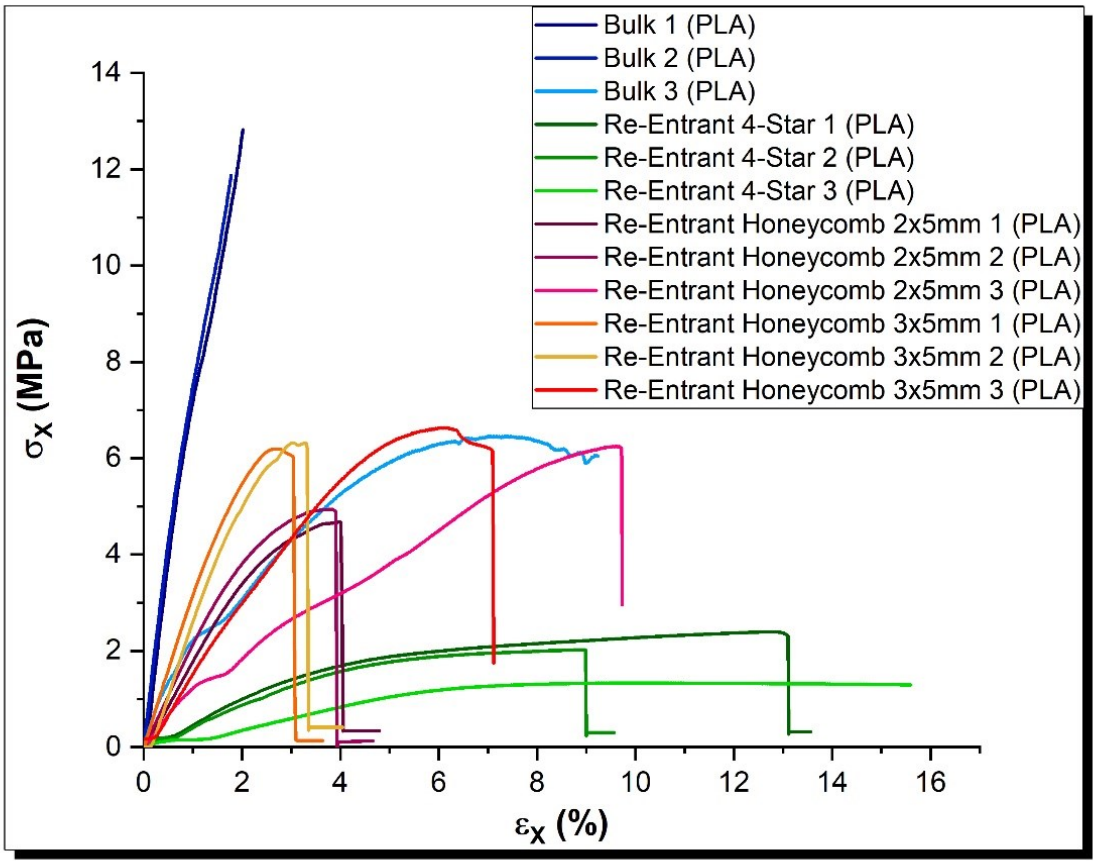

Figure 4.1 Graph εx-σx for models printed with PLA: blue-Bulk models, green-Re Entrant 4-Star models, purple-Re Entrant Honeycomb 2x5mm models, orange-Re Entrant 3x5mm models

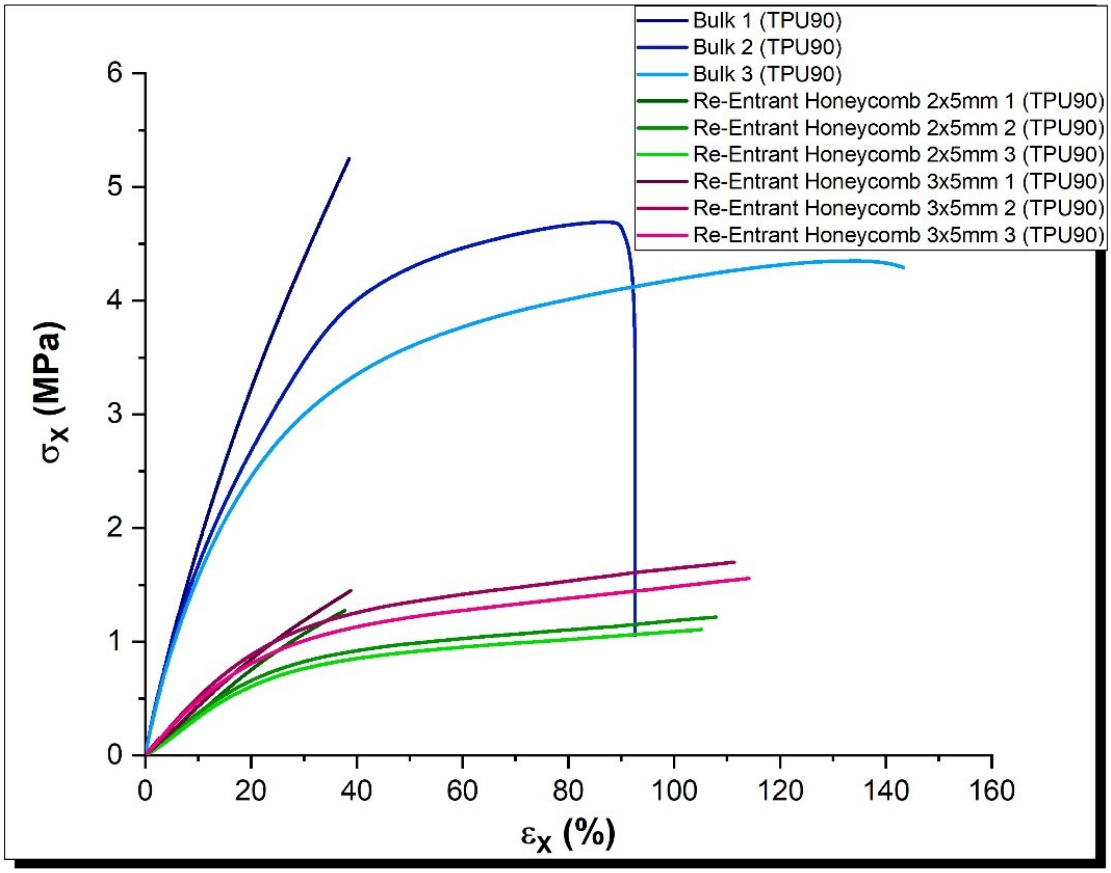

Figure 4.2 Graph εx-σx for models printed with TPU90: blue-Bulk models, green-Re Entrant Honeycomb 2x5mm models, purple-Re Entrant 3x5mm models

In fact, regardless of the material, a discernible pattern emerged. For instance, bulk models exhibited the highest Young's moduli in comparison to the auxetic models. It was also evident that, as anticipated, the Re-Entrant Honeycomb 3x5mm structures were more rigid than their thinner counterparts, the Re-Entrant Honeycomb 2x5mm structures. Furthermore, the Re-Entrant 4-Star models had an even smaller slope, indicating they were less rigid than the other auxetic models.

This behavior can be succinctly explained by stating that the introduction of voids into the structure reduces the Young's modulus of the latter, thereby increasing its elasticity.

Finally, the approximate values of the Young's moduli for the printed models were determined by considering only the initial portion of the curves, typically at 5% elongation.

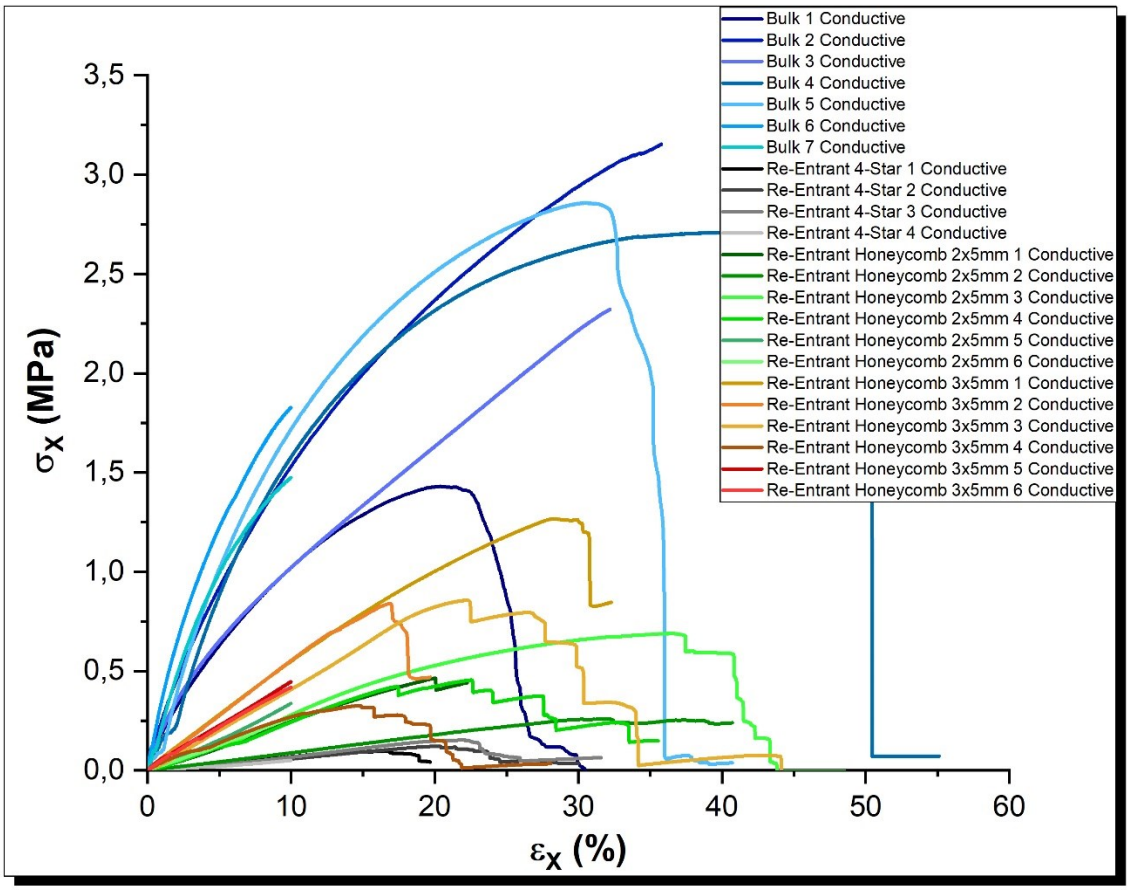

Figure 4.3 Graph εx-σx for models printed with Conductive FilaFlex: blue-Bulk models, grey-Re Entrant 4-Star models, green-Re Entrant Honeycomb 2x5mm models, orange-Re Entrant 3x5mm models

The Young's modulus can be evaluated graphically by using the following equation:

$$E = \frac{\sigma}{\varepsilon} = \frac{F/A}{dl/l}$$

σ is the normal tensile stress applied

ε is the strain along the X axis per unit length

Due to the non-linear nature of the experimental data curves, it was necessary to graphically approximate said curves linearly before performing any calculations (Fig. 4.4-4.6).

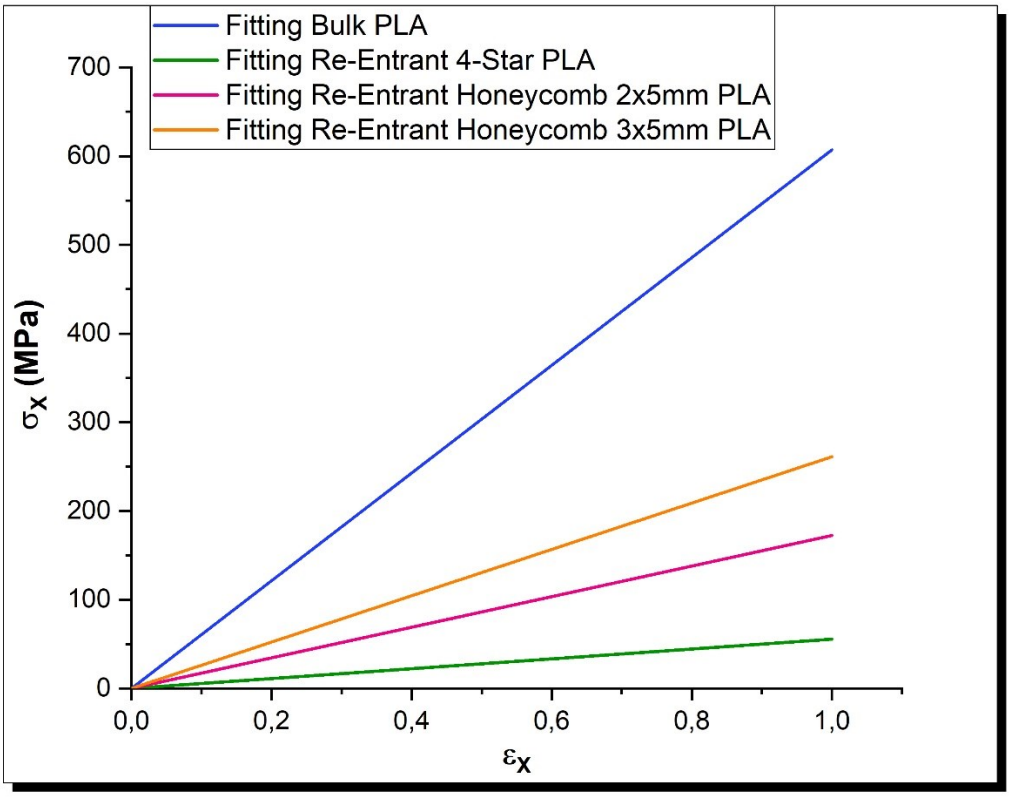

Figure 4.4 Graphical Evaluation of Young's Modulus for structures printed with PLA

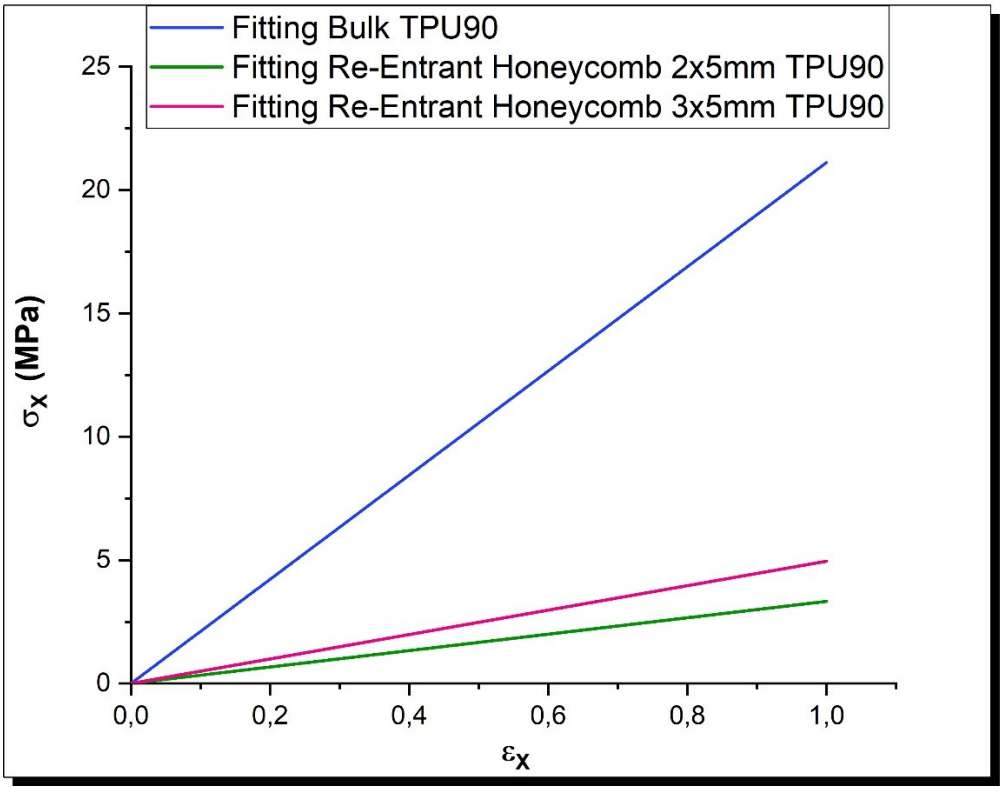

Figure 4.5 Graphical Evaluation of Young's Modulus for structures printed with TPU90

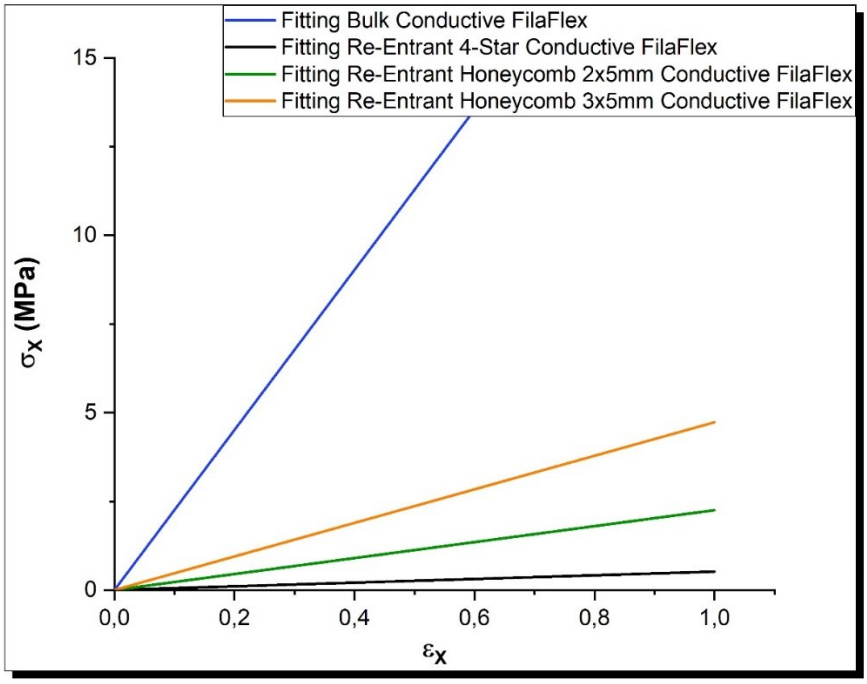

Figure 4.6 Graphical Evaluation of Young's Modulus for structures printed with Conductive FilaFlex

Regarding the models printed with ionically conductive cellulose, all structures exhibited a more elastic behavior compared to those printed with the 3D FDM printer. However, the bulk models still demonstrated a steeper slope than the Re-Entrant structures or the traditional lattice (Fig. 4.7).

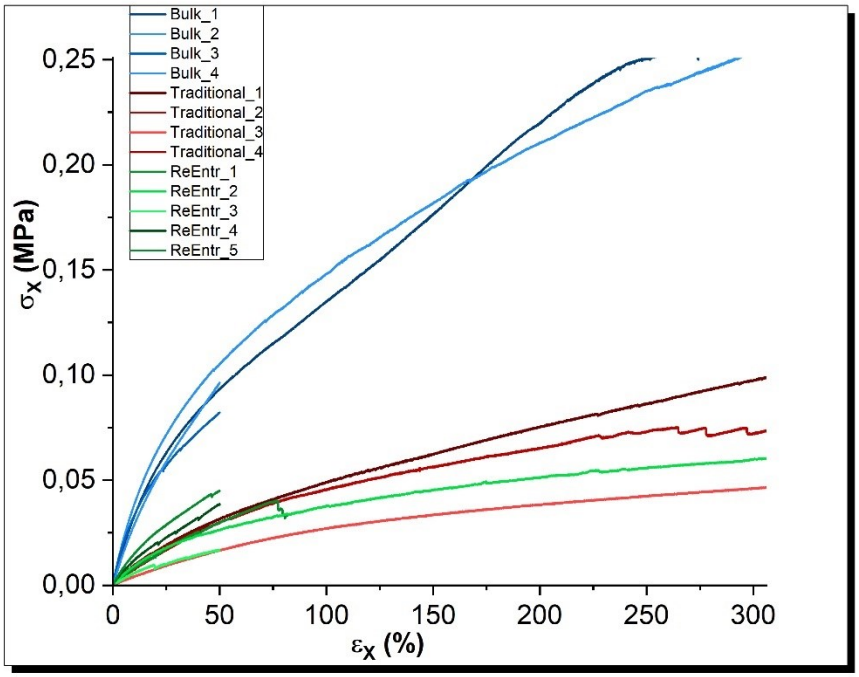

Figure 4.7 Graph εx-σx for models printed with ionically conductive cellulose

The results of these evaluations are subsequently detailed in the table below:

Table 4 Approximation of Young's Modulus from experimental data

	PLA	TPU90	Conductive FilaFlex	Cellulose
Bulk	607.127 MPa	21.111 MPa	22.570 MPa	0,367 MPa
Traditional Lattice	-	-	-	0,405 MPa
4-Star Re Entrant	55.556 MPa	-	0.519 MPa	-
2x5mm Honeycomb Re Entrant	172.371 MPa	3.333 MPa	2.250 MPa	-
3x5mm Honeycomb Re Entrant	261.111 MPa	4.958 MPa	4.729 MPa	0,112 MPa

- ***Poisson's Ratio ν (Graph εx-εy)***

Given the primary objective of this study, the next factor to be evaluated and compared with the simulations was the Poisson's ratio.

By definition, Poisson's ratio is an elastic parameter, and it is defined as the ratio of the absolute value of the lateral strain (Y axis) and the axial (X axis) one whenever a uniaxial tension is applied.

$$\nu = -\frac{\varepsilon_y}{\varepsilon_x}$$

ε_Y is the lateral strain along the Y axis

ε_X is the axial strain along the X axis

In conventional structures, the Poisson's ratio is typically positive, as the structure attempts to maintain a constant volume. Conversely, in auxetic structures, the Poisson's ratio is negative because the volume of the structure changes under applied uniaxial stress.

To evaluate the lateral strain, it was necessary to measure lateral deformation by extracting frames from laboratory videos. These measurements, initially in pixels, were then converted into millimeters, inevitably introducing some errors. Consequently, the graphical results of the experimental data did not exhibit a linear behavior compared to the simulations. Despite this, the behavior of the models closely approximated the results obtained with COMSOL Multiphysics for each geometry.

The graphs in question are reported below (Fig. 4.7-4.10).

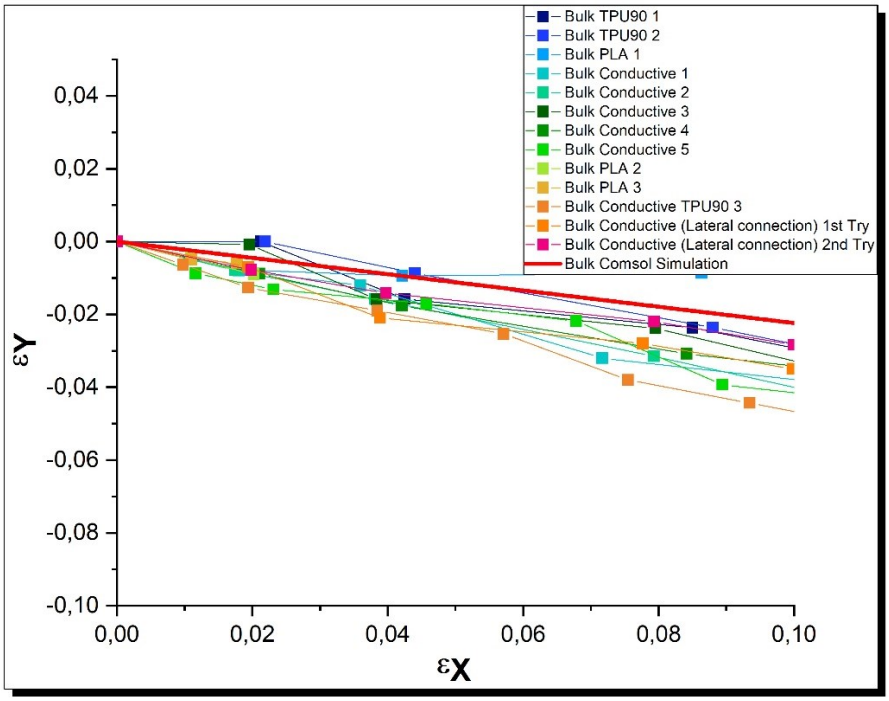

Figure 4.8 Graph εx-εy: Poisson evaluation for Bulk models vs simulation

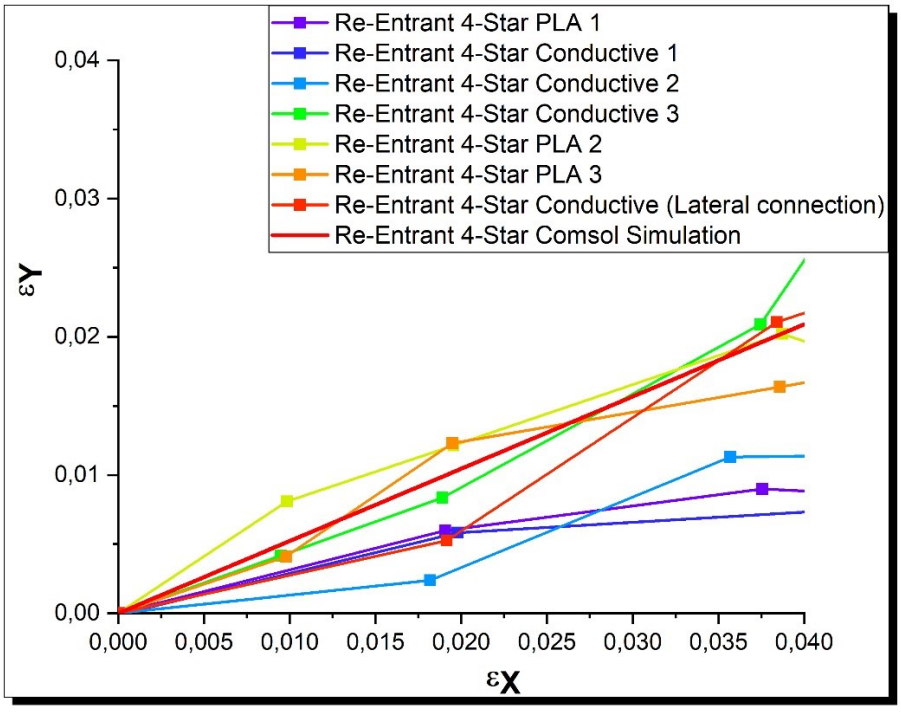

Figure 4.9 Graph εx-εy: Poisson evaluation for Re-Entrant 4-Star models vs simulation

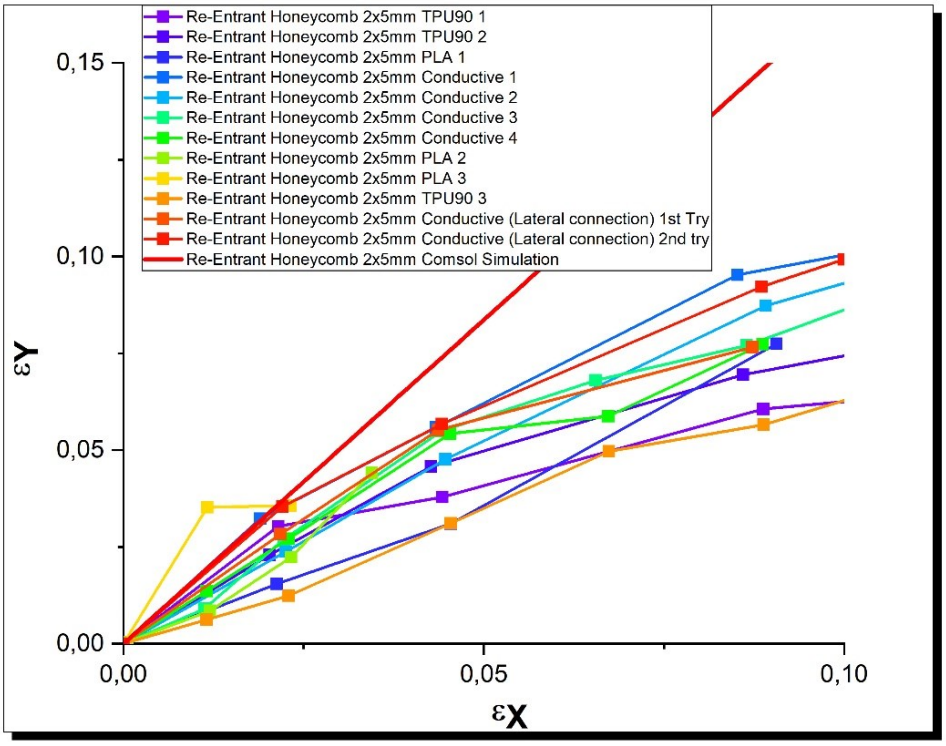

Figure 4.10 Graph εx-εy: Poisson evaluation for Re-Entrant Honeycomb 2x5mm models vs simulation

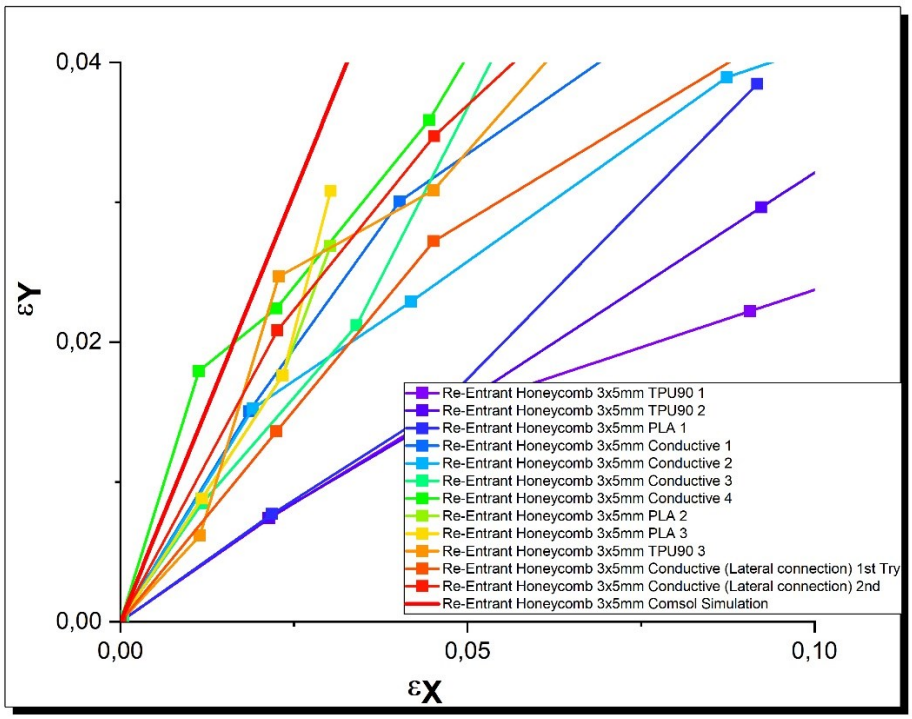

Figure 4.11 Graph εx-εy: Poisson evaluation for Re-Entrant Honeycomb 3x5mm models vs simulation

The comparison of the evaluated Poisson's ratios through the experimental data is presented in the following table. Notably, the overall behavior closely aligns with the simulation results.

Table 5 Poisson's ratio: Real vs Simulation

	Simulation	Experimental Data
Bulk	0.283	0.500
Traditional Lattice	-	-
4-Star Re Entrant	-0.500	-0.567
2x5mm Re Entrant Honeycomb	-1.760	-1.187
3x5mm Re Entrant Honeycomb	-1.250	-0.843

- ***Piezoresistive Behavior (Graph ⊿R/Ro-t)***

In this section, several additional considerations were necessary.

The objective was to evaluate the variation of resistance over time during the structure's elongation. By examining this variation, it became evident that the conductive FilaFlex structures exhibited two distinct slopes-one positive and one negative. In contrast, the structures made with ionically conductive cellulose displayed only a single slope.

The variation of resistance was evaluated with the use of the following formula:

$$\frac{\Delta R}{Ro}\,(\%) = \frac{R - Ro}{Ro} * 100$$

R is the instantaneous value of the resistance at a specific time

Ro is the initial value of the resistance

The presence of dual slopes in the conductive FilaFlex graphs necessitated an additional examination. At that juncture, it seemed prudent to scrutinize the distinctions between lateral and conventional conduction, particularly in their variability of resistance. The findings revealed intriguing insights (Fig 4.12-4.18).

Specifically, three observations could be drawn from these graphs:

- There appeared to be no significant difference between lateral and conventional conduction.
- Models crafted with conductive FilaFlex exhibited behavior akin to ionically conductive cellulose models upon subsequent testing; notably, repeated testing correlated with a reduction in the positive slope.
- Furthermore, when structures were tested after a prolonged period of rest, a slight reappearance of the slope was observed.

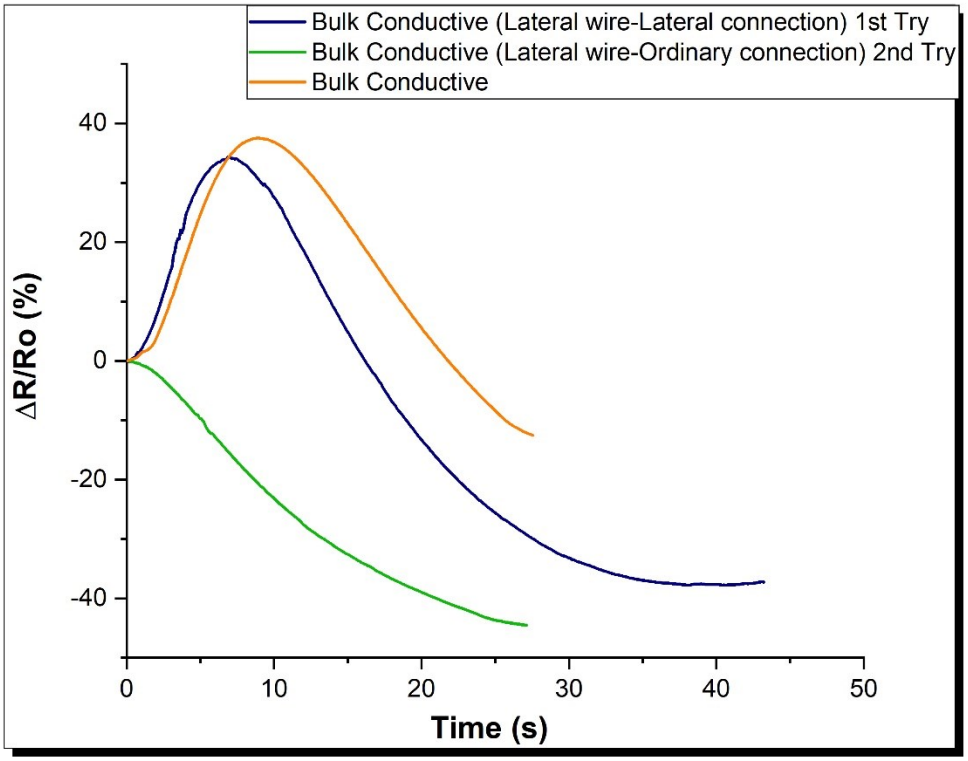

Figure 4.12 Variation of resistance in time for Bulk structures printed with Conductive FilaFlex

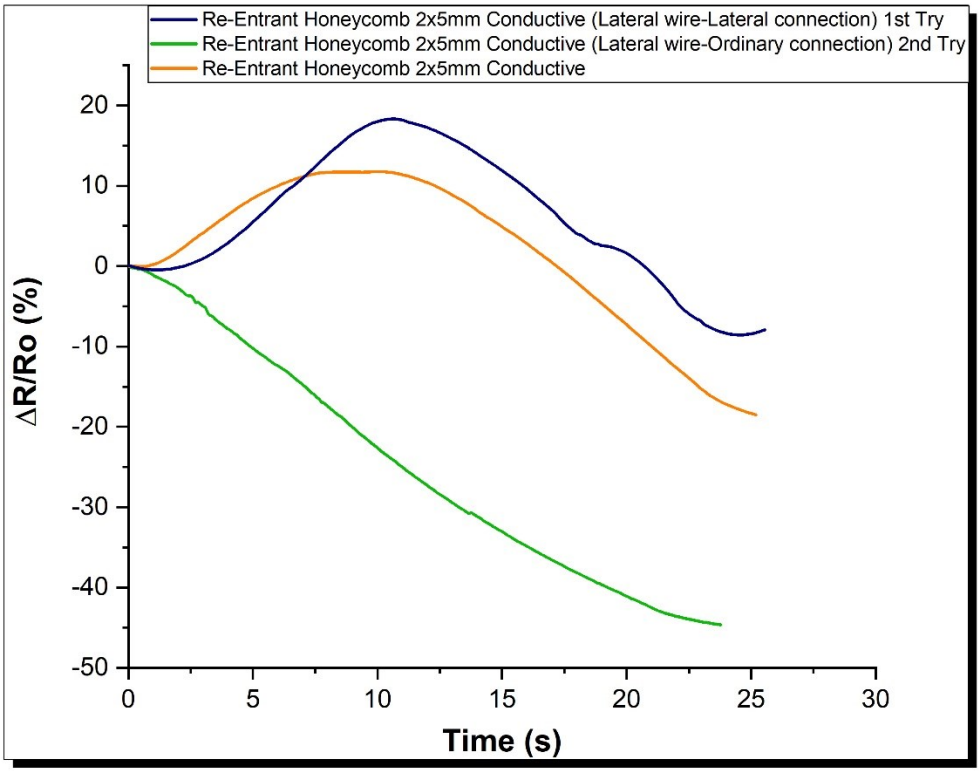

Figure 4.13 Variation of resistance in time for Re-Entrant Honeycomb 2x5mm structures printed with Conductive FilaFlex

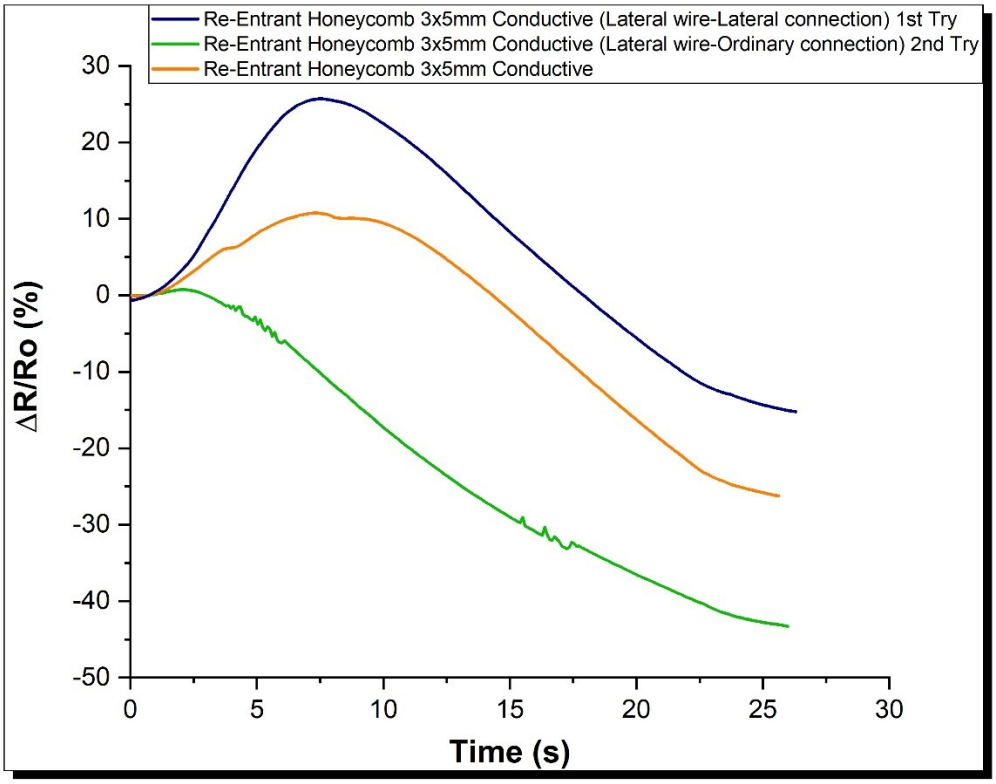

Figure 4.14 Variation of resistance in time for Re-Entrant Honeycomb 3x5mm structures printed with Conductive FilaFlex

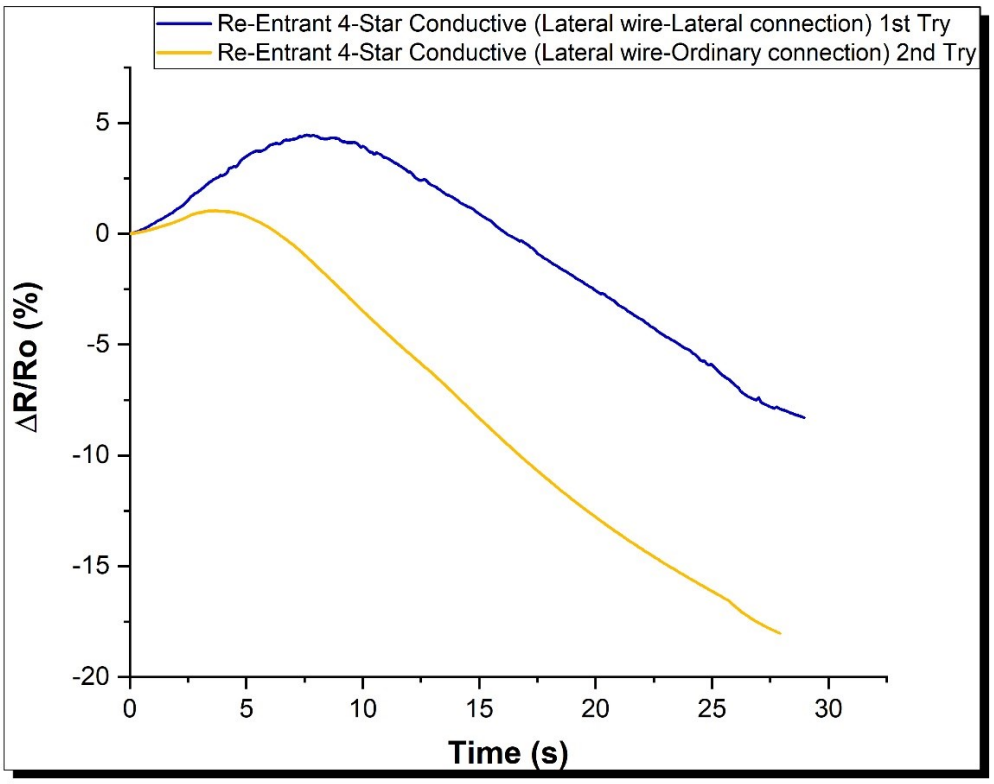

Figure 4.15 Variation of resistance in time for Re-Entrant 4-Star structures printed with Conductive FilaFlex

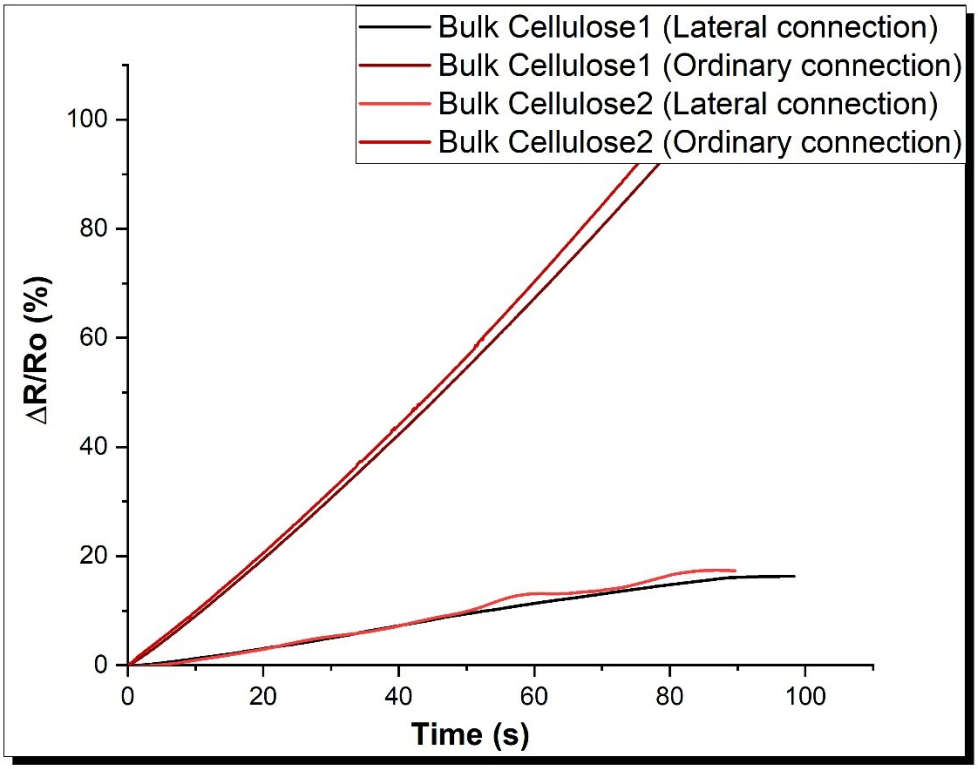

Figure 4.16 Variation of resistance in time for structures printed with ionically conductive cellulose: Bulk

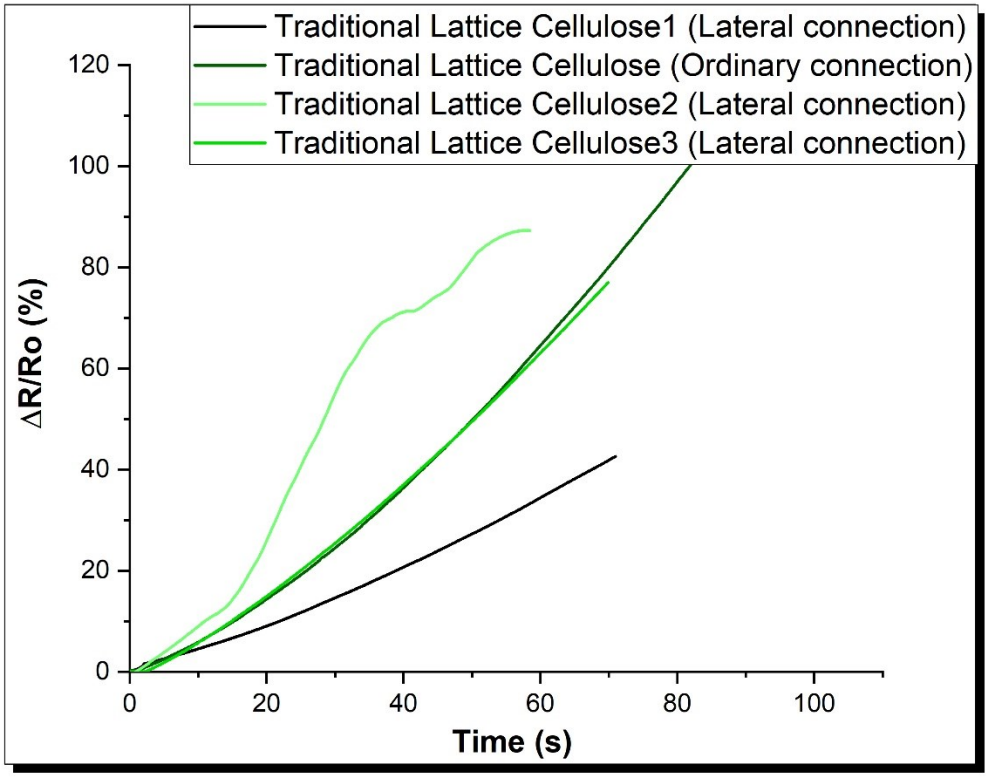

Figure 4.17 Variation of resistance in time for structures printed with ionically conductive cellulose: Traditional Lattice

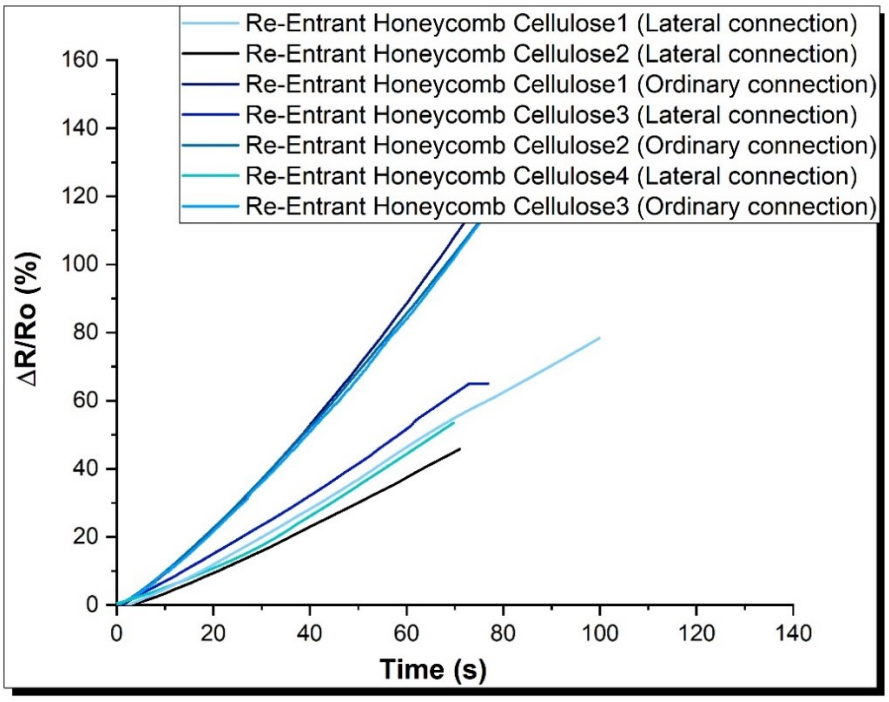

Figure 4.18 Variation of resistance in time for structures printed with ionically conductive cellulose: Re-Entrant Honeycomb

To substantiate the second hypothesis, the models underwent a secondary testing phase two weeks later, subjected to a 10% elongation. This aimed to observe whether the positive slope would diminish, vanish or remain unchanged (Fig 4.19-4.22).

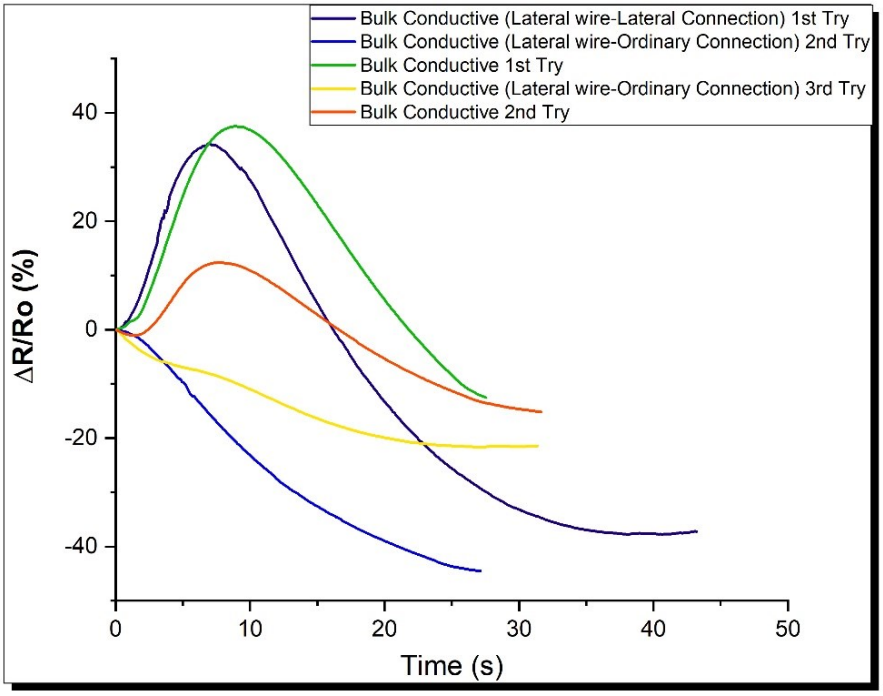

Figure 4.19 Comparison between 1st and 2nd try: Variation of resistance in time for Bulk models made with Conductive FilaFlex

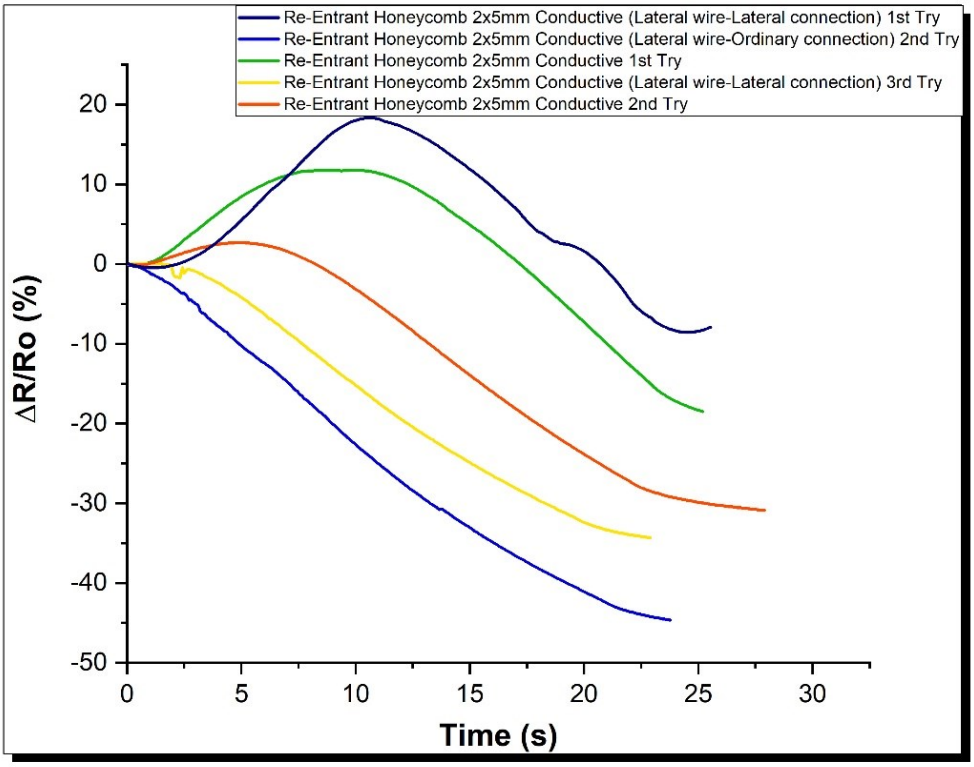

Figure 4.20 Comparison between 1st and 2nd try: Variation of resistance in time for Re-Entrant Honeycomb 2x5mm models made with Conductive FilaFlex

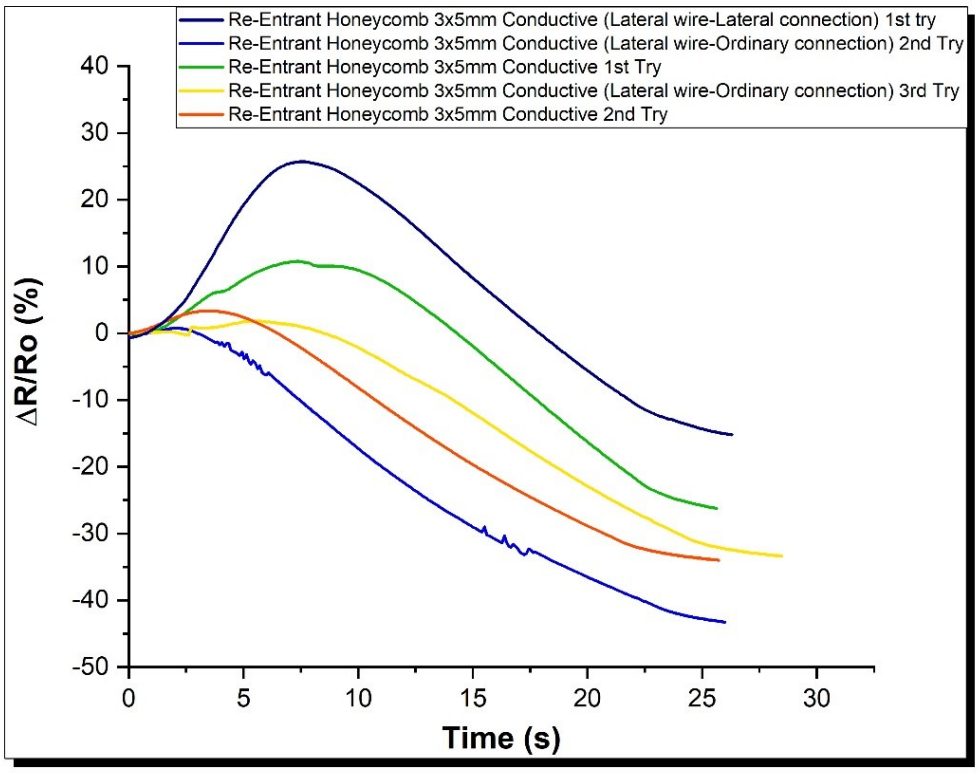

Figure 4.21 Comparison between 1st and 2nd try: Variation of resistance in time for Re-Entrant Honeycomb 3x5mm models made with Conductive FilaFlex

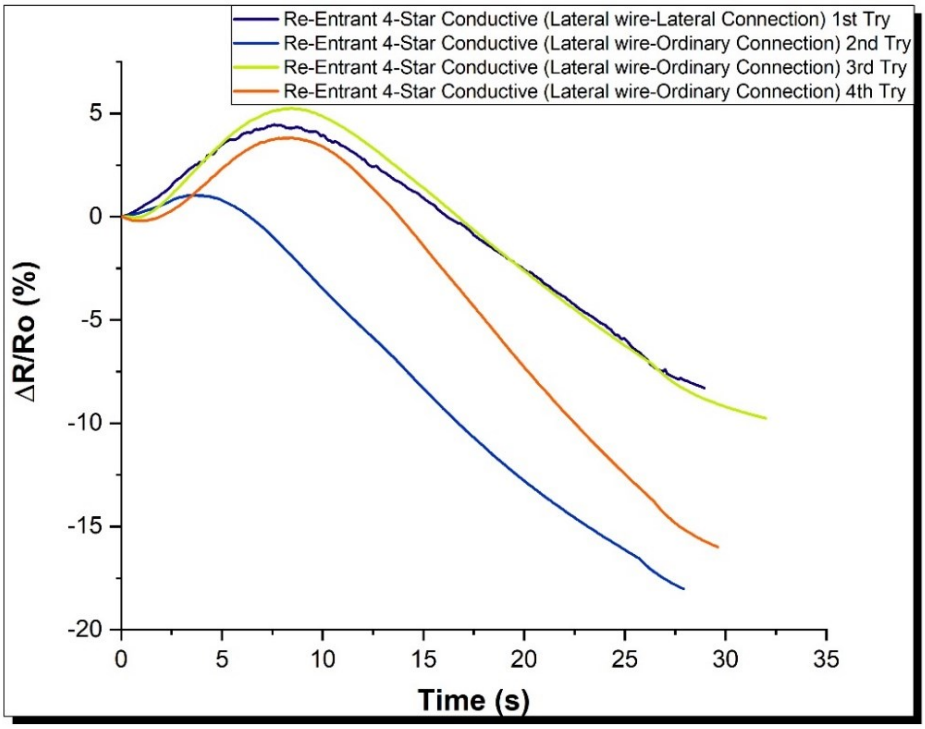

Figure 4.22 Comparison between 1st and 2nd try: Variation of resistance in time for Re-Entrant 4-Star models made with Conductive FilaFlex

The graphs depicted above suggest the possibility of a residual effect from the initial deformation, enabling the structure to mimic the behavior of the ionically conductive cellulose. Indeed, after allowing the models to rest for two weeks, a subsequent test revealed that all models exhibited both slopes once again, albeit with a reduced magnitude compared to the original measurements.

To gain a comprehensive understanding of these phenomena, conducting hysteresis tests on both lateral and conventional conduction for all printed models made with conductive FilaFlex seemed indispensable.

The parameters used were the following:

- Elongation: 10%
- Cycles: 10
- Speed: 10mm/min

Upon observing the new graphs, it became apparent that auxetic structures exhibited a significantly more uniform mechanical response in comparison to the bulk models. Furthermore, these structures demonstrated a reduced hysteresis response (Fig. 4.23-4.26).

On the other hand, interpreting the electrical response posed a more nuanced challenge (Fig. 4.27-4.30).

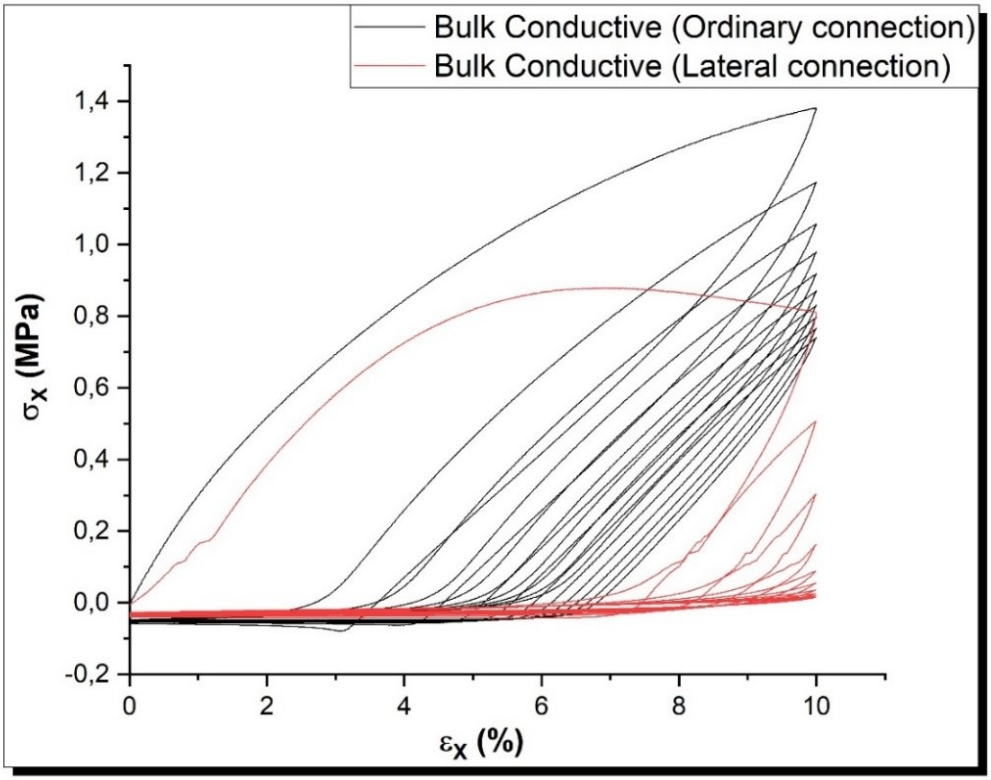

Figure 4.23 Ordinary connection Vs Lateral connection: Bulk, conductive FilaFlex

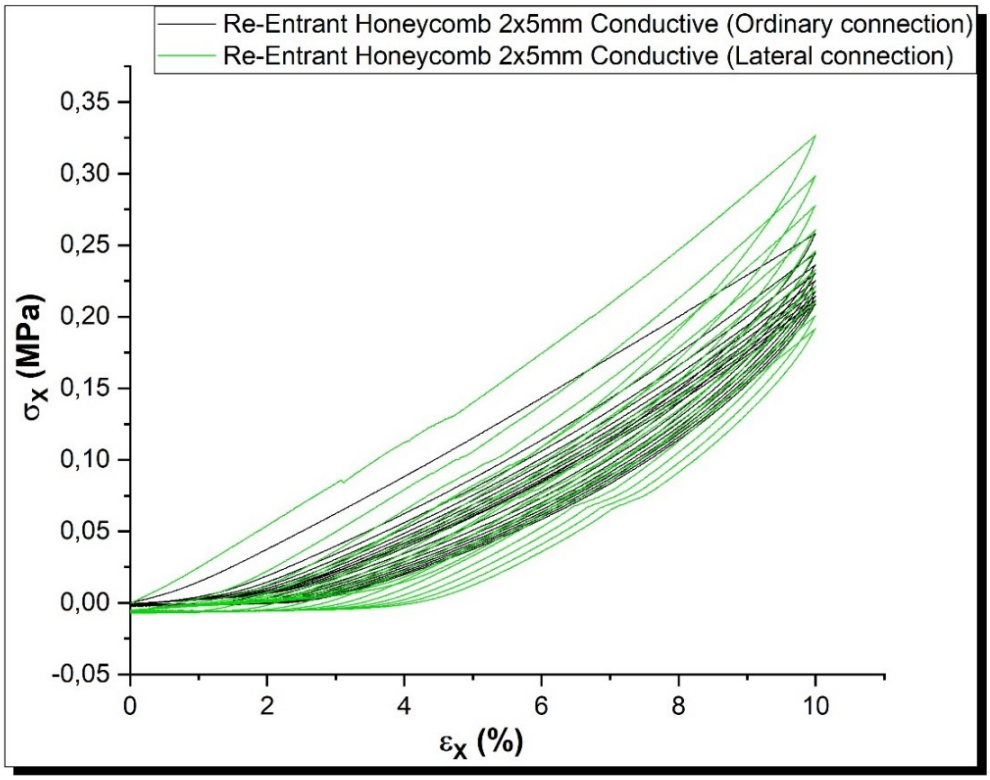

Figure 4.24 Ordinary connection Vs Lateral connection: Re-Entrant Honeycomb 2x5mm, conductive FilaFlex

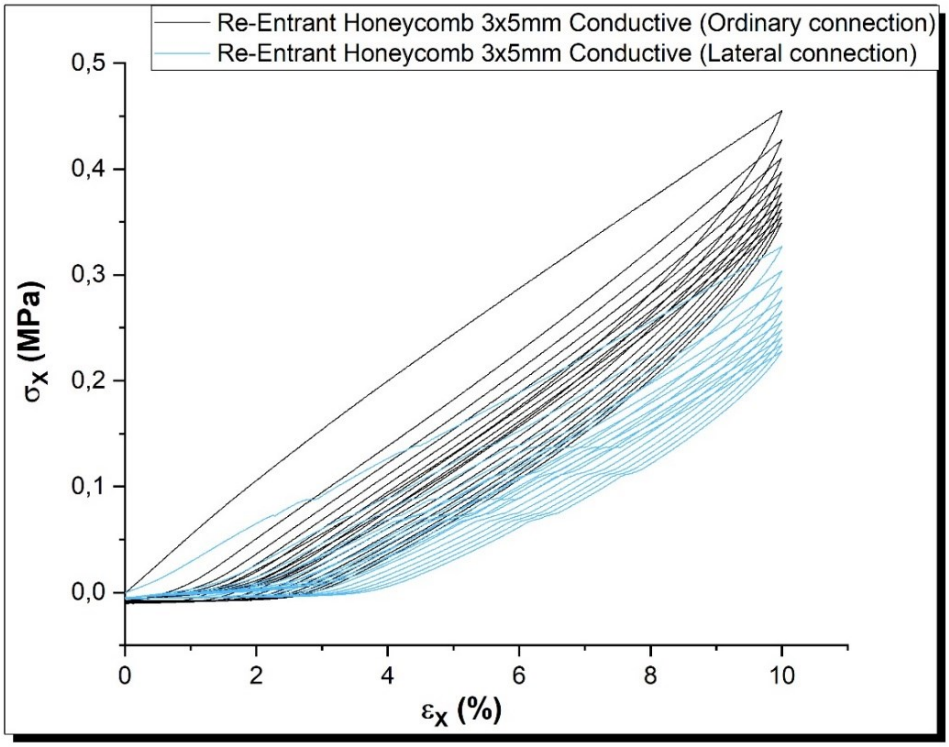

Figure 4.25 Ordinary connection Vs Lateral connection: Re-Entrant Honeycomb 3x5mm, conductive FilaFlex

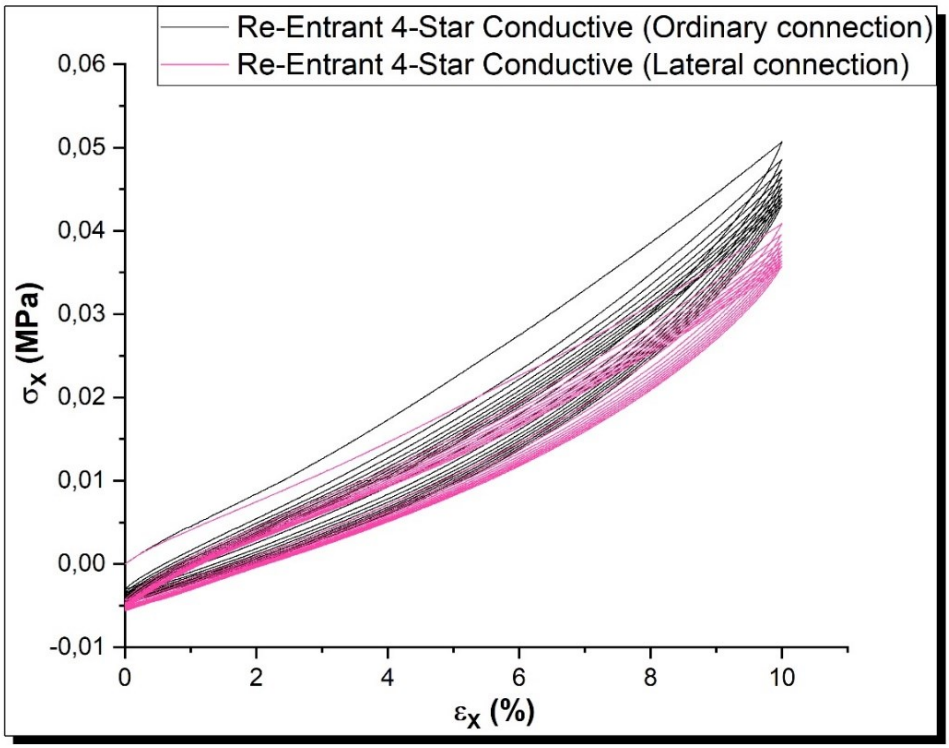

Figure 4.26 Ordinary connection Vs Lateral connection: Re-Entrant 4-Star, conductive FilaFlex

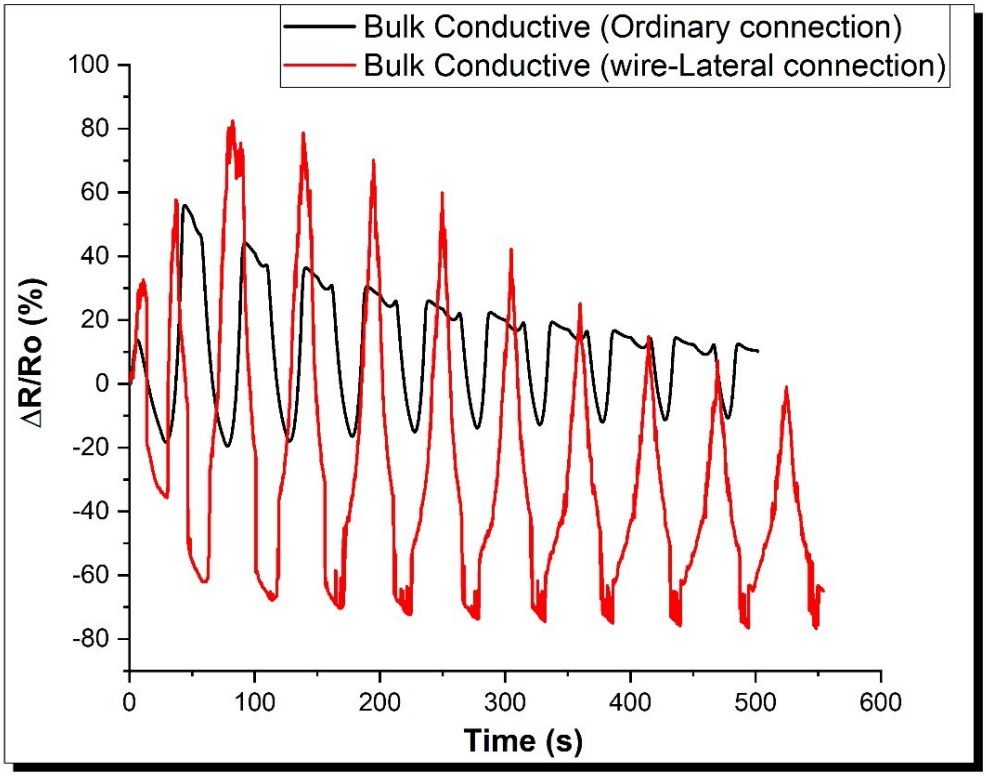

Figure 4.27 Graph ΔR/Ro-t Ordinary connection Vs Lateral connection: Bulk, conductive FilaFlex

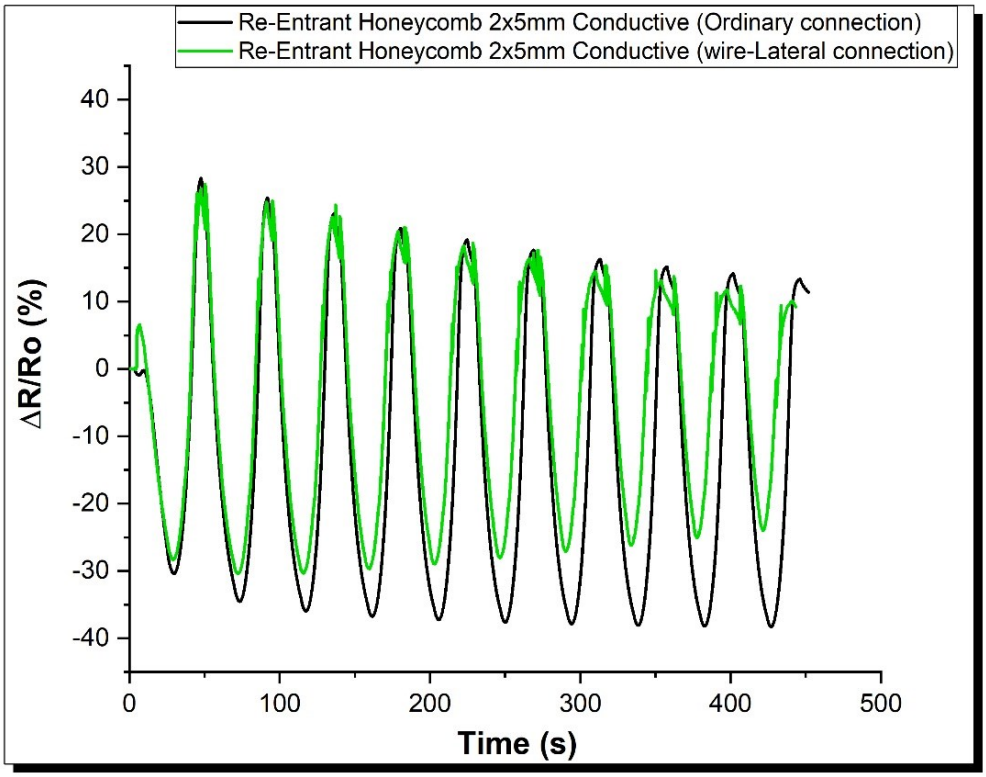

Figure 4.28 Graph ΔR/Ro-t Ordinary connection Vs Lateral connection: Re-Entrant Honeycomb 2x5mm, conductive FilaFlex

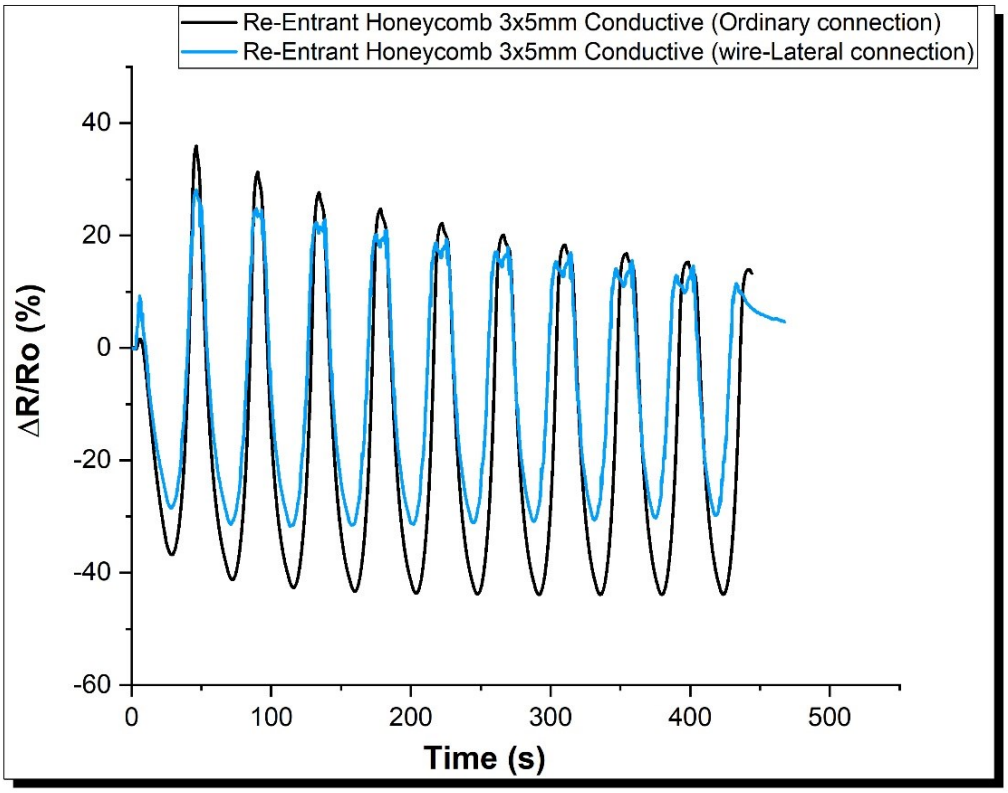

Figure 4.29 Graph ΔR/Ro-t Ordinary connection Vs Lateral connection: Re-Entrant Honeycomb 3x5mm, conductive FilaFlex

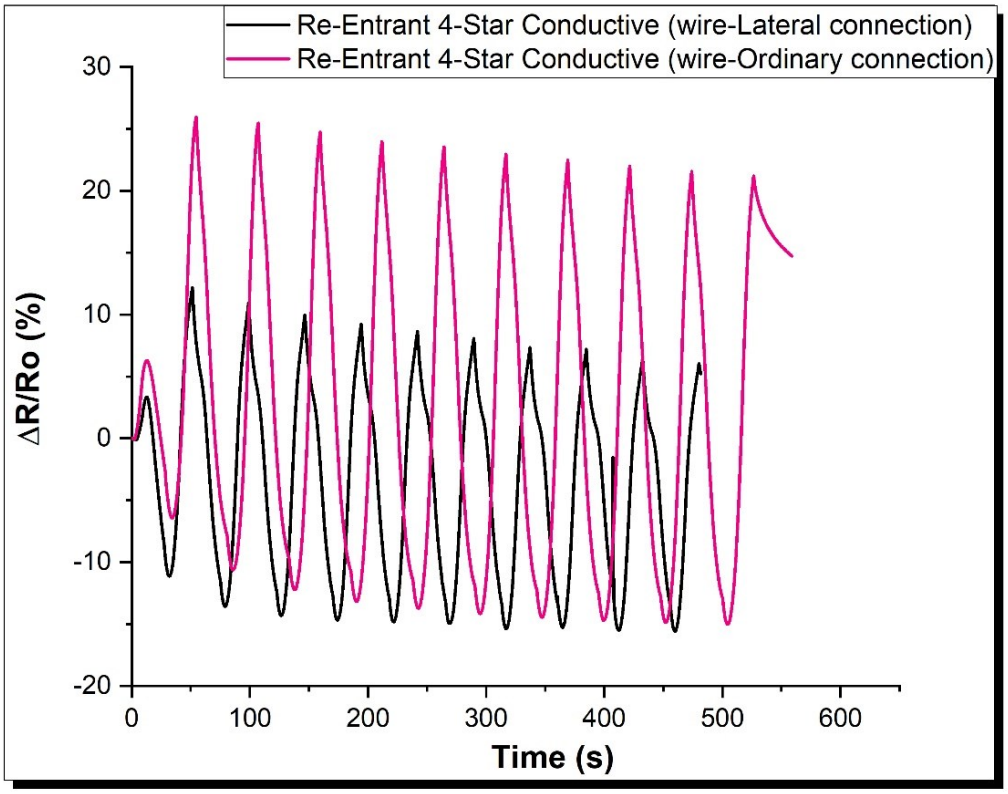

Figure 4.30 Graph ΔR/Ro-t Ordinary connection Vs Lateral connection: Re-Entrant 4-Star, conductive FilaFlex

Upon analyzing the resistance variation over time, it was evident that all auxetic structures exhibited a greater fluctuation in resistance during ordinary conduction that during lateral conduction. In contrast, the response of the bulk models was observed to be complex to interpret.

Overall, these curious phenomena involving both the dual slopes and the lateral conduction of the structures require a further investigation for a thorough interpretation in future studies.

- ***Gauge Factor (Graph $\Delta R/Ro$-εx)***

The last factor to be evaluated was the Gauge Factor.

The Gauge Factor is defined in literature as the ratio per unit change in resistance to per unit change in length. It is an important parameter that allows to evaluate the performance of a sensor.

$$G = \frac{\Delta R/Ro}{\varepsilon_x}$$

ΔR/Ro is the absolute variation of resistance (%)

εx is the axial deformation along the X axis (%)

Typically, metallic strain gauges have a gauge factor around 2. This means that for a 1% change in strain, the relative resistance change is about 2%. On the other hand, semiconductor strain gauges present much higher values that range from 50 to 200. This is due to the higher sensitivity of semiconductor materials to strain.

In contrast to structures fabricated with conductive FilaFlex, cellulose models exhibited significantly more consistent behavior. (Fig 4.31). It was readily apparent that lateral conduction was notably lower than conventional conduction (Fig 4.32). This phenomenon can be attributed to the fact that the lateral expansion of the structure is typically less than the axial expansion, resulting in a smaller cross section, and as a consequence in a much more difficult passage of the ions.

Conversely, the situation with the conductive FilaFlex, as mentioned earlier, appeared somewhat different. In fact, these structures displayed two distinct slopes rather than a single one, paralleling the patterns observed in the ΔR/Ro-t graphs (Fig. 4.33-4.36).

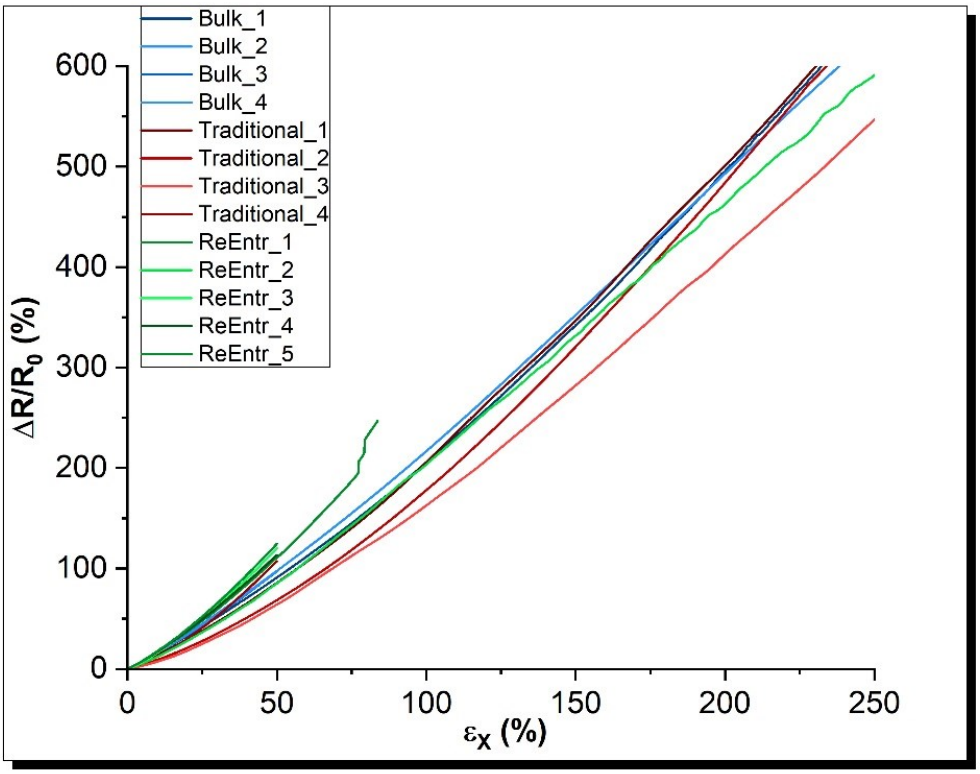

Figure 4.31 Graph ΔR/Ro-εx for models printed with ionically conductive cellulose: Evaluation of Gauge Factor

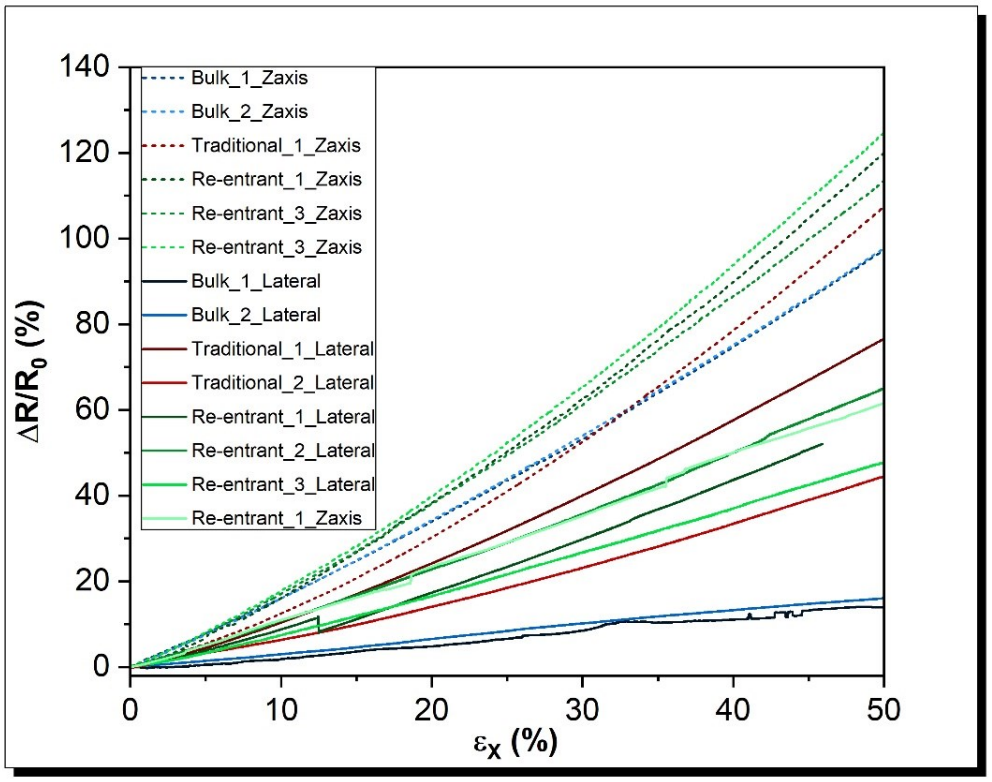

Figure 4.32 Graph ΔR/Ro-εx for bulk models printed with ionically conductive cellulose: comparison between lateral and ordinary conduction

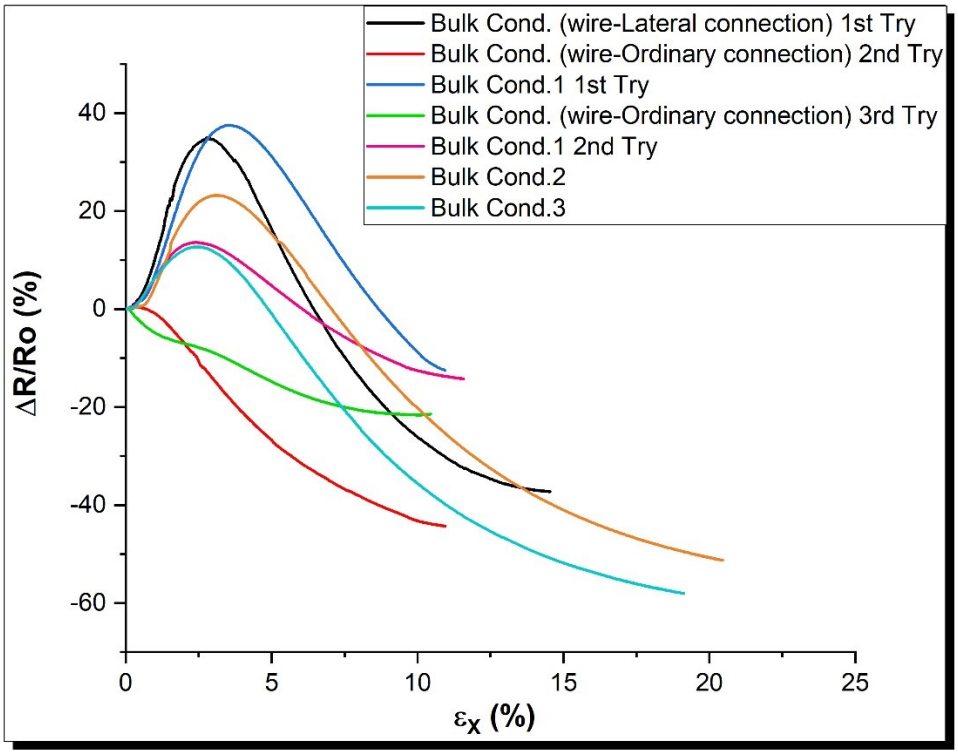

Figure 4.33 Graph ΔR/Ro-εx for bulk models printed with Conductive FilaFlex: comparison between lateral and ordinary conduction & Evaluation of Gauge factor

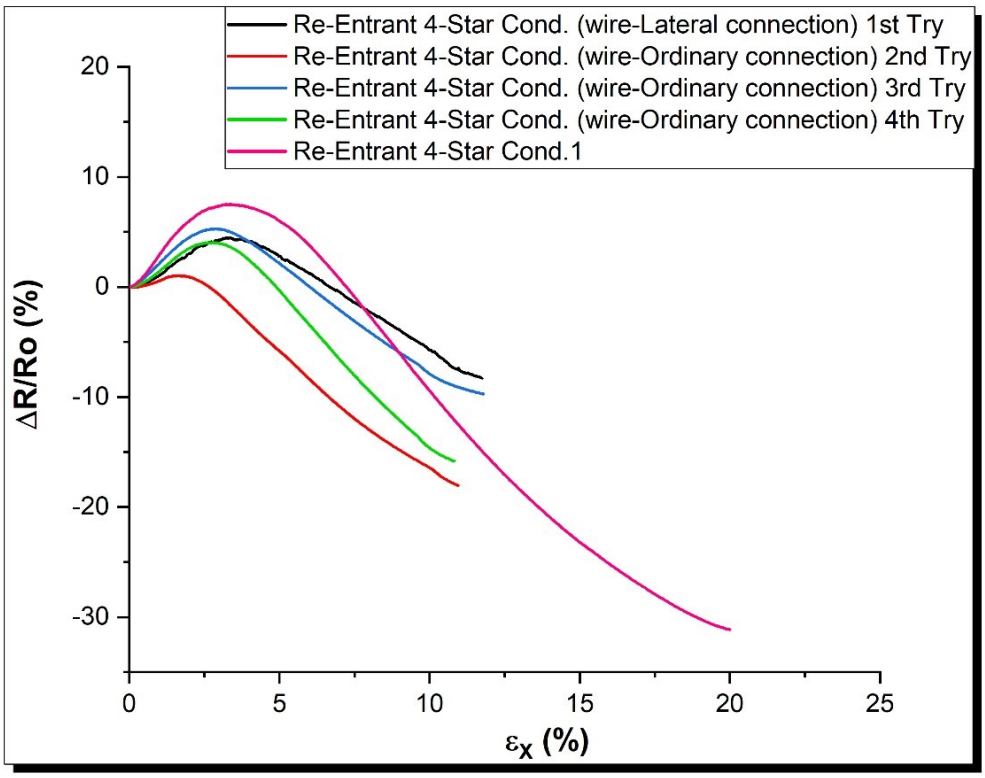

Figure 4.34 Graph ΔR/Ro-εx for Re-Entrant 4-Star models printed with Conductive FilaFlex: comparison between lateral and ordinary conduction & Evaluation of Gauge factor

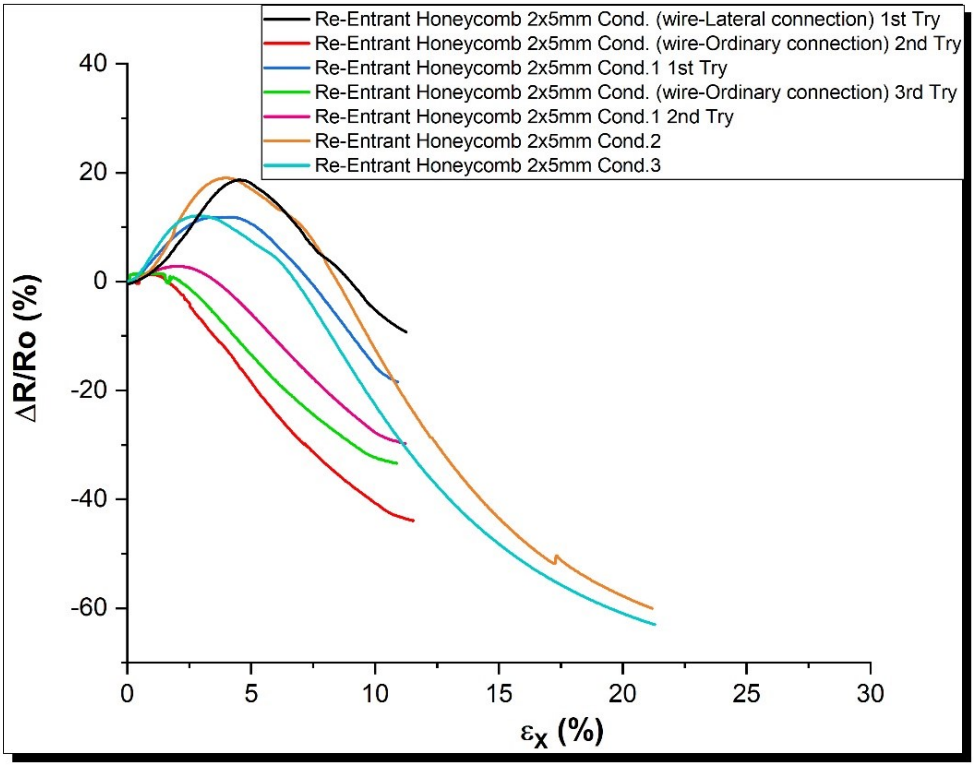

Figure 4.35 Graph ΔR/Ro-εx for Re-Entrant Honeycomb 2x5mm models printed with Conductive FilaFlex: comparison between lateral and ordinary conduction & Evaluation of Gauge factor

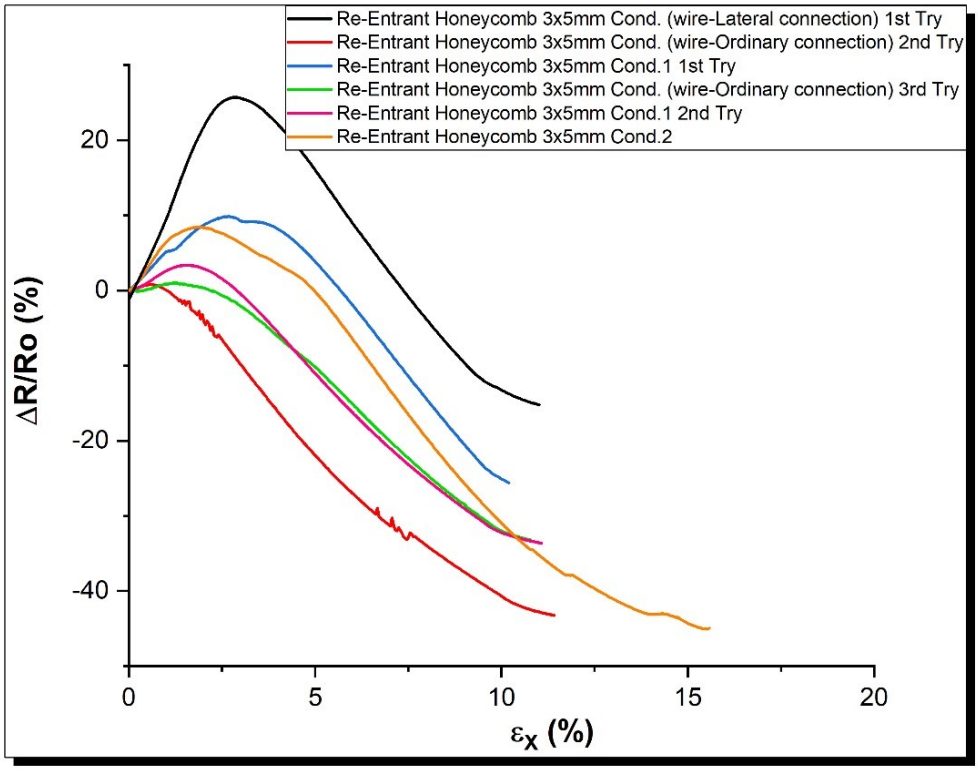

Figure 4.36 Graph ΔR/Ro-εx for Re-Entrant Honeycomb 3x5mm models printed with Conductive FilaFlex: comparison between lateral and ordinary conduction & Evaluation of Gauge factor

With the aim of evaluating the approximate value of the Gauge factor for each structure, measurements for the conductive FilaFlex structures were focused solely on the values associated with the negative slopes.

When a strain gauge exhibits a negative slope, it means that the resistance decreases as the strain increases. The gauge factor in this context is still evaluated using the same principles, but care must be taken to properly account for the sign and slope in the calculations. Since the gauge factor is negative, the gauge factor will also be negative.

Subsequently, the Gauge factors obtained for both conductive FilaFlex models and ionically conductive cellulose ones were compiled into two separate tables:

Table 6 Experimental values of Gauge factor for Conductive FilaFlex models: negative slope

Conductive FilaFlex (Negative Slope)	
Bulk	-6,025
Re-Entrant 4-Star	-2,543
Re-Entrant Honeycomb 2x5mm	-4,710
Re-Entrant Honeycomb 3x5mm	-5,360

Table 7 Experimental values of Gauge factor for cellulose models

Cellulose (Single-Positive Slope)	
Bulk	1,425
Traditional Lattice	0,965
Re-Entrant Honeycomb 3x5mm	1,408

5. Conclusions & Future Applications

This research has demonstrated the unique properties of mechanical metamaterials, including their ability to exhibit negative Poisson's ratio, tunable stiffness, and adaptive deformation. These properties have been rigorously tested and validated through experimental and computational methods. During this process innovative design and building methodologies for mechanical metamaterials have been introduced, leveraging both theoretical (COMSOL Multiphysics) and practical fabrication techniques (Additive Manufacturing). These methodologies contribute significantly to the field, providing new avenues for customizing material properties.

Specific applications, such as flexible electronics and piezoresistive response, have been explored, showcasing some interesting features based on the additive manufacturing technique used: 3D FDM (Fused Deposition Modeling) & UV DPL (Digital Light Printing).

This field is still very new, and the discoveries made during the course of this study have pushed the boundaries of conventional material science. This work not only expands the fundamental understanding of mechanical metamaterials but also paves the way for future research. This research has also highlighted the importance of interdisciplinary approaches, combining principles from physics, engineering, material science and chemistry.

The study of mechanical metamaterials is very vast, especially since the field is still in its infancy, with vast potential yet to be explored. The insights and methodologies developed in this thesis lay a strong foundation for future applications contributing to technological progress and societal well-being. Mechanical metamaterials can be applied to biomedical devices by designing implants and prosthetics that closely mimic the flexibility and resilience of natural tissues, enhancing patient comfort and recovery. It can be also applied to Wearable technologies, in fact, their flexibility, lightweight, and durability can be used in wearable devices, improving their performance and user experience. Such applications may include health monitoring, soft robotics and smart textiles.

The directions that can be taken from here are also very vast. Future research can focus on scaling the production or dimension of mechanical metamaterials and developing cost-effective manufacturing processes. Techniques such as advanced 3D printing have shown how promising they can be as areas to explore. Developing metamaterials that can dynamically change their properties in response of external stimuli could also open up new functionalities and applications. Integrating mechanical metamaterials with smart systems and IoT can create advanced materials that not only adapt to their environment but also provide real-time data for predictive maintenance and other uses. Last but not least, research into eco-friendly materials and sustainable production methods is essential. Exploring bio-inspired designs and recyclable materials will contribute to the environmental sustainability of mechanical metamaterials.

6. References

6.1. Bibliography

[1] Mauko, Anja, et al. Dynamic deformation behaviour of chiral auxetic lattices at low and high strain-rates. Metals, 2020, 11.1: 52
[2] Duncan, Olly, et al. Review of auxetic materials for sports applications: Expanding options in comfort and protection. Applied Sciences, 2018, 8.6: 941.
[3] Chen, Meng, et al. Design of an acoustic superlens using single-phase metamaterials with a star-shaped lattice structure. Scientific reports, 2018, 8.1: 1861.
[4] Bhat, Chinmai, et al. Design of tessellation based load transfer mechanisms in additively manufactured lattice structures to obtain hybrid responses. Additive Manufacturing, 2023, 76: 103774.
[5] Buchner, Thomas JK, et al. Vision-controlled jetting for composite systems and robots. Nature, 2023, 623.7987: 522-530.
[6] Lecina-Tejero, Óscar, et al. The rise of mechanical metamaterials: Auxetic constructs for skin wound healing. Journal of Tissue Engineering, 2023, 14: 20417314231177838.
[7] Dell'isola, Francesco; Steigmann, David; Della Corte, Alessandro. Synthesis of complex structures. Designing micro-structure to deliver targeted macro-scale.
[8] Shintake, Jun; Nagai, Toshiaki; Ogishima, Keita. Sensitivity improvement of highly stretchable capacitive strain sensors by hierarchical auxetic structures. Frontiers in Robotics and AI, 2019, 6: 127.
[9] Gu, Jimin, et al. Self-powered strain sensor based on the piezo-transmittance of a mechanical metamaterial. Nano Energy, 2021, 89: 106447.
[10] Lu, Haotian, et al. 3D Printing and processing of miniaturized transducers with near-pristine piezoelectric ceramics for localized cavitation. Nature communications, 2023, 14.1: 2418.
[11] Cholleti, Eshwar Reddy. A Review on 3D printing of piezoelectric materials. In: IOP conference series: materials science and engineering. IOP Publishing, 2018. p. 012046.
[12] Jiao, Pengcheng, et al. Mechanical metamaterials and beyond. Nature communications, 2023, 14.1: 6004.
[13] Mohammadi, Alireza, et al. Flexible mechanical metamaterials enabling soft tactile sensors with multiple sensitivities at multiple force sensing ranges. Scientific reports, 2021, 11.1: 24125.
[14] Huang, Xin, et al. Flexible mechanical metamaterials enabled electronic skin for real-time detection of unstable grasping in robotic manipulation. Advanced Functional Materials, 2022, 32.23: 2109109.
[15] Wang, Dong; DONG, Le; GU, Guoying. 3D printed fractal metamaterials with tunable mechanical properties and shape reconfiguration. Advanced Functional Materials, 2023, 33.1: 2208849.
[16] Barchiesi, Emilio; Spagnuolo, Mario; Placidi, Luca. Mechanical metamaterials: a state of the art. Mathematics and Mechanics of Solids, 2019, 24.1: 212-234.
[17] Owusu, Francis, et al. How to Make Elastomers Piezoelectric?. Advanced Materials Technologies, 2023, 8.15: 2300099.
[18] Jiang, Ying, et al. Auxetic mechanical metamaterials to enhance sensitivity of stretchable strain sensors. Advanced Materials, 2018, 30.12: 1706589.
[19] Loh, Leon Yeong Wei, et al. 3D printed metamaterial capacitive sensing array for universal jamming gripper and human joint wearables. Advanced Engineering Materials, 2021, 23.5: 2001082.
[20] Kolken, H. Ma; Zadpoor, A. A. Auxetic mechanical metamaterials. RSC advances, 2017, 7.9: 5111-5129.
[21] Khan, Sohaib Z.; MASOOD, S. H.; COTTAM, Ryan. Mechanical properties in tensile loading of H13 re-entrant honeycomb auxetic structure manufactured by direct metal deposition. In: *MATEC Web of*

Conferences. EDP Sciences, 2015. p. 01004.
[22] Mizzi, Luke, et al. Mechanical metamaterials with star-shaped pores exhibiting negative and zero Poisson's ratio. *Materials & Design*, 2018, 146: 28-37.
[23] Lvov, V. A., et al. Design and mechanical properties of 3D-printed auxetic honeycomb structure. Materials Today Communications, 2020, 24: 101173.
[24] Geng, Luchao, et al. Damage characterizations and simulation of selective laser melting fabricated 3D re-entrant lattices based on in-situ CT testing and geometric reconstruction. *International Journal of Mechanical Sciences*, 2019, 157: 231-242.
[25] Johnston, Ross; KAZANCI, Zafer. Analysis of additively manufactured (3D printed) dual-material auxetic structures under compression. *Additive Manufacturing*, 2021, 38: 101783.
[26] Ma, Pibo, et al. Review on the knitted structures with auxetic effect. *The Journal of The Textile Institute*, 2017, 108.6: 947-961.

6.2. List of Figures

6.3. List of Tables

Acknowledgements

This thesis has been one of the most enriching experiences of my academic journey. Beginning as a purely theoretical one, it evolved into something entirely new along the way.

Through this process, I had the opportunity to explore familiar hobbies and delve into entirely new areas of study. This experience has significantly contributed to my personal growth and has reinforced my passion for research and innovation.

First and foremost, I would like to thank for this experience Professor Stefano Stassi, for believing in me and for assigning me this task, and his graduate assistant Giorgio Mogli, for both supervising me through the whole experience but also giving me the freedom to take autonomous decisions and dare to try out things.

It is important to thank at this point all the other people who dove into this new experience along with me, all the PoliTo undergraduates in the interdip lab. Without them, the long lab hours and meetings wouldn't have been the same. We shared laughs and problems together, and I will cherish those moments even if our paths may never cross again. And, of course, I wish them all the best of luck and I'm sure they'll do great things in the future.

The next person I need to thank is my mom, the first person to always believe in me no matter what. It's no easy job to provide for two kids on your own and she needs a reward just for that. She is the one who encouraged me to study far away from home and she would do anything if it meant investing in my future. And, for that I'm truly grateful.

A special thanks goes also to some people in my life that have always been there, even in the toughest of moments. Those are the ones that, even from kilometers away, were able to encourage me, help me or even support my rants whenever I needed them the most. Giovanni, Carmine, Laura, Renato, Bea, Adolfo, Salvo, Malak, Lili, Atlas, Allan, Ben, Francesco thank you all for just being your awesome selves, I can't thank you enough. I could write whole chapters about every single one of you, but I choose to be brief for both your sakes and for the sake of the poor readers that may need to get through them.

I did thank all the people in my life that supported me from distance, but recently I felt the need to also thank a person that helped me in presence instead. This is a late submission, but a necessary one. Without a further ado, a special thanks goes also to Giuseppe for selflessly reading this whole document and taking professional notes for the sole purpose of helping me out even if he was busy with his own exams in the meantime. I'm honored to call him my friend.

Last but not least, I want to thank every single person that I have met throughout those years. Even if our interaction may have been brief the wisdom or kindness showed in those interactions has shaped me. If I am the person I am today is also thanks to those people. Either they were colleagues, or friends that we grew apart with or just simple acquaintances, their contribution has been equally important for me.